UNIVERSIDADE D
COIMBRA

Marcos João do Carmo Gouveia

Modelling Endothelial Cells' Collective Movement and Keratin Cytoskeleton Dynamics using the Phase Field Method

Tese no âmbito do Doutoramento em Física, ramo de Física Computacional, orientada pelo Professor Doutor Rui Davide Martins Travasso e pela Professora Doutora Maria José Cardoso Oliveira e apresentada ao Departamento de Física da Faculdade de Ciências e Tecnologia da Universidade de Coimbra.

Fevereiro de 2023

Funding

The author thanks the support of national funds from FCT – Fundação para a Ciência e a Tecnologia, I.P. through grant SFRH/BD/136046/2018 and through projects UIDB/04564/2020 and UIDP/04564/2020. This work was also funded by FEDER funds through the Operational Programme Competitiveness Factors–COMPETE and by Fundação para a Ciência e a Tecnologia–Ministério da Ciência, Tecnologia e Ensino Superior (FCT-MCTES, Portugal) under the project POCI-01-0145-FEDER-031743–PTDC/BIA-CEL/31743/2017 and by UE/FEDER funds through the program COMPETE 2020, under the project CENTRO-01-0145-FEDER-000014 (MATIS).

Abstract

Over the last two decades, the development of mathematical models to describe both the individual and collective behavior of cells in different biological processes has been an active area of study, as well as the focus of multidisciplinary research teams, often composed of experimental and theoretical biologists, mathematicians, computer scientists and physicists. In this work, we employ the phase field method to describe the dynamics of cellular systems at different scales.

We start by modeling a single cell has we investigate how the dynamics of the keratin intermediate filament network is affected by the K14R125P mutation, which can be found in keratinocytes of patients suffering from Epidermolysis Bullosa Simplex (EBS). Based on experimental results obtained for the distribution of keratin in the cytoskeleton, we are able to create a mathematical model that reproduces those results. We show that, by assuming that the K14R125P affects the assembly process of keratin filaments, we can predict the spatial distribution of keratin filaments in wild-type cells, as well as the accumulation of keratin particles in the cortex of the keratinocyte, in the case where there is mutant keratin in the cell.

To further understand how the formation of keratin aggregates depends on the amount of mutant keratin present in a cell's cytoskeleton, we test different reaction networks that take into account the coexistence of wild-type and mutant keratins. From experiments we know that the maximum amount of keratin aggregates is obtained when around 25% of a cell's keratin content is mutant. By assuming that keratin aggregate formation occurs as a result of the asymmetric binding of WT and mutant keratin, we are able to find a region of parameter space where the model is able to correctly predict what is observed experimentally.

Next, we go from models that describe a single cell, to a model that uses a multi-phase field approach to simulate a multi cellular system. By simulating a vessel constituted by endothelial cells organized in a tubular structure, we are able to study how cell-cell and cell-matrix adhesion, coupled to blood flow induced endothelial cell polarization, leads to cell rearrangement and cell shape heterogeneity. By simulating a tip cell sprouting from the vessel, we are able to show that the velocity of the tip cell influences the formation of the new sprout. We also explore the importance of stalk-cell proliferation in providing structural integrity to the sprout.

Finally, we present a phase field model capable of describing a two-phase system and its elastic behavior. Using this model we study how the rigidity of the extracellular matrix affect the morphology of growing vessel networks. We show that for soft matrices, there is little to no vessel formation and instead we see that tip cells detach from the main vessel, migrating alone. As we increase the rigidity, we start observing the formation of elongated sprouts. In accordance with experiments, we show that vessel length does not have a linear

dependence with ECM rigidity, since there is a value of rigidity at which sprout length is maximum, decreasing as the ECM becomes stiffer.

Resumo

No decorrer das últimas duas décadas, o desenvolvimento de modelos matemáticos para descrever o comportamento, individual e coletivo, de células em diferentes processos biológicos, tem sido uma área de estudo ativa, assim como o foco de equipas de investigação multidisciplinares, compostas por biólogos teóricos e experimentais, matemáticos, cientistas de computação e físicos. Neste trabalho, utilizamos o método de interface difusa para descrever a dinâmica de sistemas celulares, a diferentes escalas.

Começamos por modelar uma célula individual, de maneira a investigar de que maneira a dinâmica da rede de filamentos intermédios de queratina é afetada pela mutação K14R125P, que pode ser encontrada em queratinócitos de pacientes que sofrem de Epidermolysis Bullosa Simplex (EBS). Tendo por base os resultados experimentais obtidos para a distribuição de queratina no citoesqueleto, podemos criar um modelo matemático que reproduz esses resultados. Mostramos também que, assumindo que a mutação R125P afeta o processo de montagem de filamentos de queratina, podemos prever a distribuição espacial de filamentos de queratina em células normais, assim como a acumulação de partículas de queratina junto à membrana celular do queratinócito, no caso em que a célula possui queratina mutante.

De maneira a perceber como é que a formação de agregados de queratina depende da quantidade de queratina mutante presente no citoesqueleto, testamos diferentes redes de reações, tendo em conta a coexistência de queratina mutante e não-mutante. Dos resultados experimentais, sabemos que a quantidade máxima de agregados de queratina é obtida quando aproximadamente 25% do conteúdo de queratina da célula é mutante. Assumindo que a formação de agregados ocorre devido à ligação entre queratina mutante e não-mutante em proporções distintas, somos capazes de encontrar uma zona do espaço dos parâmetros, onde o modelo é capaz de prever corretamente o que é observado nas experiências.

De seguida, passamos de modelos que descrevem sistemas apenas com uma célula, para um modelo que usa um modelo de múltiplas interfaces difusas para simular um sistema multicelular. Ao simular um vaso sanguíneo cilíndrico constituído por células endoteliais, podemos estudar como a adesão entre células endoteliais e entre uma célula e a matriz extracelular, acopladas à polarização induzida pela corrente sanguínea em células endoteliais, levando ao rearranjo celular e heterogeneidade de formas celulares. Ao simular uma célula da ponta migrando para fora de um vaso, podemos mostrar que a velocidade da célula da ponta influencia a formação do novo vaso, e realçando a importância da proliferação de células endoteliais em garantir a integridade estrutural do vaso.

No último capítulo, apresentados um modelo de interface difusa capaz de descrever um sistema de duas fases e o seu comportamento elástico. Usando este modelo, pretendemos estudar como é que a rigidez da matriz extracelular pode levar à formação de redes sanguíneas com morfologias diferentes. Neste trabalho mostramos que para matrizes com rigidez baixa, a formação de novos vasos é muito reduzida, e no seu lugar verificamos

que as células da ponta se separam do vaso inicial, passando a migrar individualmente. Aumentando a rigidez da matriz, começamos a ver a formação de vasos alongados. Em concordância com os resultados experimentais, mostramos que o comprimento de vasos sanguíneos não varia linearmente com a rigidez da matriz, uma vez que existe um valor ótimo de rigidez para qual o comprimento do vaso é máximo, diminuindo à medida que a matriz extracelular se torna mais rígida.

Agradecimentos

I would like to thank my supervisors Rui and Maria for their guidance during the development of the work presented in this thesis. When I started working with Rui I was a second year undergrad. From then to the present, he has taught me so much and he will always remain a mentor and a close friend. I would also like to thank João Carvalho for being an unofficial co-supervisor who is always quick to help and provide good advice.

During my years at the University of Coimbra there were a number of other people that inspired me to become a better scientist and played a vital part in my growth: Professor Constança Providência, Professor José António Paixão, Professor Fernando Nogueira and others. May they continue to serve as models for new students of the Department of Physics, as they did for me.

Part of my success is also due to the amazing group of Soft and Biological Matter and all the colleagues I have had over the years. Maurício, Marina, Tânia, Tiago and Sahar, with whom I shared experiences and who I consider good friends. During the last year I have been lucky to supervise a greatly motivated and highly skilled student, Matilde, whose work was essential for this thesis.

I would like to thank two great friends in particular, Sagar and André, who started their journey in the exact same day as I did, our first day in college. They have been loyal and supportive throughout the years and deserve a special note. There are many other friends who could be listed here so I will name a few more: Felipe, Margarida, Joana, Francisco, Sofia, Renan, Adriana, Sara, Carla, Pereira...

Of course none of this would have been possible without my family. Throughout the years they have loved me and supported me through everything: my parents, Maria João and Zé, who gave me everything and asked nothing in return. For my brother and sister, António and Rita, who are my best friends and were and will always be role models for me. To my sister from another mother, Becas, and Pedro, who besides being role models also gave me my younger "brother", Gui. To my aunts Rosa, Teresa, Nazaré and to my uncles Rui and Carlos who were all second mothers and fathers for me. Also, to Céu who took care of me since I was a little baby and treated me as her own son.

To Rita...who throughout this experience was my rock (Roque, ahaha) and is there, and will be, for the good and bad moments, and who I love dearly. Without her, this work (and I) would not be complete. To Jessie, our feline adopted daughter, who shows her affection through bite marks and scratches. Meow!

If anyone feels unjustly left out of this page, please call and I will provide an errata. Just kidding...I won't.

Contents

List of Figures

List of Tables

Chapter 1

Biological Context

1.1 Formation of Blood Vessels

1.1.1 Vasculogenesis

The existence of an efficient circulatory system is indispensable for the existence of healthy mammals. During the first weeks of embryo development, oxygen and all the necessary nutrients necessary to cells are obtained directly from the placenta by diffusion. As the embryo reaches a certain size, direct diffusion is no longer a viable process due to the very limited diffusion length of most nutrients, most importantly oxygen. As such, the circulatory system is the first functional system to be established in a developing embryo. Blood vessels that belong to this primordial circulatory system are formed by a process called vasculogenesis. Vasculogenesis is the *de novo* formation of new blood vessels from the

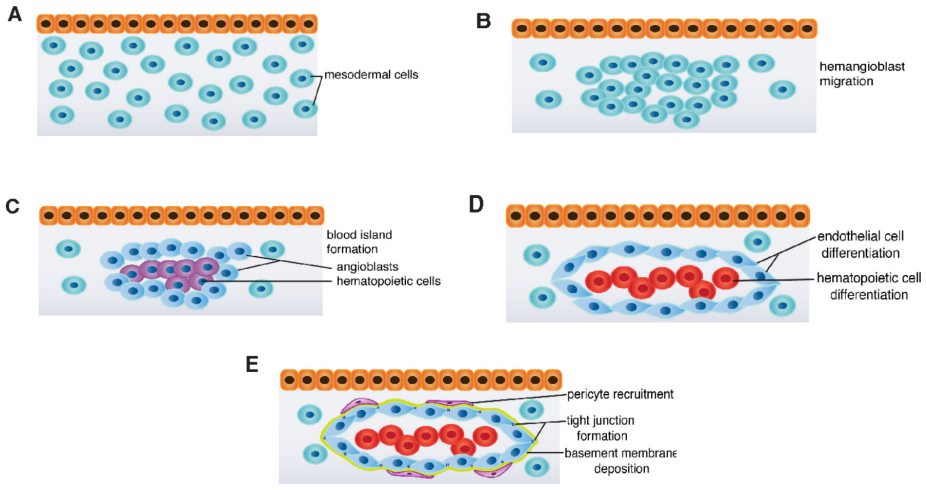

FIGURE 1.1: Diagram illustrating the different stages involved in vasculogenesis: Mesodermal cells differentiate (A), originating hemangioblasts that migrate and form a cluster (B). Blood island formation with angioblasts at the periphery and hematopoietic cells at the core (C). Hematopoietic and endothelial cell differentiation (D). Formation of the vascular lumen and vessel stabilization (E). Adapted from [1].

differentiation of endothelial precursor cells (EPC), also know as angioblasts. The first step in vasculogenesis is the aggregation of several cells called hemoangioblasts leading to the

formation of structures called blood islands. The majority of the cells located at the core of the blood islands will undergo apoptosis creating a lumen i.e. empty space. The cells at the cortex of blood islands will differentiate into endothelial precursor cells, while the cells that remained in the lumen will be blood cell precursors, or, hemopoietic cells. Several of these blood islands will coalesce with neighboring islands and form elongated structures called vascular cords which form the primary capillary plexus. During embryonic development, most of the main blood vessels in the circulatory system are formed by vasculogenesis and its occurrence drops drastically after birth. However, post-natal vasculogenesis has been shown to have an important role in both physio and pathological events such as tumor growth and wound healing [2]. At this stage, another process of blood network formation called angiogenesis takes a more important role in the development of the circulatory system.

1.1.2 Angiogenesis

Angiogenesis is the process by which new blood vessels are formed from preexisting ones. As such, in embryos, angiogenesis can only happen after vasculogenesis has already occurred and the primary capillary network has already been formed. As is the case with vasculogenesis, in angiogenesis new blood vessels are created in order to supply nutrients to cells whose distance to the closest vessel is bigger than the maximum diffusion length of most species. There are two types of angiogenesis: sprouting angiogenesis and splitting angiogenesis (also know as intussusceptive angiogenesis). Sprouting angiogenesis

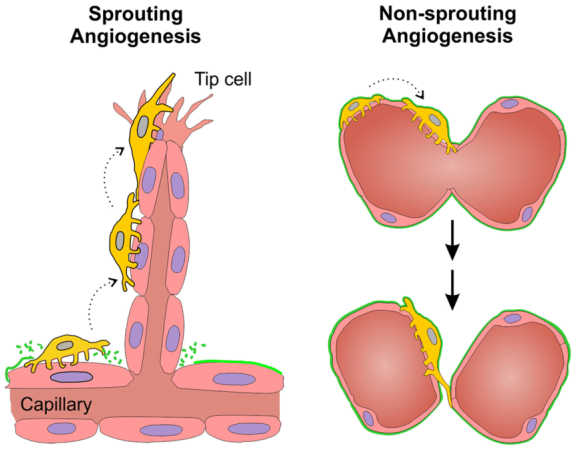

FIGURE 1.2: Differences between sprouting and non-sprouting (splitting) angiogenesis. Adapted from [3].

is characterized by the formation and elongation of sprout-like structures. These sprouts are formed by endothelial cells with two different phenotypes. The cell located at the front of the sprout is called a tip cell, while the cells located behind it are called stalk cells and provide support to the new sprout. The tip cell will migrate following the gradient of growth factors, while the stalk cells will proliferate extending the sprout towards the hypoxic center and providing stability to the new vessel. When two sprouts meet in space, they will connect with another one and form a loop where blood can flow, in a process called anastomosis. In splitting angiogenesis, a preexisting vessel originates two new vessels.

In this case, there is no cell proliferation or migration and instead the endothelial cells that form the original vessel rearrange themselves and create a wall that bissects the lumen, originating two new vessels.

1.1.3 Sprouting Angiogenesis

Sprouting angiogenesis is the most studied form of angiogenesis, not only because it was the first process to be observed for the formation of blood vessels, but primarily due to the intimate connection it had with the appearance and growth of solid tumors. In 1971, the American physician Judah Folkman published a seminal paper where the connection between tumor growth and angiogenesis was first reported [4]. In this work, Folkman also suggested how targeting angiogenesis could provide new therapeutic approaches in treating tumor progression. In the decades that followed, the study of sprouting angiogenesis has been very active, and its importance in understanding both physiological and pathological processes is now well established. It has been shown that sprouting angiogenesis plays a critical role in processes such as embryo development [5], wound healing [6, 7] and in the feminine reproductive cycle [8]. Its implication in diseases such as Type-II diabetes [9, 10], tumor growth [4] and cancer metastatic spread [11], endometriosis [12] and cardiovascular disease [13], further justifies the importance of understanding this complex process.

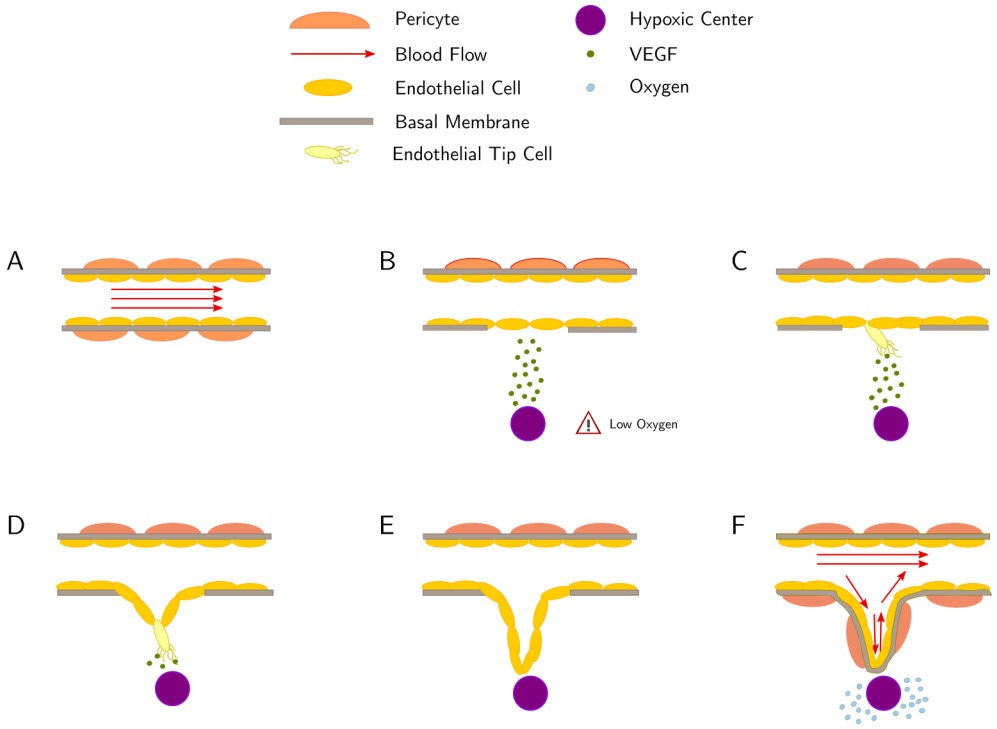

FIGURE 1.3: Illustration of the six main steps in the formation of a new vessel through sprouting angiogenesis: Preexisting stable vessel (A); VEGF from an hypoxic center reaches the vessel, and consequent destabilization and basement membrane degradation (B); Tip cell selection with filopodia formation (C); Tip cell migration towards the hypoxic center, following the gradient of VEGF, and stalk cell proliferation (D); The new sprout reaches the hypoxic center and VEGF production ceases (E); Stabilization of the new vessel and irrigation of the tissue, delivering oxygen (F).

The process of sprouting angiogenesis can be divided in six main steps, as illustrated

in Figure 1.3. At first, we have a preexisting vessel whose cells are in a quiescent state, meaning the vessel is stable, as there is no significant cell movement or proliferation and there is blood flowing in the lumen. In this phase, the vessel is surrounded by a basement membrane that provides stability to its structure, aided by the presence of pericytes (Figure 1.3A). In the second stage, somewhere in the tissue where the vessel is located, there is the appearance of an hypoxic center, which is a region where the concentration of oxygen is very low, threatening the survival of cells in its vicinity. The lack of oxygen induces the translation of hypoxia-inducible factors (HIFs) in the nucleus of the cells in the tissue. These transcription factors will, in turn, promote the production and release of growth factors, most importantly, vascular endothelial growth factor (VEGF), by the cells in hypoxia. Once VEGF is present in the extracellular matrix, it will diffuse in every direction, eventually reaching the capillary described in step one (Figure 1.3B). Endothelial cells have three specific VEGF receptors located at the cell membrane (VEGFR-1,2 and 3) and when these receptors are activated, the Delta-Notch pathway will also be activated, and as a result, some endothelial cells will undergo a phenotype change, becoming tip cells. Tip cells differ from quiescent cells through their proliferative rate but also through the formation of filopodia, cell membrane protrusions associated to the cytoskeleton, that allow cell migration through the ECM (Figure 1.3C). Before they start to migrate, tip cells must first destabilize the vessel they are a part of. They accomplish this by degrading the basement membrane that surrounds the vessel using matrix metalloproteinases (MMPs), which are enzymes capable of degrading the basement membrane, as well as the fibers that constitute the extracellular matrix. Once they are free to migrate through the ECM, endothelial tip cells will adopt a chemotactic behavior, characterized by their movement in the direction of the VEGF gradient that will lead them towards the hypoxic center. The cells that did not become tip cells, as a result of the Delta-Notch mechanism, will adopt the stalk cell phenotype. As opposed to tip cells, stalk cells do not alter their morphology by growing filopodia, but instead they will provide the necessary structure to the new sprout. As a result of cell-cell adhesion, stalk cells will follow the tip cell, while at the same time proliferating via cell division, adding new endothelial cells to the sprout, thus allowing for sprout elongation, as well as providing robustness to its structure (Figure 1.3D). As the initial sprout starts to become longer, some of the stalk cells may experience an up-regulation of VEGF receptors, thus becoming tip cells, leading to the branching of the sprout. At the same time, new lumen starts forming at the core region of the sprout, allowing for blood to flow in the newly formed vascular structures. Sprouts do not grow indefinitely, and when the new vessel network reaches the vicinity of the hypoxic center and is able to irrigate the surrounding tissue, both tip cell migratory and stalk cell proliferative behavior is down-regulated and the vessel network reaches the last phase of the angiogenic process, vessel maturation (Figure 1.3E). The process of vessel re-stabilization starts with the recruitment of pericytes that will attach themselves to the vessel, followed by the formation of a new basement membrane. This new vessel network will make sure oxygen and other nutrients are supplied to the surrounding tissue, as well as eliminating waste byproducts of cell activity (Figure 1.3F).

This simplified description of angiogenesis aims at providing a general overview of the complex process, avoiding some important details, some of which will be discussed in the following sections.

Vascular Endothelial Growth Factor

The VEGF protein family is a group of signaling proteins, produced by different kinds of cells, that is very important in the formation of new blood vessels. VEGF was first referenced in by Judah Folkman [14] who observed that tumors secreted a substance that stimulated the formation of new blood vessels in the tumor's vasculature. To this protein he gave the name of tumor angiogenesis factor (TAF). In the following decade, other authors identified the same protein in other settings and called it vascular permeability factor (VPF) [15], before being purified and isolated and named vascular endothelial growth factor [16].

VEGF plays a role in every step of sprouting angiogenesis and it is essential for endothelial cell migration and stalk cell proliferation. Besides those two functions, it also stimulates lumen formation in developing vessels and increases the permeability of blood vessels to chemical stimuli from the outside. It has been shown that the chemotactic movement along the gradient of VEGF is not exclusive to endothelial cells. Cells from the immune system such as macrophages (a white blood cell) can also follow VEGF cues towards inflammation spots, while also providing support to newly formed sprouts during angiogenesis [17]. It has been even described that at the front of each tip cell, a macrophage releasing MMPs and degrading cell and ECM debris is present [18].

Since its discovery, several VEGF proteins have been identified and studied, being divided into five families: VEGF-A, VEGF-B, VEGF-C, VEGF-D and, placental growth factor (PlGF). VEGF-C and VEGF-D have been identified as key modulators in lymphangiogenesis, the lymphatic system's equivalent to angiogenesis [19–21]. During embryogenesis, the placenta releases PlGF, which is important during vasculogenesis. VEGF-A is, by far, the most important growth factor family that is involved in angiogenesis, although VEGF-B also plays a part in the process but in a more supporting role. Four different VEGF-A isoforms, resulting from alternative splicing, have been identified and named after the number of amino-acids in their structure characterization ($VEGF_{121}$, $VEGF_{165}$, $VEGF_{189}$ and $VEGF_{206}$). Depending on their affinity to heparin, the dynamics of each isoform in the extracellular matrix can be very different, going from highly diffusive ($VEGF_{121}$), when there is no affinity, to being bound in the fibrous network ($VEGF_{189}$ and $VEGF_{206}$), when the affinity is high. $VEGF_{165}$ is know to have an intermediate affinity to heparin, being able to diffuse through the matrix while a significant amount is bound to the ECM and to the surface of cells. Matrix-bound VEGF can be released and become more diffusive due to the action of ECM-degrading enzymes, such as MMPs. What makes an endothelial cell sensitive to the existence of VEGF is the presence of specific receptors in its surface. Generally, there are three main VEGF receptors that can be found in cells: VEGFR-1, VEGFR-2 and VEGFR-3. Not all VEGF types bind to the same receptor and depending on

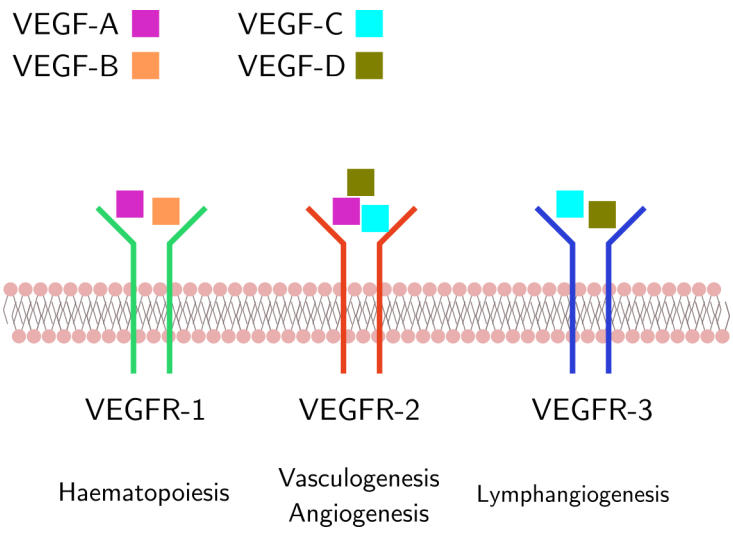

FIGURE 1.4: VEGF receptors located at the surface of cells, the VEGF forms that bind to each one, and the physiological processes they are involved in.

which receptor is activated, different cell responses can occur which can influence distinct physiological and pathological processes, as can be ssen in Figure 1.4.

1.1.4 Angiogenesis and the Extracellular Matrix

The extracellular matrix is present in all tissues and organs and its function is to provide a substrate and mechanical support for cellular activity, as well as mediate biochemical communication between cells and tissues that are connected by it. It has been shown that the interaction between cells and the ECM can also have effects on gene expression and can trigger cell apoptosis [22]. The ECM is organized as a three-dimensional network of fibers, minerals and proteins, although its composition can vary depending on where it is located in the body. The existence of an ECM in the vicinity of blood vessels, all around the circulatory system, makes it a subject of interest when studying angiogenesis. Most of the physical processes that are associated with angiogenesis, from cell migration to growth factor signaling and endothelial cell coordination, are largely dependent on the properties of the ECM and of its constituents.

As stated, the composition of the ECM is not the same everywhere in the body, although it is possible to identify a basic structure shared by the different matrices. The ECM can be divided into two main structures: the interstitial matrix and the extracellular basement membrane. The later is a layer that separates the matrix from the cells in the surroundings and it is mostly composed of collagen IV, laminins and heparin-derived proteoglycans. The interstitial matrix contains both fibrous and non-fibrous collagen, elastin and fibronectin. The combination of different amount of these constituents can lead to the existence of matrices with different mechanical properties, which in turn can influence their function and the behavior of cells located in their vicinity. In angiogenesis, specifically, the concentration of collagen and the distribution of fibrous components can highly influence cell migration,

in both pathological and homeostatic conditions, leading to vessel networks with different morphologies. How this occurs will be one of the main topics explored in this work.

Although the ECM is the substrate that allows endothelial cells to migrate during angiogenesis, at the same time it also constitutes an obstacle for cell movement. The fact that the matrix is a highly dynamic structure, subject to degradation and remodeling, is a key concept in understanding how cells can migrate through its complex organization. Matrix metalloproteinases, or MMPs, are enzymes capable of degrading both the extracellular basement membrane, as well as remodeling the fibers of the interstitial matrix. There are over twenty different types of MMPs, each specialized in degrading a specific type of substrates. The activity of MMPs can be inhibited due to the existence of protease activity regulators called tissue inhibitor of metalloproteinases, or TIMPs. MMP activation is dependent on the existence of a zinc atom with high catalytic properties, which TIMPs can bind to, thus inhibiting ECM degradation and remodeling.

In the context of angiogenesis, MMP production by endothelial cells is stimulated by the presence of growth factors such as VEGF and FGF, allowing cells to degrade the ECM, carving a path for sprout formation and neovascularization. Besides the role in remodeling the ECM, MMPs can also free some heavier VEGF isoforms that are less mobile and become trapped in the matrix due to their high heparin affinity. The VEGF that is released from the ECM will then reinforce the chemotactic behavior of endothelial tip cells, promoting cell migration. Similarly to what happens with VEGF, the role played by MMPs on angiogenesis, especially when it is tumor-induced, makes MMP inhibition a possible target for therapeutic strategies in cancer. Studies involving MMP knock-out mice have shown to reduce neovascularization and cell migration, both *in vitro* and *in vivo* [23, 24].

1.1.5 Tip/Stalk Cell Selection and the Notch Mechanism

In a stable, preexisting blood vessel in homeostatic conditions, the endothelial cells in its structure are in a quiescent state. In this state, cells are not being stimulated by external agents, and are characterized by very low motility and a non-proliferative behavior. This equilibrium can be disrupted when the vessel is subject to stimuli such as the release of growth factors by surrounding cells, specifically those in hypoxic or inflammatory conditions derived from both pathological or physiological events. When VEGF reaches the a vessel's endothelium, the process of vascular destabilization begins, marking the start of an angiogenic event, with cells abandoning their quiescent state and coordinating to perform the necessary functions. For sprout formation to occur, some cells will adopt an active migratory behavior and become endothelial tip cells, while the majority will provide a supporting role, proliferating and providing structure to the new sprout by forming tight junctions where cell-cell adhesion is strong. The mechanism through which endothelial cell coordination is determined, is the Notch signaling pathway. The importance of the Notch mechanism is underlined by the fact that it is a highly conserved system, meaning it is

present in the majority of all animals, maintained across the process of natural selection [25].

Notch is an inter-cellular communication pathway, and as such, it requires an interaction between cell ligands. Suppose we have two cells A and B that will interact via the Notch mechanism. Cell A is expressing Notch, a transmembranal protein that is composed of a portion located inside the cell and an extracellular part. Cell B, on the other hand, is expressing the Delta ligand located at the outside of the cell, anchored to its membrane. When the two cells are in proximity of each other, the exterior head of the Notch protein of cell A will bind to the Delta ligand (specifically, the Delta-like ligand 4, Dll4) in cell B. When the binding is complete, ADAM, a protease, cleaves the Notch protein in cell A, leaving its exterior head bound to the Delta ligand of cell B, while its intracellular component is left hanging on the cell interface. Through specific enzymatic activity, the intracellular portion of Notch, now called Notch intracellular cleaved domain (NICD) will be released from the interface and internalized, traveling to the nucleus of cell A, where it will trigger transcription mechanisms resulting in cell proliferation. Meanwhile, the Delta-Notch complex, located on the outside of cell B, will also be internalized by endocytosis.

When VEGF reaches the endothelial cells at the start of angiogenesis, some cells will become tip cells. Tip cells will present a low level of Notch protein and a high concentration of Delta ligands at their surface. When tip cells interact with other endothelial cells in their vicinity, those cells will increase their levels of Notch, promoting transcription and at the same time, increase their proliferative capacity and reduce the levels of VEGFR-2 in their surface, while downregulating the expresssion of Delta. The process by which tip cells influence the phenotype of their neighboring cells is called lateral inhibition [26, 27]. Since the process of lateral inhibition was first introduced, it has been widely included in computational models of angiogenesis, both in great detail or simply in the consequences it has on endothelial cell phenotype [28–30]. Although, in this work, we will focus on the role the Delta-Notch mechanism plays in angiogenesis, it is worth mentioning that the concept of lateral inhibition has been identified in other biological systems, such as neurogenesis (differentiation of neuroblasts into neurons).

1.1.6 EC-EC and EC-ECM Mechanical Interactions

Cell migration is one of the most important processes involved in angiogenesis. Sir Isaac Newton postulated in his Second Law of Motion for a body to move, that there must exist an external force that set the body in motion by acting on it [31]. Thus, for cell movement to occur, there must be a set of forces that act on the cell that initiate and sustain movement. Endogenous forces are the ones generated by the cells on their surroundings, as a result of the dynamics of their cytoskeleton. The forces that are applied to the cell by some external agent, such as gravity, are called exogenous forces. In the specific case of angiogenesis, two of the most important forces that result in cell movement and sprout formation are endothelial cell-cell adhesion and tip cell traction forces, exerted by the tip

cell leading the sprout on the ECM that serves substrate for migration. In late stages of vascular network formation and remodeling, blood flow shear stress is also an important force to consider, specifically when studying vessel pruning and regression.

Endothelial cell-cell adhesion is a fundamental interaction that assures tissue connectivity, stability and permeability. Similar to the Delta-Notch mechanism discussed in the previous section, cell-cell adhesion is possible due to the existence of transmembrane proteins that mediate the interaction between the cytoskeleton of one cell and the other. Cadherins is a family of proteins that is one of the most important mediators of cell-cell adhesion. Besides their importance in angiogenesis, these proteins are also involved in embryonic development, tumor metastasis and morphogenesis. The cadherin protein family is extensive, however, for cell-cell adhesion in angiogenesis, the most relevant member is cadherin-5, also know as VE-cadherin (vascular endothelium-cadherin). Cadherins get their name since they depend on the concentration of calcium ions to function, and they act through the interaction of their intracellular domains with the actin cytoskeleton. The importance of VE-cadherin in vascular development has been supported by experimental work with mouse models, where it was observed that in VE-cadherin KO mouse embryons, the newly formed vessels where not able to maintain their integrity and would collapse, resulting in embryonic death [32]. Despite the importance of cell-cell adhesion, this interaction alone is not sufficient to

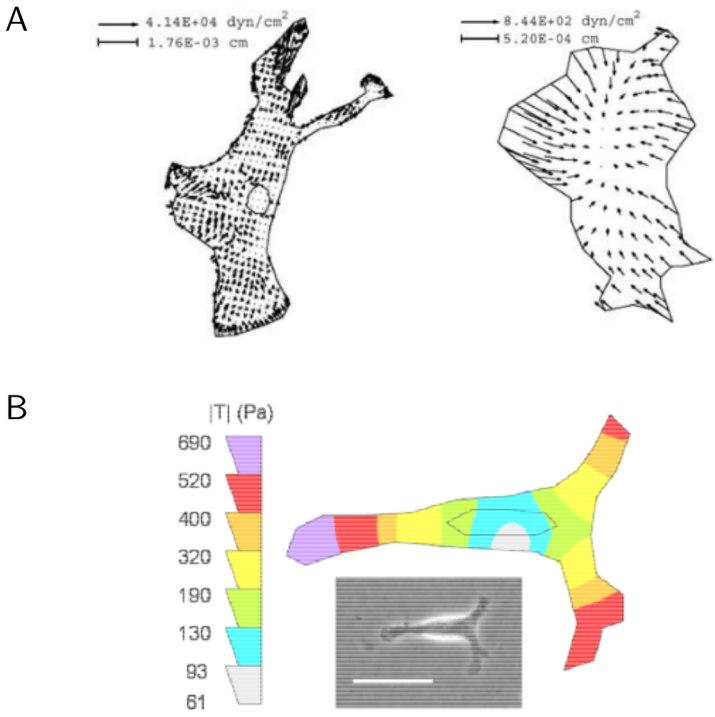

FIGURE 1.5: Endothelial cell traction forces measured using Traction Force Microscopy. Traction force vector fields calculated for an endothelial cell spreading in a substrate (A). Force magnitude colormap measured for a cell (B). Adapted from [33] (A) and [34] (B).

explain cell movement. Tip cell migration occurs mostly due to its mechanical interaction with the ECM. The morphological changes an endothelial cell undergoes when the tip cell phenotype is assigned to it, most importantly the formation of filopodia, along with its

high concentration of VEGFR2 receptors, increase its sensitivity to growth factor gradients. In order to move, tip cells must exert a force on the ECM. This force is the result of internal forces generated by the cell's cytoskeleton and the formation of focal adhesions between the matrix and the tip cell's filopodia. The tip cell extends its filopodia which will form strong connections to the ECM. Meanwhile, in the rear of the cell, the action of acto-myosin propels the cell forward. This type of crawling behavior is what allows cells to migrate and create elongated sprouts. The traction force field created by endothelial cells has been measured experimentally in the context of a cell spreading on a substrate [33, 34]. In Figure 1.5A we can see vector field representations of the traction force exerted by an endothelial cell on a soft substrate. We can see that the arrows point, approximately, to the center of the cell. Looking at the size of the arrows and at the colormap in Figure 1.5B, we see that forces are more intense closer to the cell interface, while near the cell geometric center they have a lower magnitude.

1.2 Cell Cytoskeleton

Inside an animal cell there are a number of organelles, each performing one or more specific tasks. In order for the cell not to collapse on itself, there must be some structure that holds the cell together, providing stability. This task is performed by a set of protein filaments, that together form what is called the cytoskeleton. As the word itself suggests,the cytoskeleton is the skeleton of the cell, performing tasks much like the human skeleton, as it is involved in providing structural support to the cell, as well as allowing the cell to move, while also aiding the inter-organelle transport of materials inside the cell. Besides these main functions, the cytoskeleton is also responsible for cells maintaining or changing their shape, for example, during processes such as cell division, or in response to external mechanical perturbations. The proteins that form the cytoskeleton can be divided into three groups, depending on the size of the fibers they form, as well as their chemical structure and function. These groups are microtubules, intermediate filaments and microfilaments.

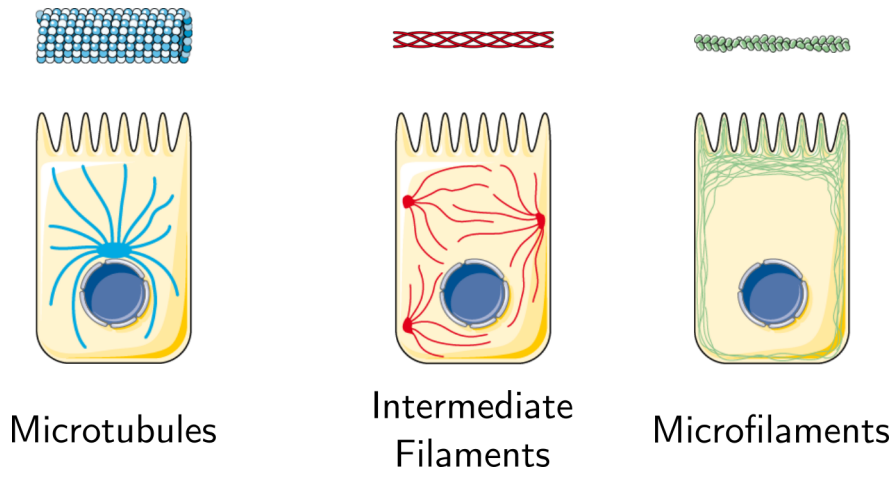

FIGURE 1.6: Group of protein filaments that constitute the cytoskeleton, their filament structure and usual distribution on the cytoplasm.

1.2.1 Microtubules

Microtubules are cylindrical fibers (Figure 1.6 Left) of $\approx$ 20 nm in diameter, made up of bundles of proto-filaments of α and β tubulin dimers. They are able to transport cell organelles like mitochondria, as well as vesicles secreted by other cell components. They are also the main protein found in cilia and flagella of cells, like spermatozoa, that allow them to move using self-propulsion. In plant cells, they are also found in the cell wall. Perhaps the most important function of microtubules is their role in cell division. The mitotic spindle, the apparatus that forms during metaphase, and that is responsible for the separation of chromosomes, is composed of microtubules that span from the centrosomes and bind to the chromatids that will be divided between the two daughter cells. Neurons also have microtubules in their structure, where they go by the name of neurotubules and participate, for example, in the transport of neurotransmitters.

1.2.2 Microfilaments/Actin Filaments

The cytoskeleton's microfilaments or, most commonly, actin filaments, are protein fibers that have $\approx$ 7 nm in diameter and are made of two helical strands of actin subunits that interlace. They participate in many cell processes like cell movement and force generation, cell shape changes, cell contractility and mechanical resistance, as well as playing a fundamental role in separating the two daughter cells resulting from mitosis.

The actin filament's structure provides flexibility to the fiber, while also granting it with a high resistance to filaments fracture. The subunits that make up an actin fiber, usually refered as F-actin, are called globular actin (G-actin). Actin fiber assembly is an asymmetric process characterized by the existence of a slow growing end, usually refered as the (-) or pointed end, and a fast growing end, called the (+) or barbed end. This means that an actin filament is naturally polarized since the addition of new actin subunits at the (+) end is faster than at the (-) end. The first step in the formation of an actin fiber is the nucleation step, where small actin monomers bind to each other forming a stable trimer called the nucleus. Nucleation is the slowest step in the actin filament process but it can be accelerated if there are fragments of preexisting actin filaments in the vicinity. Next, the process of filament elongation begins, characterized by the addition of actin monomers to both ends of the filament, until the steady state is reached. This state corresponds to a dynamic equilibrium where the addition of monomers to the minus and plus ends occur at the same rate.

The actin cytoskeleton formation and function is highly dependent on the existence of accessory proteins that are involved in the steps of actin filament formation, as well as in the organization of those filaments in bundles and/or networks. Some of these auxiliary proteins, and the role they play in actin dynamics are:

- Formin: Nucleating site assembly;
- Arp2/3 complex: Nucleates assembly to form a branched network;

- Profilin: Binds actin monomers, concentrating them on assembly sites;
- Tropomyosin: Stabilizes filaments and mediates the binding of other accessory proteins;
- Fimbrin and α-actinin: Controls the spacing between actin fibers when bundling;
- Filamin: Cross-links actin fibers in networks;
- Spectrin: Binds the actin filament network to the plasma membrane.

1.2.3 Intermediate Filaments

Intermediate filaments (IFs) get their name from the fact that their average diameter is in between that of actin filaments and microtubules, at ≈ 10 nm. The main function of intermediate filaments is to provide mechanical integrity to the cell, specially when it is subject to external stress. They are also know to mediate cell-cell and cell-ECM adhesion by interacting, respectively, with desmosomes and hemidesmosomes. The biomechanical properties of IFs are what allows them to maintain cell stability and resist stress. IFs are easily deformable proteins, and can also stretch up to three times their natural length without breaking, due to their alpha-helix structure.

Based on their amino-acid sequence, intermediate filaments have been grouped into five categories. Type I and II IFs correspond, respectively, to acidic and basic keratins, that are found in epithelial cells. Type III IFs include vimentin (endothelial cells, fibroblasts and leukocytes) and desmin (muscle cells). The Type IV group contains the neurofilaments, found in the axons of neurons. Finally, Type V IFs are the so called nuclear lamins. While all other four kinds of intermediate filaments are generally found in the cytoplasm, lamins have a structural function in the cell nucleus. In this work, our focus will be on the keratin IF cytoskeleton and how mutations in genes that regulate its expression can lead to different IF network configurations.

1.2.4 Keratin Cytoskeleton

Sequencing of the human genome revealed there are 54 different keratin genes, making it the most diverse family of intermediate filaments. 28 of these genes code type I, acidic keratins, while the other 26 correspond to type II, basic keratins [35]. Acidic keratins are named so since they possess more acidic amino acids like aspartic acid, while basic keratins contain a surplus of basic amino acids like lysine [36]. Keratin dimers are always heterodimers, resulting from the pairing of an acidic and a basic keratin form. Keratins can also be classified as hard or soft depending on their cysteine levels. Hard keratins contain a higher amount of cysteine causing the resulting filaments to be able to sustain higher forces without breaking up, and these are usually found in the constitution of hair, nails and animal horns. Soft keratins are more flexible and have a more elastic behavior, and are present in keratinocytes that make up the layers of the skin. These characteristics are consistent with the role of the keratin cytoskeleton in guaranteeing epithelial cell

mechanical stability and protection against mechanical stress. It has also been shown that this intermediate filament network may also play a part in shielding the cell against stress such as heat, as well as assuring organelle homeostasis [37].

The basic unit of a keratin filament is the heterodimer, as previously mentioned. Two heterodimers are anti-parallel aligned to one another and form a tetramer. When two tetramers bind laterally, they form an octamer, also know as a proto-fibril. Unit length filaments (ULFs) are a result of the side-by-side association of four proto-fibrils, and the end-to-end association of ULFs results in a basic keratin filament. After packing, a keratin filament has a length of ≈ 10 nm.

The keratin network inside a cell is not static but highly dynamic, being in a continuous cycle of assembly/disassembly. In 2011, a work was published that presented an hypothesis for the several steps involved in the keratin cycle, shown in Figure 1.7 [38]. This process

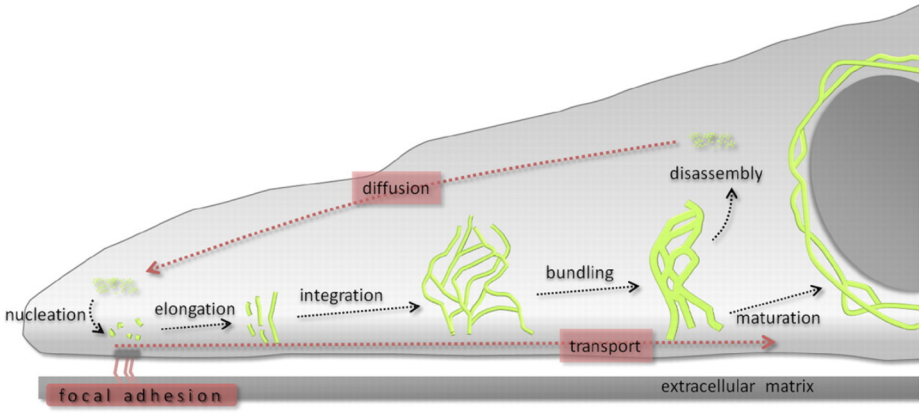

FIGURE 1.7: Diagram of the keratin assembly and disassembly cycle, showing the different steps of the process. Adapted from [38].

begins near the cell membrane, in regions where the cell is anchored to the ECM via focal adhesions. There, soluble keratin oligomers group together to form small particles, in a process called nucleation. Over time, these particles assemble into filaments that are being transported along the actin cytoskeleton fibers in the direction of the nucleus. These new fibers join the already formed network located in the periphery of the nucleus, where they will bundle and mature, forming a dense keratin filament network. Concurrently, these same fibers start disassembling back to soluble oligomers, which due to their small size and high solubility in the cytoplasm water content, diffuse to the regions near to the cell membrane, where the cycle restarts. This process of keratin disassembly is a result of the action of proteosomes and it is a fundamental process, since high densities of intermediate filaments could interfere with other cellular functions [39]. The hypothesis of a recycling keratin process is further supported by the fact that it is a more efficient process than *de novo* synthesis of new keratin, and considering that actin also undergoes an assembly and disassembly cycle.

1.2.5 Keratin Mutations and Disease

Mutations in keratin expressing genes have been linked to a number of pathologies, commonly known as keratinopathies, such as: corneal dystrophy (K3/K12), white sponge nevus (K4/K13) and liver disease and inflammatory bowel disease (K8/K18 and K19) [40]. The pathologies are often characterized by the dysfunctional assembly of keratin filaments, resulting in the formation of aggregates, impairing the structure and function of epithelial cells. In the basal layer of the skin, the innermost layer of the epidermis where cells are constantly dividing, keratinocytes form K14/K5 heterodimers and mutations in one, or both of these keratin forms causes epidermolysis bullosa simplex (EBS), a congenital disorder. The disruption of keratin filament formation caused by this mutation leads to the malfunction of basal keratinocytes, resulting in the formation of bulbous structures in the epidermis which, combined with an increase in epithelial cell motility, leads to skin fragility and blistering. Cells with a mutated K14 protein react differently to external stress altering the constitutive structure of the skin.

In this work, we will focus on studying the K14-R125P keratin mutation, which is caused by the replacement of an arginine (R) amino acid, located at position 125, by a proline (P).

Chapter 2

Mathematical and Modeling Concepts

2.1 Calculus of Variations

2.1.1 Functionals

A function f is a map that makes a correspondence between each element of a set X (called the domain) and a unique element of another set Y (called the co-domain). Using mathematical notation, this definition is written as

$$f : X \to Y \,. \tag{2.1}$$

In the fields of physics and applied mathematics, we regularly come across functions where the domain and co-domain are both the set of all real numbers $\mathbb{R}$.

A functional is also a map that corresponds an element from a set to the set of real numbers. The difference being that, a functional, instead of mapping a number to another number, makes a correspondence between a function and a number. Mathematically, the definition of a functional F that takes a function $f(x)$ and returns a number is written as

$$F : \{f(x) \mid x \in \mathbb{R}\} \to \mathbb{R} \,.$$

When we want to write the expression of a functional the following notation is used:

$$F[f(x)] = \quad \cdots \,.$$

which defines a functional F that takes a function $f(x)$ and returns a number.

Perhaps the most common type of functional we are accustomed to is the integral.

$$A[f(x)] = \int_a^b f(x)\,\mathrm{d}x \tag{2.2}$$

is a functional that calculates the area beneath a curve described by $y = f(x)$ between the points $x = a$ and $x = b$, or simply, the definite integral of $f(x)$ between a and b. A function can also be interpreted as a functional. The following integral

$$F[g(x)] = \int_{-\infty}^{+\infty} g(x)\delta(x - x_0)\,\mathrm{d}x = g(x_0) \tag{2.3}$$

takes a function $g(x)$ as input, integrates its product with the Dirac delta function, $\delta(x-x_0)$, and, using the properties of the delta function, returns $g(x_0)$.

Perhaps one of the most important functionals in physics is the action of a classical system, which is the basis for the development of the Lagrangian formalism

$$S[L(q_i(t), \dot{q}_i(t), t)] = \int_{t_1}^{t_2} L(q_i(t), \dot{q}_i(t), t)\,\mathrm{d}t \tag{2.4}$$

where $L(q_i(t), \dot{q}_i(t), t)$ is the Lagrangian of the system as a function of the generalized coordinates and velocities. In some cases, an explicit dependence on the time variable is also present.

2.1.2 Extrema of a Functional

Often we want to find the minima and maxima of a certain function f. At these points, a small change in the value of x produces no change in the value of $f(x)$ i.e. the derivative of f with respect to x is equal to zero. We can write this statement as

$$\mathrm{d}f = f(x + \mathrm{d}x) - f(x) = 0\,, \tag{2.5}$$

in the limit $\mathrm{d}x \to 0$

The same idea can be applied to a functional. Suppose we want to find the function $f(x)$ that leads to a maximum or minimum value of a certain functional $F[f(x)]$. This means that the variation in the value of F when $f(x)$ suffers an infinitesimal deviation $\delta f(x)$ is zero, or

$$\delta F = F[f + \delta f] - F[f] = 0\,. \tag{2.6}$$

2.1.3 Euler-Lagrange Equations

The stationary action principle of a classical system states that the time evolution of the generalized coordinates is such that

$$\delta S = 0\,,$$

where the action functional, S, is defined in 2.4. Calculating the value of the action when the coordinates are slightly changed we write

$$S\left[q_i + \delta q_i, \dot{q}_i + \delta\dot{q}_i, t\right] = \int_{t_1}^{t_2} L(q_i + \delta q_i, \dot{q}_i + \delta\dot{q}_i, t)\,\mathrm{d}t\ ,$$

which, in the case of very small δq_i and $\delta \dot{q}_i$, can be expanded using the Taylor series as

$$S\left[q_i + \delta q_i, \dot{q}_i + \delta \dot{q}_i, t\right] = \int_{t_1}^{t_2} \left[L(q_i, \dot{q}_i, t) + \frac{\partial L}{\partial q_i}\delta q_i + \frac{\partial L}{\partial \dot{q}_i}\delta \dot{q}_i \right] \mathrm{d}t \ .$$

Using the definition of δS and integrating the third term in the integral by parts we have

$$\delta S = \int_{t_1}^{t_2} \left(\frac{\partial L}{\partial q_i}\delta q_i - \frac{\mathrm{d}}{\mathrm{d}t}\left(\frac{\partial L}{\partial \dot{q}_i}\right)\delta q_i \right) \mathrm{d}t + \left. \frac{\partial L}{\partial \dot{q}_i}\delta q_i \right|_{t_1}^{t_2} .$$

Assuming that at both ends of the trajectory we have $\delta q_i(t_1) = \delta q_i(t_2) = 0$, we are left with

$$\delta S = \int_{t_1}^{t_2} \left(\frac{\partial L}{\partial q_i} - \frac{\mathrm{d}}{\mathrm{d}t}\frac{\partial L}{\partial \dot{q}_i} \right) \delta q_i \, \mathrm{d}t \ .$$

For the stationary action principle to be verified at every point of the trajectory, independently of whatever deviation δq_i we choose, the integrand in the previous equation must be equal to zero. This last condition gives us the Euler-Lagrange equations for a classical system

$$\frac{\mathrm{d}}{\mathrm{d}t}\left(\frac{\partial L}{\partial \dot{q}_i}\right) = \frac{\partial L}{\partial q_i} \, . \tag{2.7}$$

Although, here we showed how to minimize a functional using a concrete example from classical physics, this procedure is still valid for other minimization/maximization problems.

2.2 Fourier Transforms and PDEs

The Fourier transform of a function $f(\mathbf{r})$, denoted by $\hat{f}(\mathbf{k})$, is defined as

$$\mathcal{F}(f) = \hat{f}(\mathbf{k}) = \int_{-\infty}^{+\infty} f(\mathbf{r}) e^{i\mathbf{k}\cdot\mathbf{r}} \, \mathrm{d}\mathbf{r} \tag{2.8}$$

and it serves as a way to change between a function's real space representation and its representation in reciprocal space. This transform is useful as a result of several properties that come from its definition. For instance, the Fourier transform of the derivative of a function, $f(x)$ is given by

$$\begin{aligned} \mathcal{F}\left(\frac{\mathrm{d}f}{\mathrm{d}x}\right) &= \int_{-\infty}^{+\infty} \frac{\mathrm{d}f}{\mathrm{d}x} e^{ikx} \, \mathrm{d}x \\ &= \int_{-\infty}^{+\infty} ikf(x)e^{ikx} \, \mathrm{d}x - f(x)e^{ikx}\Big|_{-\infty}^{+\infty} \end{aligned}$$

Under the condition that $\lim_{x\to\pm\infty} f(x) = 0$, we have that

$$\mathcal{F}\left(\frac{\mathrm{d}f}{\mathrm{d}x}\right) = ik\int_{-\infty}^{+\infty} f(x)e^{ikx} \, \mathrm{d}x = ik\hat{f}(k)$$

which by repeating the process results in

$$\mathcal{F}\left\{\frac{\mathrm{d}^n f}{\mathrm{d}x^n}\right\} = (ik)^n \hat{f}(k)\,.$$

This property of the Fourier transform turns the derivative from a differential operator into a simpler algebraic operation.

2.2.1 Poisson Equation - An example

The best way to show how Fourier transforms can simplify the solution of some problems is to exemplify how we can solve, for example, the Poisson equation

$$\nabla^2 u = f(\mathbf{r})$$

when subject to periodic boundary conditions. This equation has a unique solution in a domain with periodic boundary conditions provided we set its average value in the domain. In three dimensions, the above equation in its more explicit form is

$$\frac{\partial^2 u}{\partial x^2} + \frac{\partial^2 u}{\partial y^2} + \frac{\partial^2 u}{\partial z^2} = f(x, y, z)$$

and after applying the Fourier transform to the left and right side of the equation we end up with

$$(-k_x^2 - k_y^2 - k_z^2)\ \hat{u}(k_x, k_y, k_z) = \hat{f}(k_x, k_y, k_z)$$

which is now a simple algebraic equation with a solution given by

$$\hat{u}(\mathbf{k}) = -\frac{\hat{f}(\mathbf{k})}{|\mathbf{k}|^2}\,.$$

We should note, however, that at this point the solution for the equation is still in its reciprocal space representation, meaning we have to apply the inverse Fourier Transform to get the solution in real space. Another question that arises when we look at the solution is what happens when $|\mathbf{k}| = 0$. The only way to make this solution valid at $|\mathbf{k}| = 0$ is for $\hat{f}(\mathbf{k} = 0)$ to also be zero. According to the Fourier transform definition, $\hat{u}(\mathbf{k} = 0)$ is equal to the average of $u(\mathbf{r})$ in the domain.

2.3 Theory of Linear Elasticity

When a force is applied to a certain body it tends to change its shape or volume and we say that the body has suffered a deformation. Afterwards, when the applied force ceases, the body tends to relax towards its initial configuration. A body that is able to restore its exact previous configuration is called perfectly elastic. In this work we will only deal with systems that have this characteristic. The way to mathematically describe the deformations of continuous media is by using the classical theory of elasticity.

2.3.1 Displacement

Suppose we choose a certain point P with coordinates $\mathbf{r} = x_1\hat{e}_x + x_2\hat{e}_y + x_3\hat{e}_z$ that is part of a certain elastic body that is at rest. After the body is deformed, the coordinates of point P will change to $\mathbf{r}' = x_1'\hat{e}_x + x_2'\hat{e}_y + x_3'\hat{e}_z$. The difference between the position of point P before and after deformation is called the displacement u_i (in Einstein notation)

$$u_i = r_i' - r_i \,. \tag{2.9}$$

In a first approximation we will consider that r_i' is simply a function of r_i i.e. $r_i'(r_i)$ and, consequently $u_i(r_i)$.

2.3.2 Strain Tensor

Let us consider two points P_1 and P_2 that are very close together. Before the deformation, the length of a vector $\mathbf{x}$ that starts at P_1 and points towards P_2 is given by $\mathrm{d}l = \sqrt{\mathrm{d}x_i^2}$. After the body is perturbed, the distance between the two points changes to $\mathrm{d}l' = \sqrt{\mathrm{d}x_i'^2}$. Knowing that $\mathrm{d}x_i' = \mathrm{d}x_i + \mathrm{d}u_i$ we can write $\mathrm{d}l'^2 = (\mathrm{d}x_i + \mathrm{d}u_i)^2$ and applying the chain rule we can write $\mathrm{d}u_i$ as $\mathrm{d}u_i = \frac{\partial u_i}{\partial x_j}\,\mathrm{d}x_j$ and consequently

$$\begin{aligned}\mathrm{d}l'^2 &= \left(\mathrm{d}x_i + \frac{\partial u_i}{\partial x_j}\,\mathrm{d}x_j\right)^2 \\ &= \mathrm{d}x_i^2 + 2\frac{\partial u_i}{\partial x_j}\,\mathrm{d}x_i\,\mathrm{d}x_j + \frac{\partial u_i}{\partial x_j}\frac{\partial u_i}{\partial x_k}\,\mathrm{d}x_j\,\mathrm{d}x_k \,.\end{aligned}$$

When the external stress applied to the body leads to small deformations, we can neglect terms of order higher than one on the displacement u_i. This leads to the theory of linear elasticity. Using this approximation in the above expression, and writing the second term in a symmetric form, we get

$$\mathrm{d}l'^2 = \mathrm{d}l^2 + \left(\frac{\partial u_i}{\partial x_j} + \frac{\partial u_j}{\partial x_i}\right)\mathrm{d}x_i\,\mathrm{d}x_j = \mathrm{d}l^2 + 2\varepsilon_{ij}\,\mathrm{d}x_i\,\mathrm{d}x_j$$

where ε_{ij} are the components of the strain tensor (in linear elasticity) defined as

$$\varepsilon_{ij} = \frac{1}{2}\left(\frac{\partial u_i}{\partial x_j} + \frac{\partial u_j}{\partial x_i}\right) . \tag{2.10}$$

By construction the strain tensor is symmetric, meaning that $\varepsilon_{ij} = \varepsilon_{ji}$. Another interesting property is the geometric interpretation of is trace, ε_{ii}. Considering an infinitesimal vector along the x coordinate axis, then $\mathrm{d}x' = \mathrm{d}x + \frac{\partial u_x}{\partial x} = (1 + \varepsilon_{xx})$. A similar expression is obtained for the y and z directions.

The volume of an infinitesimal portion of the body $\mathrm{d}V = \mathrm{d}x\,\mathrm{d}y\,\mathrm{d}z$, after the deformation is given by

$$\mathrm{d}V' = \mathrm{d}x'\,\mathrm{d}y'\,\mathrm{d}z' = (1+\varepsilon_{xx})(1+\varepsilon_{yy})(1+\varepsilon_{zz})\,\mathrm{d}x\,\mathrm{d}y\,\mathrm{d}z$$

and if we keep only the linear terms of ε_{ij} we get

$$\mathrm{d}V' = (\varepsilon_{ii} + 1)\,\mathrm{d}V$$

or

$$\frac{\delta V}{V} = \varepsilon_{ii} = \mathrm{tr}(\varepsilon) \tag{2.11}$$

2.3.3 Stress Tensor

When a body is at rest and is not being deformed, that body is in mechanical equilibrium. If a force is applied to an elastic body, the internal arrangement of its constituents changes. In linear elasticity, when the force stops, those constituents will move back to their original positions. This is analogous to what happens when we have a spring-block system at rest and we move the block from its resting place. In that case a restorative force tries to bring the block back to its starting position and using Hooke's law we can calculate that force. Suppose we take a small piece of the body and we calculate the total force applied in that volume

$$F_i^{\mathrm{total}} = \int_V f_i \,\mathrm{d}\mathbf{r} \ ,$$

where f_i is the force per unit of volume. If we assume that f_i can be written as the divergence of a tensor with rank 2, and use Gauss's theorem of vector calculus, we transform the integral over the volume V to an integral over the surface, S, that encloses that same volume.

$$F_i^{\mathrm{total}} = \int_V \frac{\partial \sigma_{ij}}{\partial x_j}\,\mathrm{d}\mathbf{r} = \int_S \sigma_{ij}\,\mathrm{d}S_j$$

where σ_{ij} is called the stress tensor. Each component of the stress tensor, σ_{ij}, gives the force in the i^{th} direction on a surface element whose normal vector is given by $\mathrm{d}S_j$.

2.3.4 Mechanical Equilibrium

From Newtonian particle mechanics we know that for a particle to be in equilibrium two conditions must be satisfied: the sum of all forces applied to the particle must be null, as well as the sum of the moment of those same forces, i.e.

$$\Sigma_i F_i = 0$$
$$\Sigma_i \tau_i = 0\,.$$

In the study of continuous media, the equilibrium conditions are the same, but they must be true in the whole extension of the body. From the previous section we learned that the forces in an elastic body are given by

$$F_i = \int_V \left(\frac{\partial \sigma_{ij}}{\partial x_j} + f_i^{\mathrm{ext}} \right) \mathrm{d}\mathbf{r}$$

where f_i^{ext} represents external forces applied to the body. For the total force to be zero the equilibrium condition must be true for every infinitesimal element, so

$$\partial_j \sigma_{ij} + f_i^{\text{ext}} = 0\,. \tag{2.12}$$

The torque, τ_k,that is applied to the body is given by

$$\tau_k = \int_S \epsilon_{ijk} x_i \sigma_{jl}\,\mathrm{d}S_l + \int_V \epsilon_{ijk} x_i f_j^{\text{ext}}\,\mathrm{d}\mathbf{r}$$

where the first term is the moment of the internal forces of the elastic body and the second one is the torque caused by external forces. Using Gauss's Theorem the first integral can be turned into a volume integral of a divergence

$$\begin{aligned}\tau_k &= \int_V \partial_l \left(\epsilon_{ijk} x_i \sigma_{jl}\right)\mathrm{d}\mathbf{r} + \int_V \epsilon_{ijk} x_i f_j^{\text{ext}}\,\mathrm{d}\mathbf{r} \\ &= \int_V \left(\epsilon_{ijk}\delta_{il}\sigma_{jl} + \epsilon_{ijk} x_i \partial_l \sigma_{jl} + \epsilon_{ijk} x_i f_j^{\text{ext}}\right)\mathrm{d}\mathbf{r}\end{aligned}$$

and making use of equation 2.12 we are left with only one term

$$\tau_k = \int_V \epsilon_{ijk}\sigma_{ji}\,\mathrm{d}\mathbf{r}$$

which is zero when the body is in mechanical equilibrium. This is only true everywhere in the body if

$$\epsilon_{ijk}\sigma_{ji} = 0$$

or

$$\sigma_{ij} = \sigma_{ji} \tag{2.13}$$

i.e. the stress tensor must be symmetric. The physical interpretation of this symmetry is that in the case of mechanical equilibrium, the angular momentum (L_k) of the body is conserved. This comes from the fact that

$$\tau_k = \dot{L}_k\,.$$

2.3.5 Elastic Energy

The work done by forces in an elastic system, W, is equal to the change of energy when the displacement is incremented by a small factor δu_i and is equal to

$$\begin{aligned}W &= \int_S \sigma_{ij}\delta u_i\,\mathrm{d}S_j + \int_V f_i^{\text{ext}}\delta u_i\,\mathrm{d}\mathbf{r} \\ &= \int_V \left[\partial_j\left(\sigma_{ij}\delta u_i\right) + f_i^{\text{ext}}\delta u_i\right]\mathrm{d}\mathbf{r} \\ &= \int_V \left[\left(\partial_j\sigma_{ij} + f_i^{\text{ext}}\right)\delta u_i + \sigma_{ij}\partial_j\delta u_i\right]\mathrm{d}\mathbf{r}\,.\end{aligned}$$

In the case where the displacement δu_i is quasi-static, meaning it is so small it does not disturb the mechanical equilibrium, the first parcel in the integral is zero and we are left

with

$$W = \int_V \sigma_{ij}\partial_j \delta u_i \,\mathrm{d}\mathbf{r} = \frac{1}{2}\int_V (\sigma_{ij}\partial_j \delta u_i + \sigma_{ji}\partial_i \delta u_j)\,\mathrm{d}\mathbf{r}$$
$$= \int_V \sigma_{ij}\delta\varepsilon_{ij}\,\mathrm{d}\mathbf{r}$$

where the integrand represents the variation of elastic energy per volume, i.e.

$$\delta U = \sigma_{ij}\delta\varepsilon_{ij} \tag{2.14}$$

Consequently, the density of elastic energy is given by

$$U = \int \sigma_{ij}\,\mathrm{d}\varepsilon_{ij} \tag{2.15}$$

In the elastic regime, we assume that the stress depends linearly on the displacements. We can write without loss of generality that

$$\sigma_{ij} = C_{ijkl}\varepsilon_{kl} \tag{2.16}$$

where C_{ijkl} is a fourth order tensor called the elasticity tensor.

$$\delta U = C_{ijkl}\varepsilon_{kl}\delta\varepsilon_{ij}$$
$$= \frac{1}{2}C_{ijkl}\delta\left(\varepsilon_{ij}\varepsilon_{kl}\right)$$

and

$$U = \frac{1}{2}C_{ijkl}\varepsilon_{ij}\varepsilon_{kl} = \frac{1}{2}\sigma_{ij}\varepsilon_{ij} \tag{2.17}$$

2.3.6 Linear, Isotropic Materials

If we rotate an elastic material around any axis and we observe that its mechanical properties remain unchanged then the elastic material is isotropic. To obey these symmetries, the energy must be proportional to combinations of ε_{ij} that are scalars. Therefore, we need to find which terms of $\varepsilon_{ij}\varepsilon_{kl}$ produce a scalar. The only way to produce a scalar from a product of this kind is by contracting indices. In this case, there are two ways to do it:

$$\varepsilon_{ij}\varepsilon_{kl}\delta_{ij}\delta_{kl} = \varepsilon_{ii}\varepsilon_{kk}$$

and

$$\varepsilon_{ij}\varepsilon_{kl}\delta_{il}\delta_{lj} = \varepsilon_{ij}\varepsilon_{ij}\,.$$

Thus we can write the elastic energy as

$$U = \frac{1}{2}\left(\lambda\varepsilon_{ii}\varepsilon_{jj} + 2\mu\varepsilon_{ij}\varepsilon_{ij}\right)\,. \tag{2.18}$$

where λ and μ are called the Lamé coefficients and their value is dependent on the mechanical properties of the material. Comparing 2.17 and 2.18 we can extract the expression of σ_{ij}

as a function of the strain

$$\sigma_{ij} = \lambda \varepsilon_{kk} \delta_{ij} + 2\mu \varepsilon_{ij} \,. \tag{2.19}$$

In Physics, these type of relations that describe the response of a system to an external perturbation are called constitutive relations. In some situations it is useful to invert the relation i.e. write ε_{ij} as a function of σ_{ij} and to do that we have to find a relation between $\mathrm{tr}(\varepsilon)$ and $\mathrm{tr}(\sigma)$. From (2.19) we write the diagonal elements of the stress tensor

$$\sigma_{ii} = \lambda \varepsilon_{kk} + 2\mu \varepsilon_{ii} \quad \not{\sum}_i$$

where $\not{\sum}_i$ means there is no summation in the i index. Summing over i we get

$$\mathrm{tr}(\sigma) = (3\lambda + 2\mu)\,\mathrm{tr}(\varepsilon) \,. \tag{2.20}$$

Plugging in this result into (2.19) and solving for ε_{ij} we arrive at

$$\begin{aligned} \varepsilon_{ij} &= \frac{1}{2\mu}\left(\sigma_{ij} - \frac{\lambda}{3\lambda + 2\mu}\delta_{ij}\sigma_{kk}\right) \\ &= \lambda' \delta_{ij}\sigma_{kk} + 2\mu' \sigma_{ij} \end{aligned} \tag{2.21}$$

where

$$\begin{aligned} \lambda' &= -\frac{\lambda}{2\mu\,(3\lambda + 2\mu)} \\ \mu' &= \frac{1}{4\mu} \end{aligned}$$

are called the Lamé elasticity constants.

2.3.7 Infinite, Isotropic and Homogeneous body under an external force

Suppose we have an infinite, isotropic body where the Lamé coefficients are constant everywhere in the body. An external force field f_i is applied. We want to calculate the displacement field when the system is in mechanical equilibrium. We start with the constitutive relation for an isotropic body (2.19) and put it into equation 2.12 and we are left to solve

$$(\lambda + \mu)\,\partial_{ij} u_j + \mu \partial_{jj} u_i + f_i = 0 \,.$$

If we apply a Fourier Transform to the previous equation we obtain

$$(\lambda + \mu) k_i k_j \hat{u}_j(\mathbf{k}) + \mu |\mathbf{k}|^2 \hat{u}_i(\mathbf{k}) = \hat{f}_i(\mathbf{k}) \,,$$

which we can write as a set of linear equations at each point in wave space, such that

$$G_{ij}(\mathbf{k}) \hat{u}_j(\mathbf{k}) = \hat{f}_i(\mathbf{k}) \tag{2.22}$$

where $G_{ij}(\mathbf{k})$ is called the Green tensor for an infinite, homogeneous and isotropic body, and its components are given by

$$G_{ij}(\mathbf{k}) = \mu\delta_{ij}|\mathbf{k}|^2 + (\lambda+\mu)k_i k_j \,.$$

This equation gives us the applied force as a function of the displacement. Since we want the opposite, we need to invert the equation by calculating $G_{ij}^{-1}(\mathbf{k})$, which is a 3×3 matrix. Using the adjoint method, the inverse Green tensor is given by

$$G_{ij}^{-1}(\mathbf{k}) = \frac{1}{\mu|\mathbf{k}|^2}\left[\delta_{ij} - \frac{k_i k_j}{|\mathbf{k}|^2}\right] \tag{2.23}$$

2.4 Phase Field Models

2.4.1 Description

Solving PDEs in regular grids has been a necessity in many areas of applied mathematics, engineering, physics, among others. However, in many cases, we are faced with the need of solving such equations in systems with very complex geometries and where the boundaries can have complicated shapes that cannot be expressed using elementary mathematical functions. This becomes even harder when the domain's topology can change with time.

As an example, suppose we want to describe the dynamics of a binary mixture containing two immiscible components A and B (Figure 2.1). Solving the governing equations of a system such as this one requires us to keep track of the position of the boundary interface between the domains of the two phases and applying the appropriate boundary conditions at each time step. Phase field models were created to overcome these difficulties and

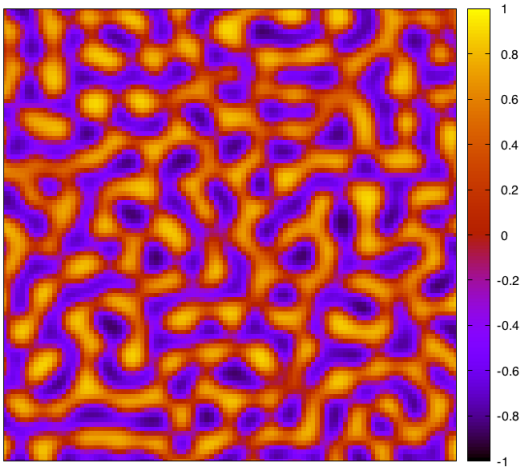

FIGURE 2.1: Example of the use of an order parameter field to describe a binary mixture (Model B).

introduce a way to solve the equations of interest without the need to worry about complex geometries and complicated boundary conditions [41]. The main idea behind a phase field model is to define an auxiliary scalar field, or set of fields, to describe the different phases

of the system. These fields are usually called order parameters and they have very distinct values depending on the phase present at each position in space. Afterwards, we define a free energy functional using those new variables that contains as many terms as necessary to describe the physical processes relevant to the system's accurate description. This will in turn determine the time evolution of the order parameter as well as the creation of an interface of finite width between different phases (Figure 2.2). With the appearance of this diffuse interface, we no longer have the necessity of imposing boundary conditions at the separation layer between different domains and consequently, we do not have to track the interface's position in time. There are different types of phase field models depending

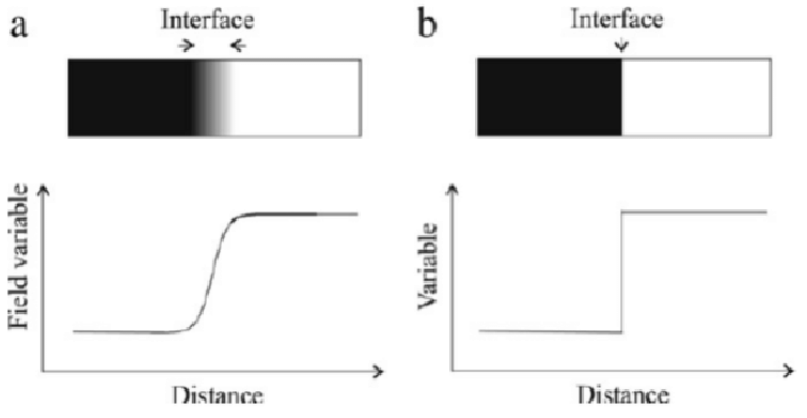

FIGURE 2.2: Difference between a diffuse (a) and sharp (b) interface model and the variation of the order parameter [42].

on the physical aspects of the system we are studying, although the main idea behind them does not differ much from what was described before. Due to their importance in the development of the models described in this work, we will focus on three of the main types of these models.

2.4.2 Model A

The first step when building a phase field model is to write down the free energy that will drive the system's evolution and that contains all of the terms that describe the relevant physical processes in the system. One term that is always present determines the existence of two stables phases (let us assume the system can be fully described using a single order parameter field). This free energy has the following form

$$F\left[\phi(\mathbf{r})\right] = \int \left[f_0(\phi) + \frac{\epsilon^2}{2} \left(\nabla\phi\right)^2 \right] \mathrm{d}\mathbf{r} \tag{2.24}$$

The choice of f_0 is related to the values we choose to label the different phases of the system. In this work we choose this energy so that those values coincide with $\phi \approx +1$ for one phase and $\phi \approx -1$ for the other. In this case, f_0 is given by

$$f_0(\phi) = -\frac{\phi^2}{2} + \frac{\phi^4}{4} \tag{2.25}$$

If we try and find the minima of this function we have to solve

$$\frac{\mathrm{d}f_0}{\mathrm{d}\phi} = 0 \Leftrightarrow -\phi + \phi^3 = 0$$

whose solutions are $\phi = \pm 1$ just like we wanted ($\phi = 0$ is a local maximum of this function).

The second term in the free energy is the one responsible for the creation of a diffuse interface between the phases. The term proportional to the spatial derivatives of ϕ adds an energetic penalty for fast variations of ϕ (which happens at the boundaries), leading to the formation of a smooth interface of finite width on the order of ϵ.

So far, what we have done is valid both for model A and B phase field models. Where they differ is in the choice of dynamical equation for the order parameter. In model A, the time evolution is given by [43]:

$$\frac{\partial \phi}{\partial t} + \boldsymbol{\nabla} \cdot (\phi \mathbf{v}) = -M \frac{\delta F}{\delta \phi} \tag{2.26}$$

where $\mathbf{v}$ is some velocity responsible for advection, M is a motility coefficient and the current is given by the functional derivative of the free energy with respect to changes in the order parameter.

2.4.3 Model B

The difference between Model A and B is that in this case we impose a conservation law to order parameter [44]. We start from a conservation equation

$$\frac{\partial \phi}{\partial t} + \boldsymbol{\nabla} \cdot \mathbf{J} = 0\,, \tag{2.27}$$

which we easily recognize for example, from electrodynamics. Next, we use Fick's law of diffusion to write the current as

$$\mathbf{J} = -M \boldsymbol{\nabla} \frac{\delta F}{\delta \phi}$$

forcing the system to evolve in the way that minimizes the free energy. Plugging $\mathbf{J}$ into the conservation equation we obtain the Cahn–Hilliard equaton (Figure 2.1)

$$\frac{\partial \phi}{\partial t} = \boldsymbol{\nabla} \cdot \left(M \boldsymbol{\nabla} \frac{\delta F}{\delta \phi} \right) . \tag{2.28}$$

Under this evolution law, the quantity

$$\phi_{\mathrm{tot}} = \int_V \phi \, \mathrm{d}\mathbf{r} \ ,$$

where we integrate over the whole system, is constant in time.

Steady state solution in 1D

The one-dimensional Cahn-Hilliard equation with a Ginzburg-Landau free energy functional can be solved analytical to find the shape of the interface in a steady state. Using the free energy functional in 2.24 the equation reads

$$-\phi + \phi^3 - \epsilon^2 \frac{\mathrm{d}^2\phi}{\mathrm{d}x^2} = 0 \tag{2.29}$$

which is a non-linear, second order differential equation. Multiplying the terms by $\frac{\mathrm{d}\phi}{\mathrm{d}x}$ and using the chain rule we get

$$\frac{\mathrm{d}}{\mathrm{d}x}\left[-\frac{\phi^2}{2} + \frac{\phi^4}{4} - \frac{\epsilon^2}{2}\left(\frac{\mathrm{d}\phi}{\mathrm{d}x}\right)^2\right] = 0 \tag{2.30}$$

We can integrate this expression between $x' = -\infty$ and $x' = x$. Considering that, $\frac{\mathrm{d}\phi}{\mathrm{d}x} = 0$ and $\phi = -1$ when $x \to -\infty$, we get

$$2\epsilon^2\left(\frac{\mathrm{d}\phi}{\mathrm{d}x}\right)^2 = -2\phi^2 + \phi^4 + 1 = \left(\phi^2 - 1\right)^2 \tag{2.31}$$

Taking the square root of both sides and keeping the negative branch where $\frac{\mathrm{d}\phi}{\mathrm{d}x} < 0$ as $x \to +\infty$, we are left with

$$\frac{\mathrm{d}\phi}{\mathrm{d}x} = \frac{1}{\sqrt{2}\epsilon}\left(1 - \phi^2\right) \tag{2.32}$$

which is a separable ordinary differential equation. Solving the integral using an hyperbolic substitution method we show that, at the steady state, the shape of the interface is given by

$$\phi(x) = \tanh\left(\frac{x}{\sqrt{2}\epsilon}\right). \tag{2.33}$$

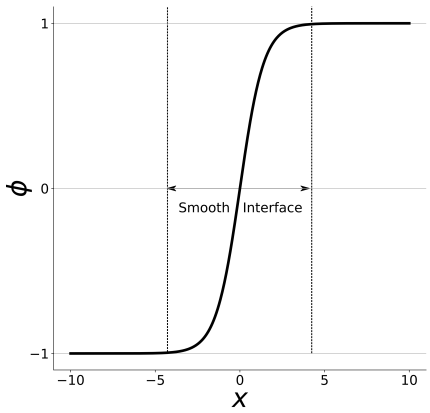

FIGURE 2.3: Graphical representation of the solution to the Cahn-Hilliard equation in one dimension.

2.4.4 Model H

Phase field model H has become popular in the last decade, especially in the modeling of cells and other biological phenomena. This approach combines the dynamics of model B but adds an advection term to the Cahn-Hilliard equation. This velocity is computed using the Navier-Stokes equation where the physical processes of interest are modeled as forces. For a system where inertial terms are ignored and incompressibility is assumed, the set of equations that described a model H system can be given by

$$\begin{aligned}
&\frac{\partial \phi}{\partial t} + \mathbf{v} \cdot \boldsymbol{\nabla} \phi = \nabla^2 \frac{\delta F}{\delta \phi} \\
&\boldsymbol{\nabla} \cdot \mathbf{v} = 0 \\
&\nu \nabla^2 \mathbf{v} - \boldsymbol{\nabla} p + \mathbf{F} = 0 \\
&\mathbf{F} = -\phi \boldsymbol{\nabla} \frac{\delta F}{\delta \phi} \,,
\end{aligned}$$

where ν is the viscosity. The pressure function, p, can be calculated from the incompressibility condition. $\mathbf{F}$ represents the force vector field.

2.5 Rodrigues Formula for 3D Rotations

Let $\mathbf{v}'$ be the result of rotating a vector $\mathbf{v}$ around an axis $\hat{k}$ by an angle θ. We wish to find an operator R such that

$$\mathbf{v}' = R\mathbf{v} \tag{2.34}$$

We can decompose $\mathbf{v}$ as the sum of a vector parallel to the axis of rotation, $\mathbf{v}_p$ and a component perpendicular to $\hat{k}$, $\mathbf{v}_n$ such that

$$\mathbf{v} = \mathbf{v}_p + \mathbf{v}_n \,. \tag{2.35}$$

The component of $\mathbf{v}$ along the axial direction is simply the projection of $\mathbf{v}$ on $\hat{k}$:

$$\mathbf{v}_p = (\hat{k} \cdot \mathbf{v})\hat{k} \,, \tag{2.36}$$

and this component is unchanged during the rotation so that

$$\mathbf{v}'_p = \mathbf{v}_p \,. \tag{2.37}$$

Transforming the normal component is essentially performing a 2D rotation on a plane perpendicular to $\hat{k}$ that contains $\mathbf{v}_n$ and $\mathbf{v}'_n$. This component is given by

$$\mathbf{v}'_n = \cos\theta \ \mathbf{v}_n + \sin\theta \ \hat{k} \times \mathbf{v}_n \,. \tag{2.38}$$

Assemblying the two components of $\mathbf{v}'$ we have

$$\begin{aligned}\mathbf{v}' &= \mathbf{v}'_p + \mathbf{v}'_m \\ &= (\hat{k}\cdot\mathbf{v})\hat{k} + \cos\theta\ \mathbf{v}_n + \sin\theta\ \hat{k}\times\mathbf{v}_n \\ &= (\hat{k}\cdot\mathbf{v})\hat{k} + \cos\theta\ (\mathbf{v}-\mathbf{v}_p) + \sin\theta\ \hat{k}\times(\mathbf{v}-\mathbf{v}_p)\end{aligned} \tag{2.39}$$

Using the definition of $\mathbf{v}_p$ and noting that $\hat{k}\times\mathbf{v}_p = 0$ we arrive at the Rodrigues' formula

$$\mathbf{v}' = \cos\theta\ \mathbf{v} + (1-\cos\theta)(\hat{k}\cdot\mathbf{v})\hat{k} + \sin\theta\ \hat{k}\times\mathbf{v}\,. \tag{2.40}$$

In order to rewrite the Rodrigues's formula in matrix form we need to use the following vector identity

$$\mathbf{a}\times(\mathbf{b}\times\mathbf{c}) = (\mathbf{a}\cdot\mathbf{c})\mathbf{b} - (\mathbf{a}\cdot\mathbf{b})\mathbf{c} \tag{2.41}$$

In the case where $\mathbf{a} = \mathbf{b} = \hat{k}$ and $\mathbf{c} = \mathbf{v}$ we get

$$\hat{k}\times(\hat{k}\times\mathbf{v}) = (\hat{k}\cdot\mathbf{v})\hat{k} - \mathbf{v}\,. \tag{2.42}$$

Substituting this last expression rotation formula we have

$$\begin{aligned}\mathbf{v}' &= \cos\theta\ \mathbf{v} + (1-\cos\theta)[\mathbf{v} + \hat{k}\times(\hat{k}\times\mathbf{v})] + \sin\theta\ \hat{k}\times\mathbf{v} \\ &= \mathbf{v} + (1-\cos\theta)\hat{k}\times(\hat{k}\times\mathbf{v}) + \sin\theta\ \hat{k}\times\mathbf{v}\end{aligned} \tag{2.43}$$

The last step in getting the matrix form of the Rodrigues' formula is representing the cross product between two vectors as a matrix-vector product. The cross product between two vectors $\mathbf{a}$ and $\mathbf{b}$ is given by

$$\begin{aligned}\mathbf{a}\times\mathbf{b} &= (a_2b_3 - a_3b_2)\hat{e}_1 + (a_3b_1 - a_1b_3)\hat{e}_2 + (a_1b_2 - a_2b_1)\hat{e}_3 \\ &= \begin{pmatrix} 0 & -a_3 & a_2 \\ a_3 & 0 & -a_1 \\ -a_2 & a_1 & 0 \end{pmatrix}\begin{pmatrix} b_1 \\ b_2 \\ b_3 \end{pmatrix} \\ &= N(\mathbf{a})\mathbf{b}\end{aligned} \tag{2.44}$$

where $N(\mathbf{a})$ is a skew-symmetric matrix that can be seen as an operator that multiplies (on the left) any column vector $\mathbf{x}$ and the result is $\mathbf{a}\times\mathbf{x}$. Using this operator we arrive at the matrix formulation of Rodrigues' formula

$$\mathbf{v}' = \left[I + \sin\theta\ N(\hat{k}) + (1-\cos\theta)N^2(\hat{k})\right]\mathbf{v} = R\mathbf{v} \tag{2.45}$$

where I is the identity matrix. If there is a need to undo a rotation, the operator R^{-1} can be obtained simply by changing θ to $-\theta$, yielding

$$R^{-1} = I - \sin\theta\ N(\hat{k}) + (1-\cos\theta)N^2(\hat{k})\,. \tag{2.46}$$

Chapter 3

Mathematical Model of Keratin Dynamics inside a Cell

The work described in this section resulted in the paper, "Keratin Dynamics and Spatial Distribution in Wild-Type and K14R125P Mutant Cells—A Computational Model", published in April 2020 by the International Journal of Molecular Sciences [45]. The work stems from a collaboration between the Soft and Biological Matter Group at CFisUC, Portugal and Mirjana Liovic's group Faculty of Medicine of the University of Ljubljana, Slovenia.

3.1 Introduction

The epidermis is the multilayered outer layer of skin, which functions as a protective barrier to all internal tissues and organs. It consists of very tightly packed epithelial cells called keratinocytes.The cytoskeleton of epithelial cells includes keratin intermediate filament (IF) proteins. These are essential to cells since they provide not only mechanical resilience [46–49], but are also involved in many cell and tissue functions, such as cell growth, proliferation, migration and in wound healing [50–60].

Altogether 54 keratin genes have been discovered so far [35]. Apart from the skin, keratins are also abundant in skin appendages such as hair and nails [61, 62]. Epidermal keratins are divided into type I and type II proteins. Their genes are clustered on chromosomes 17 (type I) and 12 (type II). Unlike other IF proteins, a type I keratin always pairs up with a specific type II partner, complexifying, thus forming a keratin heterodimer [63, 64]. The assembly process of heterodimers that lead to the formation of intermediate filaments is very complex and has been analyzed in greater detail for another protein, vimentin, that is present in the IF network of endothelial cells [65]. Nevertheless, the same sequence of events has been observed also for other IF proteins, including keratins: first, the lateral association of rod-like tetrameric complexes of IF heterodimers results in the so-called "unit-length filaments" (ULFs, 60 nm long structures). ULFs then associate longitudinally (end-to-end) to form short filaments, which can subsequently anneal longitudinally to build

longer filaments [66]. The general structure of an IF protein consists of an extremely conserved central alpha-helical domain, interrupted by two non-helical linkers, and the head and tail end domains, which vary in length and are less conserved.

Mutations affecting keratin genes have been linked to a variety of hereditary cell fragility disorders [67]. The most comprehensibly studied is epidermolysis bullosa simplex (EBS), a predominantly autosomal dominant disease linked to either keratin 5 or keratin 14 (K5 and K14) gene mutations [68, 69]. Their consequence is the inability of basal layer keratinocytes to resist physical stresses, which manifests as (often severe) skin blistering and wounding. Extensive experiments on EBS patient-derived cell lines have shown that cells retain some of these phenotypic differences also *in vitro* [70–75]. The most typical difference is the presence of highly dynamic keratin particles and aggregates at the cell's periphery in some keratin mutants [71, 72, 74, 76]. Interestingly, dynamic IF aggregates or even smaller filament fragments have been frequently observed also in normal physiological processes, such as during IF network reorganization [65, 70–72, 77–80]. In this respect p38 MAPK has been found as the major regulator of keratin filament remodeling, as well as keratin aggregate formation and disappearance. It has also been shown that keratin precursors appear at the distal tips of actin stress fibers, then move alongside the stress fibers until they integrate the peripheral keratin filament network [78]. Microtubule-dependent transport and dynamics of IF proteins has also been demonstrated both for vimentin and keratin [79, 80]. The majority of mutations lie within the IF central rod domain, and, in particular, in two highly conserved sequences at the filament ends (i.e., helix initiation and termination peptide motifs), which have been recognized as important for the assembly of IF filaments [81, 82]. The effect of mutations may vary, interfering at the structural level (at any stage of the filament assembly process), in the interaction with associated proteins or influencing protein post-translational modifications [71, 83].

Recently the understanding of keratin assembly kinetics, turnover and intracellular transport [84] has advanced significantly. In particular, several parameters that determine keratin dynamics in keratinocytes have been measured [85, 86], such as the diffusion constant of keratin monomers and the advection velocity of keratin fibers towards the nucleus. Furthermore, mathematical approaches have been used to estimate the spatial dependence and numerical values of association and dissociation rates of keratin monomers [85]. However, none of these studies have addressed keratin dynamics in cells expressing mutant keratin. In this chapter we extend a model of keratin turnover [85] by employing a 2D phase field approach to explore the stationary distribution of keratin in the cell, which mirrors already previously observed conditions in cells *in vitro*. In particular, our mathematical model accounts for the appearance of keratin particles and aggregates at the cell periphery, and may thus be applied also to the case of keratin turnover in mutant keratin expressing cells.

3.2 Experimental Work

Combining immunofluorescence techniques with light microscopy allows experimentalists to observe the intermediate filament network that is a part of a cell cytoskeleton. Enhanced green fluorescent proteins (EGFPs) are normally used to tag proteins due to their ability to exhibit fluorescence when exposed to light of a certain frequency. This allows keratin to be marked and observed under a microscope in order to see how the intermediate filament network is organized in a cell and how its arrangement changes in time or in response to mechanical stress. In Figure 3.1 Panel A we can see, on the left, a picture taken from live imaging of wild-type (WT) keratinocytes' EGFP-labeled keratin network, while on the right we have the corresponding image for a group of cells with the K14R125P mutation, containing an unknown amount of mutant keratin, both in unstressed conditions [74]. On the WT keratinocytes we can clearly see, in the perinuclear region, bundles of fibers that are especially dense, extending to the cell membrane where the density diminishes. Looking at the images taken of the mutant keratinocytes we see a completely different arrangement of intermediate filaments. The amount of fibers surrounding the nucleus is drastically lower and instead we see the appearance of small dot-like structures near the cell membrane. These structures are called granular or particulate forms of keratin and their presence in the cytoskeleton is an hallmark of the K14R125P mutation in keratinocytes, known to be associated with EBS. The results of a quantitative measurement of the

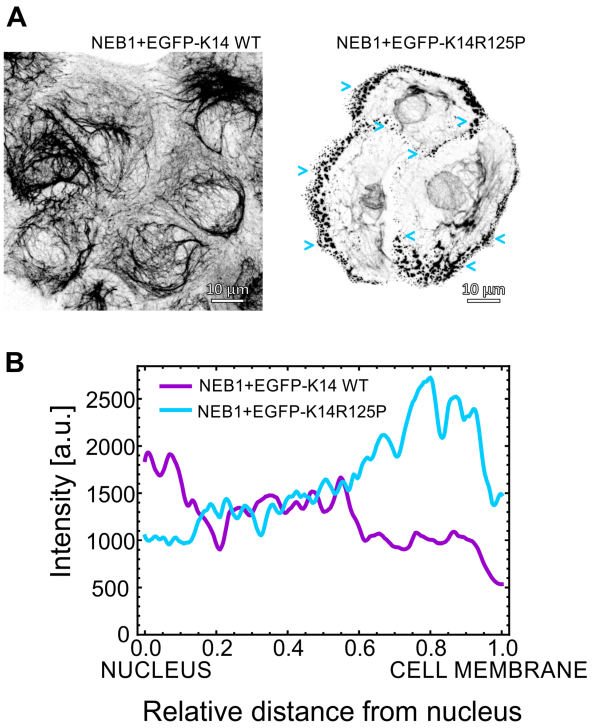

FIGURE 3.1: **Panel A:** Immunofluorescent imaging of the keratin filament network in both wild-type keratinocytes (left) and in K14R125P mutant cells (right). The presence of small granular structures in the periphery of the mutant cells is indicated by blue arrows. **Panel B:** Mean keratin intensity measured in both WT (purple) and mutant cells (blue) as a function of the distance from the nucleus to the cell membrane. Adapted from [45].

concentration of keratin in each cell type as a function of the distance from the nucleus to cell membrane is shown in Figure 3.1 Panel B. The fluorescent signal of EGFP–labeled keratin was measured for multiple cells of each construct (13 WT and 18 mutant cells) and then averaged using image analysis software. For non-mutant cells the intensity profile (purple) shows that the amount of keratin, measured in arbitrary units, is maximum in the perinuclear region, peaking at around 2000 a.u. and decreasing as we get further away from the nucleus, reaching its lowest concentration of around 500 a.u.. The blue curve representing the corresponding profile for mutant cells shows the opposite trend. The maximum in keratin concentration is reached in the peripheral region of the cell at around 2500 a.u. and decreases closer to the nucleus, where it reaches a minimum value of 1000 a.u.

The measurements shown in Panel B confirm the intuitive analysis of images in Panel A, and both clearly show the effect of the K14R125P mutation on the organization of keratinocyte cytoskeleton. In order to understand the effects of the K14R125P mutation on the spatial organization of the keratin network on cells, a mathematical model was developed to shed some light on the mechanisms behind the observed differences to pinpoint at which stage of the keratin assembly/disassembly cycle the effect of the mutation is the most disruptive.

3.3 State of the Art

The number of mathematical models developed to study the keratin cytoskeleton has been small when compared to the effort put into the study of actin filament networks, the organization of micro tubules, or the vimentin cytoskeleton. As such, the mathematical models that have been developed with this topic in mind have resulted from the work of a handful of collaborations between theoretical and experimental researchers.

The first model of keratin dynamics was presented by Portet *et al.* (2003) who described the dynamics of cytokeratin concentration, using a set of partial differential equations combined with a stochastic differential equation approach. The objective was to study how mechanical factors could alter the keratin organization [87]. Other works followed, some consisting of systems of ordinary differential equations, describing the temporal evolution of the concentration of intermediate filament proteins in different states and, solved analytically [88, 89]. Markov Chain models were also used to study intermediate filament assembly, considering the stochastic nature of molecular events [90]. In Portet and Madzvamuse *et al.* (2015) a mathematical model was developed to take into account the spatial and temporal dynamics of the keratin cycle and the spatial dependence of the turnover and transport processes that occur. Different hypotheses for modeling the said processes were tested and parameter estimation was performed. These allowed the authors to suggest values for some of the reaction rates of the keratin cycle by fitting the numerical solution obtained to the profiles of keratin distributions measured experimentally [85].

The motivation of the work presented in this chapter is to build on the existing models of keratin dynamics, particularly on Portet and Madzvamuse et al.(2015), by creating

a mathematical model to describe a cell with an arbitrary shape and its nucleus in two dimensions, and coupled to the PDEs governing the keratin dynamics in time and space, both for wild type and mutant keratin.

In the next section, a description of the mathematical framework used to model a keratinocyte, accounting for possible shape changes it may suffer in time, is given.

3.4 Phase Field Model for the Cell and Nucleus

Before developing a mathematical model for the dynamics of keratin in the cell cytoplasm, we need to first create a model to simulate the cell itself. In this work a phase field model is used to describe the cell and its nucleus, taking advantage of the formation of a smooth interface and thus avoiding the complex task of setting boundary conditions for both the phase field variables themselves as well for the value of concentration of each keratin form used in the model. We define two order parameters $\phi(\mathbf{r})$ and $\psi(\mathbf{r})$ to represent, respectively,

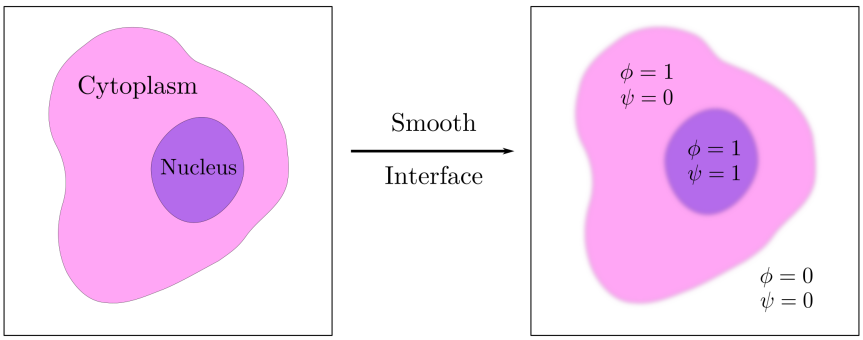

FIGURE 3.2: Diagram of the regions of interest for the model and the corresponding value of each order parameter used in the phase field description. The cell's cytoplasm (in pink) is identified by $\phi \approx 1$ and $\psi \approx 0$ while the nucleus corresponds to $\phi \approx 1$, $\psi \approx 1$ (in purple). The outside of the cell is characterized by values of ϕ and ψ close to zero. The equation chosen for the evolution of the order parameters as a function of the prescribed free energy leads to the formation of a smooth interface.

the interface between the cell and the outside (cell membrane) and the interface between the cell nucleus and the exterior. In Figure 3.2 we can see how to go from a sharp interface model (on the left) of the domain of interest, to a continuous interface approach using the order parameter fields to identify each region of the cell and its exterior.

The free energy functional associated with this description of the system using the phase field formalism is given by

$$F\left[\phi(\mathbf{r}), \psi(\mathbf{r})\right] = F^{\mathrm{pf}}_{\mathrm{cell}} + F^{\mathrm{pf}}_{\mathrm{nuc}} + F^{\mathrm{area}}_{\mathrm{cell}} + F^{\mathrm{area}}_{\mathrm{nuc}} + F^{\mathrm{rep}}\,. \tag{3.1}$$

The two terms in F^{pf} correspond to the free energy associated with the formation of the smooth interface and the appearance of two energetically stable phases, both for $u = \phi$ (cell) and $u = \psi$ (nucleus), given by

$$F^{\mathrm{pf}}\left[u\right] = \int \left[f(u) + \frac{\epsilon^2}{2} |\boldsymbol{\nabla} u|^2 \right] \mathrm{d}V \tag{3.2}$$

where $f(u) = \frac{1}{4}u^2(1-u)^2$ is the double well potential with minima located at $u = 0$ and $u = 1$. The second term serves as an energy penalty that raises the global energy if the system tries to create a rapidly varying interface, such that the formation of a smooth continuous interface is favored.

To ensure that the area of the cell and the nucleus are conserved, we include in the free energy functional the term

$$F^{\text{area}}[u] = \frac{1}{12}\alpha_u \left(V_u^T - V[u]\right)^2 . \tag{3.3}$$

where α_u is a penalization coefficient that controls the weight the soft constraint has during the process of minimization, and V_u^T is the target area set for the field. The functional $V[u]$ is the cell or the nucleus volume

$$V[u] = \int h(u)\,\mathrm{d}V \tag{3.4}$$

where $h(u) = u^2(3-2u)$. In this way, by looking at the functional in 3.3 we see that the overall energy of the system will increase with the deviation (both positive and negative) of the value for the volume from the target value we set (usually the volume measured in the initial conditions).

Finally, F^{rep} is responsible for maintaining the nucleus confined inside the cell. This is done by creating a repulsion force between the nucleus and the outside of the cell. This energy term is given by

$$F^{\text{rep}}[\phi,\psi] = \frac{1}{6}\beta \int h(1-\phi)h(\psi)\,\mathrm{d}V . \tag{3.5}$$

which reaches its maximum value at points where $\phi = 0$ and $\psi = 1$. As the system, follows the energy minimization principle, it will evolve in a way that the nucleus and the extracellular medium do not overlap and the nucleus will remain inside the cell.

The time evolution of both ϕ and ψ are given by two coupled Allen-Cahn equations

$$\begin{aligned} \frac{\partial\phi}{\partial t} &= -\frac{\delta F}{\delta\phi} \\ \frac{\partial\psi}{\partial t} &= -\frac{\delta F}{\delta\psi}\,, \end{aligned} \tag{3.6}$$

where

$$\begin{aligned} \frac{\delta F}{\delta\phi} &= -\epsilon^2\nabla^2\phi - \phi(1-\phi)\left(\phi - \frac{1}{2} + \alpha_\phi(V_\phi^T - V(\phi)) + \beta h(\psi)\right) \\ \frac{\delta F}{\delta\psi} &= -\epsilon^2\nabla^2\psi - \psi(1-\psi)\left(\psi - \frac{1}{2} + \alpha_\psi(V_\psi^T - V(\psi)) + \beta(1-h(\phi))\right) . \end{aligned} \tag{3.7}$$

In the next section, the description of how reaction-diffusion-advection dynamics can be coupled to a phase field model is given.

3.5 Reaction-Diffusion-Advection Equations in Complex Geometries

Suppose that we have a two dimensional-domain $\mathcal{D}$ and let Ω be a subdomain of $\mathcal{D}$ representing the space inside the boundary S_Ω. The scalar field $C(\mathbf{r}, t)$ is defined inside Ω and the total value of C can vary either due to the flux of material across S_Ω or via transformations inside the subdomain. The variation of the total value of C via these two processes can then be expressed as

$$\frac{\mathrm{d}}{\mathrm{d}t}\int_\Omega C(\mathbf{r}, t)\,\mathrm{d}\Omega + \int_{S_\Omega} \mathbf{J}\cdot\mathrm{d}\mathbf{S}_{\mathbf{\Omega}} = \int_\Omega R(C, \mathbf{r})\,\mathrm{d}\Omega\ , \tag{3.8}$$

where $\mathbf{J}$ is a vector describing the flux across the boundary of Ω and R the function describing the appearance or disappearance of material inside the domain. If $R(C, \mathbf{r}) > 0$ the function represents a source while if $R(C, \mathbf{r}) < 0$ it represents a sink.

Suppose we use a phase field model to describe the dynamics of the interface that separates Ω from the rest of the domain $\mathcal{D}$. We define an order parameter $\phi(\mathbf{r}, t)$ that has a value close to 1 inside Ω and 0 otherwise. In this case we can approximate $\mathrm{d}\Omega$ using the order parameter while integrating over the whole domain $\mathcal{D}$

$$\mathrm{d}\Omega \approx \phi(\mathbf{r})\,\mathrm{d}V\ , \tag{3.9}$$

since the regions where $\phi = 0$ do not contribute to the value of the integral. Introducing this approximation into the continuity equation written above (the integral over the surface S_Ω can be transformed into a volume integral using Gauss's Theorem) yields

$$\frac{\mathrm{d}}{\mathrm{d}t}\int_V C(\mathbf{r})\phi(\mathbf{r})\,\mathrm{d}V + \int_V \phi(\mathbf{r})\boldsymbol{\nabla}\cdot\mathbf{J}\,\mathrm{d}V = \int_V R(C, \mathbf{r})\phi(\mathbf{r})\,\mathrm{d}V\ . \tag{3.10}$$

Since the product $\phi(\mathbf{r}, t)C(\mathbf{r}, t)$ is a smooth, continuous function, its time derivative can go inside the integral sign transforming it into a partial derivative, while the second term can be integrated by parts resulting in

$$\int_V \left[\frac{\partial(\phi C)}{\partial t} + \boldsymbol{\nabla}\cdot(\phi\mathbf{J}) - \mathbf{J}\cdot\boldsymbol{\nabla}\phi - R\phi\right]\mathrm{d}V = 0\,.$$

For this condition to be verified, the integrand must be zero everywhere in the domain, i.e.

$$\frac{\partial(\phi C)}{\partial t} + \boldsymbol{\nabla}\cdot(\phi\mathbf{J}) - \mathbf{J}\cdot\boldsymbol{\nabla}\phi - R\phi = 0\,. \tag{3.11}$$

The flux $\mathbf{J}(\mathbf{r})$ can include several terms depending on the physical processes relevant for the model, and the same is true for the function $R(\mathbf{r})$. Supposing that $C(\mathbf{r}, t)$ represents the concentration of some component and that its diffusion follows Fick's Second Law, meaning that the chemical tends to move from places of higher concentration to places of lower concentration, i.e. $\mathbf{J}^{\mathrm{Fick}}(\mathbf{r}) = -D\boldsymbol{\nabla}C$, and that there is an advection field $\mathbf{v}(\mathbf{r})$ dragging the chemical in its flow, we can write the flux as $\mathbf{J}(\mathbf{r}) = -D\boldsymbol{\nabla}C + C\mathbf{v}$ which

turns equation 3.11 into

$$\frac{\partial(\phi C)}{\partial t} = \boldsymbol{\nabla} \cdot (\phi \boldsymbol{\nabla} C) - \boldsymbol{\nabla} \cdot (\phi C \mathbf{v}) + \mathbf{J} \cdot \boldsymbol{\nabla}\phi + R\phi \,. \tag{3.12}$$

Comparing equation 3.11 to an unconstrained diffusion-advection-reaction equation we see that there is an extra term that arises, namely $\mathbf{J} \cdot \boldsymbol{\nabla}\phi$. Using the definition for the current, we see that this term is

$$\begin{aligned} \mathbf{J} \cdot \boldsymbol{\nabla}\phi &= -D\boldsymbol{\nabla}C \cdot \boldsymbol{\nabla}\phi + C\mathbf{v} \cdot \boldsymbol{\nabla}\phi \\ &= (C\mathbf{v} - D\boldsymbol{\nabla}C) \cdot \boldsymbol{\nabla}\phi \,. \end{aligned}$$

A vector that points from the outside of the domain described by ϕ to the inside is given by $\boldsymbol{\nabla}\phi$ and we can define a unit vector that is always perpendicular to the interface at every point as $\hat{n} = \frac{\boldsymbol{\nabla}\phi}{|\boldsymbol{\nabla}\phi|}$. Using these definitions the above equation can be rewritten as

$$\mathbf{J} \cdot \boldsymbol{\nabla}\phi = |\boldsymbol{\nabla}\phi| \, (C\mathbf{v} - D\boldsymbol{\nabla}C) \cdot \hat{n} \,,$$

which imposes a value for the current $\mathbf{J}$ at the interface, such that it can be seen as a von Neumann boundary condition for the flux of C. In the model presented in the following sections we assume zero flux boundary conditions i.e. $\mathbf{J} \cdot \boldsymbol{\nabla}\phi = 0$.

3.5.1 Numerical Methods

The numerical solution of an equation of the form of 3.12, coupled with the phase field equations that govern the evolution of the domain's interface, can be accomplished using different numerical methods like finite-volume or finite-elements methods. In this work we opt for a finite difference approach with specific discretization schemes for the inhomogeneous diffusion and advection terms. For the discretization of the time derivative we use forward differentiation formulas such that

$$\frac{\partial \, (\phi C)}{\partial t} \approx \frac{\phi^{t+1} C^{t+1} - \phi^t C^t}{\Delta t} \,.$$

To write both the diffusion and advection terms in a regular grid, we use a staggered grid approach where the derivatives are calculated at midpoints by interpolating the value of

the relevant functions. Using this scheme, the diffusion and advection terms are written as

$$\begin{aligned}\frac{\partial}{\partial x}\left(\phi\frac{\partial C}{\partial x}\right) &\approx \frac{1}{\Delta x}\left(\phi\frac{\partial C}{\partial x}\right)\Big|_{i+1/2,j} - \frac{1}{\Delta x}\left(\phi\frac{\partial C}{\partial x}\right)\Big|_{i-1/2,j} \\ &\approx \frac{1}{\Delta x}\left[\frac{\phi_{i+1,j}+\phi_{i,j}}{2}\frac{C_{i+1,j}-C_{i,j}}{\Delta x}\right. \\ &\quad \left. -\frac{\phi_{i,j}+\phi_{i-1,j}}{2}\frac{C_{i,j}-C_{i-1,j}}{\Delta x}\right]\end{aligned} \tag{3.13}$$

$$\begin{aligned}\frac{\partial}{\partial x}\left(\phi C v^x\right) &\approx \frac{1}{\Delta x}\left(\phi C v^x\right)\Big|_{i+1/2,j} - \frac{1}{\Delta x}\left(\phi C v^x\right)\Big|_{i-1/2,j} \\ &\approx \frac{1}{\Delta x}\left[\frac{\phi_{i+1,j}+\phi_{i,j}}{2}\frac{C_{i+1,j}+C_{i,j}}{2}\frac{v^x_{i+1,j}+v^x_{i,j}}{2}\right. \\ &\quad \left. -\frac{\phi_{i,j}+\phi_{i-1,j}}{2}\frac{C_{i,j}+C_{i-1,j}}{2}\frac{v^x_{i,j}+v^x_{i-1,j}}{2}\right]\end{aligned}$$

In this derivation only the terms in the x direction are shown, the procedure being the

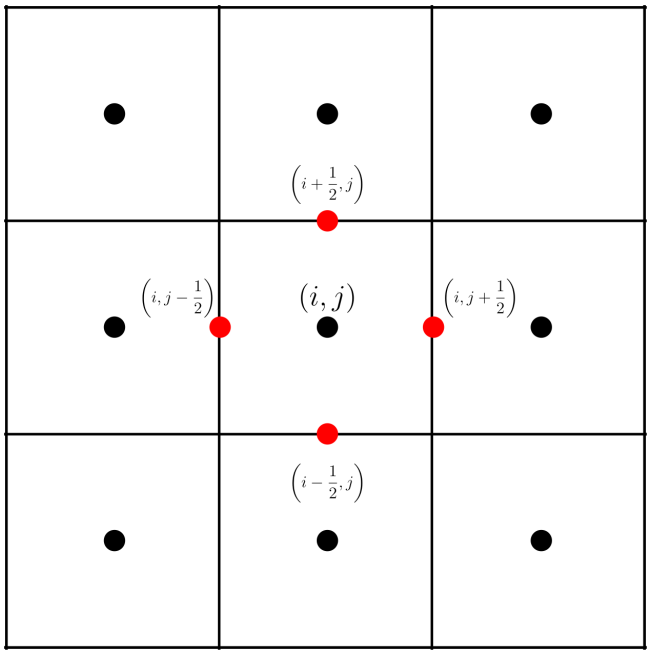

FIGURE 3.3: Example of a grid where the derivatives of a function are calculated using finite differences with the interpolated values at the midpoints (red) based on the values of the function in the center points (black).

same for the y direction, *mutatis mutandis*. Using this discretization scheme, the equation becomes

$$\frac{\phi^{t+1}_{i,j}C^{t+1}_{i,j} - \phi^t_{i,j}C^t_{i,j}}{\Delta t} = [\boldsymbol{\nabla}\cdot(\phi\boldsymbol{\nabla}C)]^t_{i,j} - [\boldsymbol{\nabla}\cdot(\phi\mathbf{v})]^t_{i,j} + R(\phi^t_{i,j}, C^t_{i,j})\phi^t_{i,j}\,.$$

which we want to solve for $C_{i,j}^{t+1}$. Manipulating the equation, we get

$$\begin{aligned} C_{i,j}^{t+1} = \frac{1}{\phi_{i,j}^{t+1}} \Big[& \phi_{i,j}^{t} C_{i,j}^{t} + \Delta t \left[\boldsymbol{\nabla} \cdot (\phi \boldsymbol{\nabla} C) \right]_{i,j}^{t} \\ & - \Delta t \left[\boldsymbol{\nabla} \cdot (\phi \mathbf{v}) \right]_{i,j}^{t} + \Delta t R(\phi_{i,j}^{t}, C_{i,j}^{t}) \phi_{i,j}^{t} \Big] . \end{aligned} \tag{3.14}$$

Simply by looking at equation 3.14 we can foresee a numerical problem when $\phi^{t+1} \approx 0$. To overcome this difficulty we must define a new solution for when the denominator in 3.14 is close to zero. The numerical scheme that fixes this problem is given by

$$C_{i,j}^{t+1} = \begin{cases} C_{i,j}^{t+1} = \dfrac{1}{\phi_{i,j}^{t+1}} \Big[\phi_{i,j}^{t} C_{i,j}^{t} + \Delta t \left[\boldsymbol{\nabla} \cdot (\phi \boldsymbol{\nabla} C) \right]_{i,j}^{t} \\ \qquad - \Delta t \left[\boldsymbol{\nabla} \cdot (\phi \mathbf{v}) \right]_{i,j}^{t} + \Delta t R(\phi_{i,j}^{t}, C_{i,j}^{t}) \phi_{i,j}^{t} \Big] & \text{if } \left| \phi_{i,j}^{t+1} \right| \geq \epsilon_C \\ \phi_{i,j}^{t+1} C_{i,j}^{t} & \text{if } \left| \phi_{i,j}^{t+1} \right| < \epsilon_C \end{cases} \tag{3.15}$$

where ϵ_C is a value that serves as threshold for the minimum value of $\left|\phi^{t+1}\right|$ where the numerical solution presented in 3.14 is considered valid.

3.6 Spatial Distribution of Keratin in Wild-Type and Mutant Cells

The intermediate filament network of a cell is mostly located in the cytoplasm, although the presence of K17 keratin inside the nucleus has been observed [91]. Since the work presented in this chapter is focused on the K14 keratin form, the presence of keratin anywhere outside the cytoplasm is neglected. Based on the description of the model for the cell and nucleus described in Section 4.4, the cytoplasm can be represented by an auxiliary field $\eta(\mathbf{r}, t)$ defined as

$$\eta(\mathbf{r}, t) = \phi(\mathbf{r}, t) \left[1 - \psi(\mathbf{r}, t) \right] \tag{3.16}$$

such that $\eta \approx 1$ in the cytoplasm and $\eta \approx 0$ everywhere else in the computational domain.

A 2D extension of the model described in [85] is used to describe the keratin cycle. In the work of Portet *et al.* (2015), the authors consider that keratin can be found in two states, the soluble keratin pool and the insoluble keratin filaments. Introducing an intermediary keratin phase, we are able to account for the small keratin aggregates observed near the cell membrane of mutant keratinocytes (Figure 3.1 Panel A on the right). These keratin particles are highly dynamic and can both integrate into filaments, as well as disassemble to the soluble keratin pool. The diagram in Figure 3.4 shows the three types of keratin we consider in the model: soluble (S), particulate (P) and filamentous keratin (F). It also shows the different processes by which keratin can change state and the rate at which that change occurs. K_{SP} corresponds to the rate at which soluble keratin can aggregate forming small particles while K_{PS} is associated with the inverse process. The keratin that is found in filaments can disassemble and rejoin the soluble pool at a rate K_{FS}. Finally, the

formation of keratin filaments depends on the passage of keratin from the particulate state to the insoluble phase and the reaction rate K_{PF} sets the timescale for that transformation.

The concentration of soluble keratin inside the cytoplasm is given by $C_S = \eta c_S$ where c_S is an auxiliary field that can be non-zero outside the cytoplasm and has no physical meaning in that region. The concentration of the other two forms is written in a similar manner and the system of coupled PDEs that describes the dynamics of the keratin cycle is the following

$$\begin{aligned}
\frac{\partial(\eta c_S)}{\partial t} &= D_S \boldsymbol{\nabla} \cdot (\eta \boldsymbol{\nabla} c_S) + R_S(c_S, c_P, c_F, \eta)\eta \\
\frac{\partial(\eta c_P)}{\partial t} &= D_P \boldsymbol{\nabla} \cdot (\eta \boldsymbol{\nabla} c_P) - \boldsymbol{\nabla} \cdot (c_P \eta \mathbf{v_a}) + R_P(c_S, c_P, c_F, \eta)\eta \\
,\frac{\partial(\eta c_F)}{\partial t} &= D_F \boldsymbol{\nabla} \cdot (\eta \boldsymbol{\nabla} c_F) - \boldsymbol{\nabla} \cdot (c_F \eta \mathbf{v_a}) + R_F(c_S, c_P, c_F, \eta)\eta
\end{aligned} \tag{3.17}$$

where D_S, D_P and D_I are the diffusion constants of each keratin form, and $\mathbf{v_a}$ is the advection velocity that models the transport of non-soluble keratin towards the nuclear membrane by the actomyosin fibers. R_S, R_P and R_F are functions that model the passage of keratin from one state to another as a function of the concentrations of each species. Since some of these reactions only occur in specific locations of the cell, these functions are also space-dependent. The reaction functions in 3.17 are modeled using results obtained in

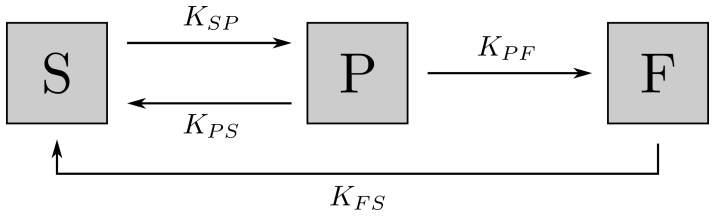

FIGURE 3.4: Proposed model for the assembly and disassembly of keratin and the reaction rates associated with each process. We assume the coexistence of three keratin states: soluble (S), particulate (P) and insoluble/filamentous (F).

[85] and are given by

$$\begin{aligned}
R_S &= K_{FS}\gamma(\mathbf{r})\frac{c_F}{k_F + c_F} + K_{PS}\gamma(\mathbf{r})c_P - K_{SP}\delta(\mathbf{r})\frac{c_S}{k_S + c_S} \\
R_P &= -K_{PS}\gamma(\mathbf{r})c_P + K_{SP}\delta(\mathbf{r})\frac{c_S}{k_S + c_S} - K_{PF}c_P \\
,R_F &= K_{PF}c_P - K_{FS}\gamma(\mathbf{r})\frac{c_F}{k_F + c_F}
\end{aligned} \tag{3.18}$$

where k_S and k_F are constants that characterize the Michaelis-Menten kynetics and correspond to the values of concentration at which the reaction rates reach half its maximum value. $\delta(\mathbf{r})$ and $\gamma(\mathbf{r})$ are space dependent functions that are needed to define in which region each reaction occurs. $\delta(\mathbf{r})$ has a value close to one at the cell cortex i.e. near the cell membrane, and zero everywhere else. Some of the reaction rates show a linear dependence on the distance from the cell membrane, so the function $\gamma(\mathbf{r})$ is defined such that its value is zero near the cell membrane, rising linearly to its maximum value of one in

the perinuclear region. A more detailed explanation of how these functions are calculated will be given in the next section.

Combining equations 3.17 and 3.18 we have the explicit expression for the dynamics of the keratin cycle:

$$\begin{aligned}
\frac{\partial(\eta c_S)}{\partial t} &= D_S \boldsymbol{\nabla}\cdot(\eta\boldsymbol{\nabla}c_S) + \left[K_{FS}\gamma\tfrac{c_F}{k_F+c_F} + K_{PS}\gamma c_P - K_{SP}\delta\tfrac{c_S}{k_S+c_S}\right]\eta \\
\frac{\partial(\eta c_P)}{\partial t} &= D_P \boldsymbol{\nabla}\cdot(\eta\boldsymbol{\nabla}c_P) - \boldsymbol{\nabla}\cdot(c_P\eta\mathbf{v_a}) + \left[K_{SP}\delta\tfrac{c_S}{k_S+c_S} - K_{PS}\gamma c_P - K_{PF}c_P\right]\eta \\
\frac{\partial(\eta c_F)}{\partial t} &= D_F \boldsymbol{\nabla}\cdot(\eta\boldsymbol{\nabla}c_F) - \boldsymbol{\nabla}\cdot(c_F\eta\mathbf{v_a}) + \left[K_{PF}c_P - K_{FS}\gamma\tfrac{c_F}{k_F+c_F}\right]\eta\,.
\end{aligned} \tag{3.19}$$

3.6.1 Localizing Functions $\gamma(\mathbf{r})$ and $\delta(\mathbf{r})$

Quantitative Experimental Studies of Keratin Assembly/Disassembly

As mentioned before, the assembly and disassembly processes that keratin undergoes do not happen homogeneously throughout the cytoplasm. In Moch *et al.* (2013) fluorescent time-lapse imaging of human vulva carcinoma derived cells was used to measure the regulation of the keratin IF cytoskeleton [77]. Using mathematical modeling combined with image analysis techniques, the authors were able to identify the regions of the cell where keratin filament sources and sinks are located. Furthermore, the velocity field that transports keratin towards the nucleus was also mapped. An abridged version of the results obtained in this paper is presented in Figure 3.5. The average velocity of keratin has an almost constant value of 165.0 ± 6.4 nm/min in the cytoplasm that drops drastically to zero as we approach the nuclear membrane, as can be seen in panel A of Figure 3.5. When measured after 54 hours (panel A on the right), the advection velocity drops to 108.0 ± 3.3 nm/min. To estimate the orientation of the velocity, a vector field was calculated (panel B) based on the images in panel A and it is clear that the direction of advection of keratin points towards the periphery of the nucleus, moving inwards from the cell membrane. However, since not all keratin accumulates near the nucleus, there must be keratin sinks causing its disassembly during transport. In panel C, the location of keratin sources and sinks was determined. Keratin assembly is seen to happen exclusively in a thin ring around the cell membrane while the turnover process is seen in the region between the assembly zone and the nuclear envelope.

Based on these results, the need to introduce a spatial dependence on the reaction rates that regulate keratin assembly and disassembly is obvious as well as the demand for a correct modeling of the keratin advection field $\mathbf{v_a}$.

Mathematical Modeling

The definition of $\gamma(\mathbf{r})$ and $\delta(\mathbf{r})$ is dependent on measuring the distance of a certain point belonging to the cytoplasm to the nuclear membrane. The diffuse interface resulting from using the phase field method to model the cell and nucleus interface, makes it hard to calculate this distance since the points that belong to the interface are not rigorously

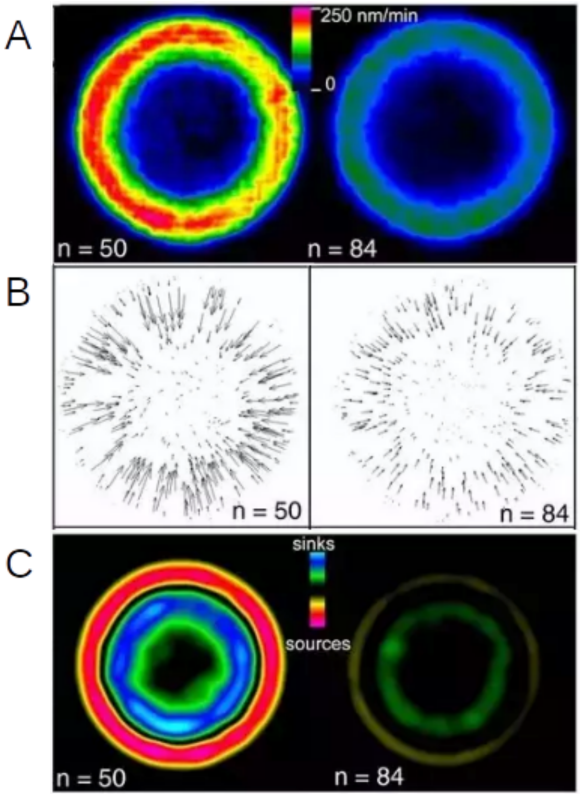

FIGURE 3.5: The images are a result of statistical image analysis performed on n cells where the average cell shape has been mapped to a circular shape to aid the analysis. The left column corresponds to images taken after 27 hours into the keratin cycle and on the right are the same images after another 27 hours. **Panel A**: Keratin speed heatmap. **Panel B**: Keratin advection velocity field obtained from the heatmaps in Panel A. **Panel C:** Qualitative assessment of the amount of keratin that is assembled in sources (pink zones) and disassembled in sinks (blue zones). Adapted from Moch et al (2013) [77].

defined. We can, however, approximate that distance by solving an ancillary problem. Suppose we have a system with circular symmetry and we want to solve the Laplace equation in an ring bounded by radius R_1 and R_2

$$\nabla^2 D = 0$$

that obeys the Dirichlet boundary conditions $D(R_1) = 1$ and $D(R_2) = 0$. The solution to the Laplace equation in this case is given by

$$D(r) = C_1 \log(r) + C_2 \,. \tag{3.20}$$

Expanding the solution around $r = R_1$, keeping only first order terms and applying the boundary conditions on the approximate solution, we have

$$D(r) = 1 - \frac{r - R_1}{R_2 - R_1} \tag{3.21}$$

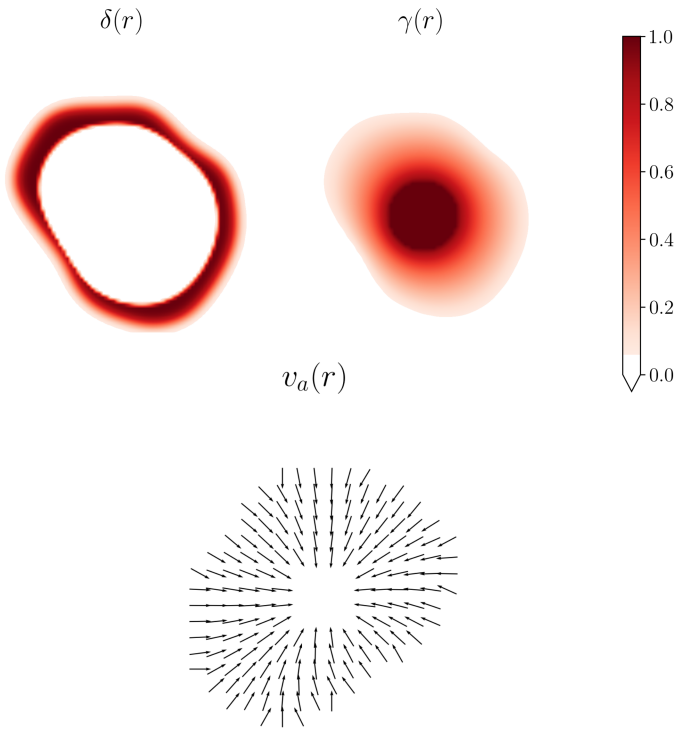

FIGURE 3.6: In the top panel, we see density plots that show how the functions $\gamma(\mathbf{r})$ and $\delta(\mathbf{r})$ vary in space. In the bottom panel, we see the direction of the advection field calculated from the $\gamma(\mathbf{r})$ function.

which is a linear function. Computationally, in order to estimate the distance of a certain point in the cytoplasm to the nucleus, we solve the equation

$$\frac{\partial D}{\partial \tau} = \nabla^2 D$$

with the following boundary conditions defined using the order parameters ϕ and ψ: $D(\psi = 1) = 1$ and $D(\phi = 0) = 0$.

The solution $D(\mathbf{r})$ will act as our distance function from where we can define the localizing function $\delta(\mathbf{r})$ as

$$\delta(\mathbf{r}) = \begin{cases} 0\,, D(\mathbf{r}) > D_{\text{int}} \\ 1\,, D(\mathbf{r}) \leq D_{\text{int}} \end{cases} \tag{3.22}$$

which defines the cell cortex where keratin assembly happens. For $\gamma(\mathbf{r})$ what we want is a function that increases quasi-linearly with the distance to the cell membrane, so we simply have that

$$\gamma(\mathbf{r}) = D(\mathbf{r})\,. \tag{3.23}$$

Finally, we use $D(\mathbf{r})$ to define the direction of keratin transport by the actin fibers. At each point, the velocity is given by

$$\mathbf{v_a} = v_a^{\max} \frac{\boldsymbol{\nabla} D}{|\boldsymbol{\nabla} D|} \tag{3.24}$$

and the result can be seen in Figure 3.6.

3.6.2 Initial Conditions

Before solving the system of PDEs that simulates the cell shape and the keratin distribution, we need to choose the initial conditions. For the cell we choose a non-symmetric, complex shape that tries to mimic the shape of a real keratinocyte. To do that, a cell was drawn using the vector graphics free software Inkscape, making use of the Bézier Curves tool. After that the image was converted to a binary matrix so it could be used in the software written to numerically solve the model's equations. Due to the stability shown by the shape of the nucleus in this particular unstressed system, it is modeled as a simple circle.

Since we are interested in finding the steady state distribution of keratin inside the cell in a stress-free environment, we solve the Allen-Cahn equations for the cell and nuclear membranes first and only afterwards we solve the reaction-advection-diffusion system for the keratin. In practice, this means that the phase field and the keratin equations are uncoupled, since during the temporal evolution of the keratin profile $\phi(\mathbf{r})$ and $\psi(\mathbf{r})$ are static fields. Solving equations 3.6 we obtain the fields represented in Figure 3.7.

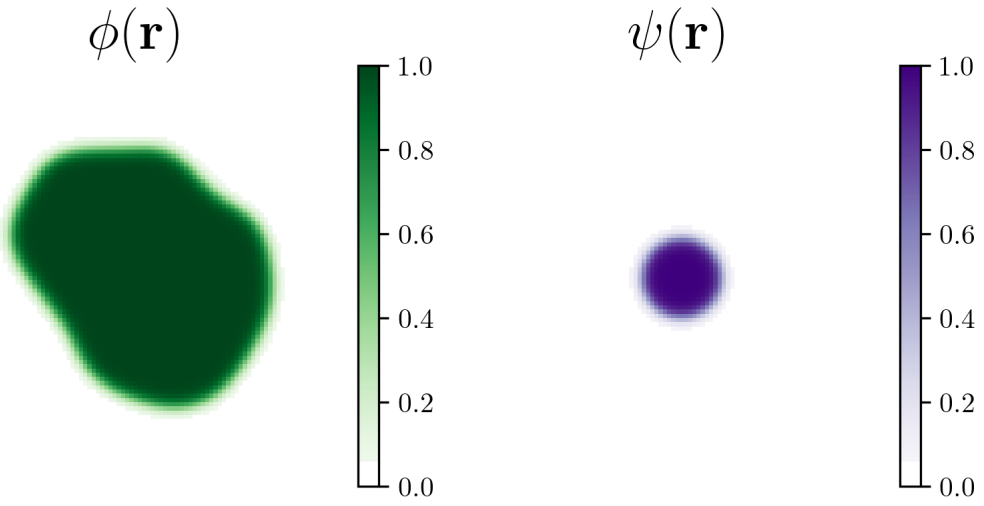

FIGURE 3.7: $\phi(\mathbf{r})$ (left) and $\psi(\mathbf{r})$ (right) obtained from the two Allen-Cahn equations in 3.6.

TABLE 3.1: Initial value of each keratin form concentration at every point inside the cytoplasm.

Keratin Form	Value	Source
C_F	700 μM	[85]
C_S	$\frac{0.05}{0.95}C_F$	[85]
C_P	C_F	–

Besides the solutions to the phase field equations, we need to define the initial conditions for the keratin distribution in the cytoplasm. In this case we use the same conditions as in [85] for the soluble and filamentous keratin (Table 3.1). Since there is no information regarding the amount of keratin in particulate form in the literature, we assume that the initial

distribution of C_P is the same as the one for C_F. The concentration presented in Table 3.1 for each keratin form is the value of the concentration at every point in the cytoplasm i.e. the keratin is initially uniformly distributed. The fact that keratin is uniformly distributed in the beginning of the simulation does not affect the steady state distribution, however it has an effect on the number of integration steps needed for the solution to converge to the steady state.

3.6.3 Parameterization

The value of the model parameters used in the simulations are presented in Table 3.2. For the study of the effects of the R125P mutation in the equations for keratin dynamics, the only parameter that does not have a fixed value is the K_{PF} reaction rate. In subsequent sections, other parameters' value will be varied in order to show how their changes modify the solution but only in order to validate modeling choices. The value of parameters in

TABLE 3.2: Values used for the model parameters in the simulation. All parameters except the domain size, Δx, Δy, D_{int} and K_{PS} were taken from [85]. The value for the cell radius is approximate since the cell does not have a circular shape.

Parameter	Value
Box Size	200×200
$\Delta x = \Delta y$	0.66 μm
Cell Radius	22.5 μm
Nucleus Radius	7.5 μm
D_{int}	0.15
D_S	0.88 μm^2 s^{-1}
$D_F = D_P$	$0.01 D_S$
$\lvert\mathbf{v_a}\rvert$	2.5 nm s^{-1}
K_{SP}	9.8 μM s^{-1}
k_S	570 μM
K_{FS}	0.99 μM s^{-1}
k_F	970 μM
K_{PS}	$0.01 K_{FS}$

Table 3.2 are presented with their respective units, even though in the simulation all the parameters are defined relative to the values of Δx and Δy. This serves only to simplify the formulas used in the finite difference discretization.

3.7 Results and Discussion

3.7.1 Wild Type and Mutant Keratin Distributions

Solving the equations of the keratin dynamics until a steady state is reached means following the temporal evolution of the concentrations at every point until

$$\frac{\partial C_S}{\partial t} = \frac{\partial C_P}{\partial t} = \frac{\partial C_F}{\partial t} = 0\,.$$

Computationally, a criterion must be set to evaluate if the steady state has been reached. In the results shown in this section, the criterion chosen was the difference between the maximum value of each concentration from one timestep to the next being below a certain threshold, i.e. $\max(|C^{t+1} - C^t|) < \epsilon$.

In Figure 3.8 the results for the steady state distribution of all keratin forms are presented, both for the wild type and mutant cells. The parameters used in the simulations are the same as presented in Table 3.2. In the simulations for the wild type cells, the value was set to be $K_{PF}^{\mathrm{WT}} = 0.1\ \mathrm{s}^{-1}$ while for the mutant keratin the same rate is 1000× smaller, $K_{PF}^{\mathrm{M}} = 10^{-4}\ \mathrm{s}^{-1}$. The biggest difference between the two cases can be seen when looking at the result for the insoluble keratin distribution, defined as the sum of the particulate and filamentous keratin. In the wild type case, the accumulation of insoluble keratin happens in the periphery of the nucleus and the maximum value reached is $\approx 2700\ \mu$M. On the other hand, in mutant cells, the non-soluble keratin is mainly located in the cell cortex, near the membrane and its concentration peaks at $\approx 2500\ \mu$M.

Despite the biggest differences being seen in the distribution of the non-soluble keratin, the distribution and amount of each keratin form also differs when comparing the WT cells and the cells with the R125P mutation. The soluble keratin in non-mutant cells is, like the insoluble keratin, more concentrated around the nuclear envelope. This accumulation results from the disassembly of filamentous keratin back to the soluble pool and since there is barely any granular keratin, there is less soluble keratin around the cell membrane. In the mutant case, not only do we have a great amount of keratin on the cell cortex, but we also have some filaments around the nucleus. This is due to the active transport of granules towards the nucleus and the linear dependence of the disassembly rate on the distance from the interface, which creates a more uniform distribution soluble pool throughout the cytoplasm. In both cases, granular keratin accumulates near the interface of the cell, but in mutant cells, the maximum value for its concentration is 200× greater than in wild type cells. Finally, keratin in filament form accumulates near the nucleus in WT cells, as expected, while in mutant cells there is still filament formation but they are not located in a well defined region. In the latter case they can be found in the mid region between the nucleus and the cell interface and they result from the small amount of aggregate keratin that is transported by actin fibers and is able to convert to filaments. Parallel to this process, filament disassembly happens faster than filament formation meaning they will be disassembled before reaching the perinuclear region.

3.7.2 Influence of K_{PF} on Insoluble Keratin Profiles

To understand further the dependence of insoluble keratin distribution on the filament assembly rate K_{PF}, in Figure 3.9 we plot the radial profile of this distribution for different values of the parameter. In the top panel of the figure we see three curves that show the radial average of the concentration of insoluble keratin as a function of the distance to the nuclear membrane, for three different values of the filament assembly rate K_{PF}. The green curve corresponds to $K_{PF} = 10^{-2}\ \mathrm{s}^{-1}$, meaning we are in the WT case. This fact is

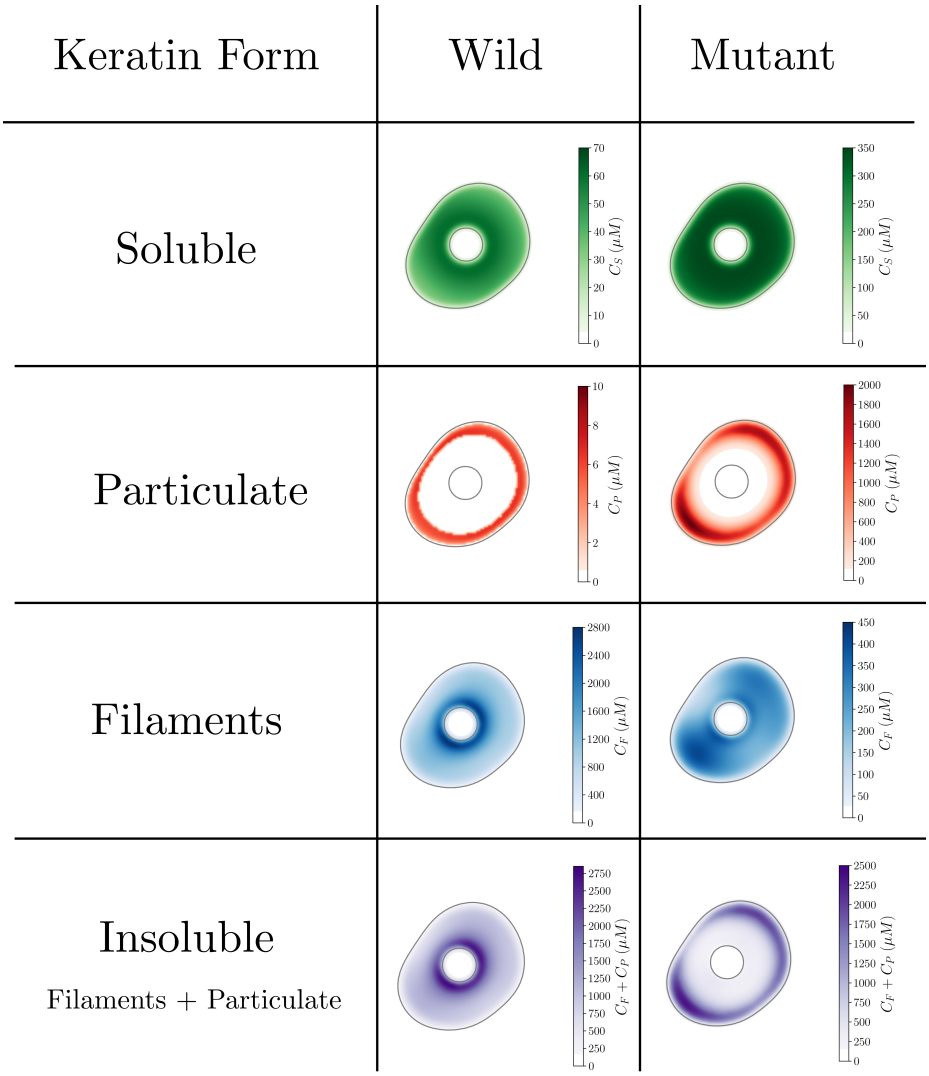

FIGURE 3.8: Steady state distributions of the concentration for different keratin forms. On the left column we have the results for a cell containing WT keratin and, on the right, the same distributions for a mutant cell. It shows, separately, the soluble keratin pool (first row), granular keratin (second), keratin filaments (third row) and insoluble keratin i.e. granular keratin plus the filaments (fourth row).

confirmed by the accumulation of insoluble keratin near the nucleus and the fast decline in concentration as we get closer to the cell membrane. In purple, for $K_{PF} = 10^{-3}$ s^{-1}, we observe an alteration in the profile since, although there is a considerable accumulation of keratin near the nucleus, the concentration does not decay as fast as in the previous case, and we see the formation of a concentration plateau where the amount of insoluble keratin is constant before going to zero near the membrane, as expected. By decreasing the value of K_{PF} by another order of magnitude we can see the profile more common in cells with mutant keratin. In this case, the blue curve shows there is very little keratin at the periphery of the nucleus and instead the non-soluble keratin accumulates in a region close to the cell membrane.

Besides the spatial distribution of keratin in wild-type and mutant cells, we have measured the relative amounts of each keratin form in the steady state for different values of K_{PF} (Figure 3.9 bottom). While for $K_{PF} = 10^{-2}$ or 10^{-3} s^{-1} the filament state of keratin

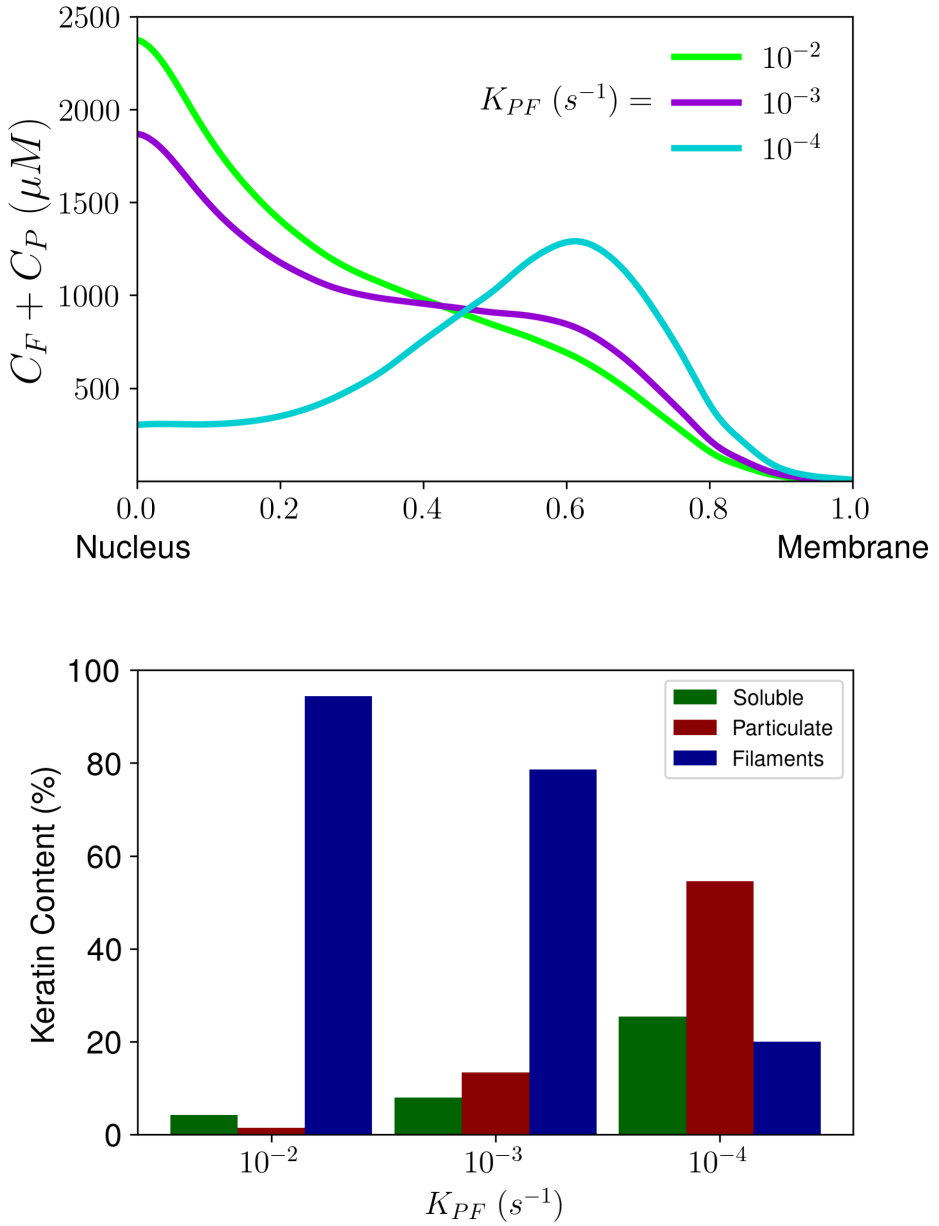

FIGURE 3.9: Radial average profiles of insoluble keratin concentrations (top) and the percentage of the total amount of keratin in the cell that corresponds to each keratin form (bottom), for different values of K_{PF}.

clearly dominates the composition of the intermediate filaments in the cytoskeleton, at 95% and 80% respectively, for the lowest value of the reaction rate there is an inversion and the particulate keratin reaches around 50%. Even in this case, a small amount of filaments can still be observed in the network which is compatible with what is seen in the experiments. This observation will be further explored in the next chapter.

3.7.3 Regarding Modeling Choices

The results presented in the previous section show that the mathematical model developed for this biological system can replicate the effects of the K14R125P mutation on the

distribution of keratin in the cytoskeleton. There are, however, some options made when developing the model that, for the sake of robustness, should be tested.

Different Values for D_P and D_F

In the numerical experiments performed to determine the steady state distribution of keratin in both WT and mutant cells, the value for the diffusion coefficients of the non-soluble keratin forms was taken to be $D_P = D_F = 10^{-2} D_S$. These values were taken from literature [85] although their value was not accurately determined. As such, the same simulation of the keratin cycle was performed for different values of that same parameter. The results obtained for the WT and mutant keratinocytes are presented in Figure 3.10. A great part of the dynamics of insoluble keratin in this model can be interpreted as an

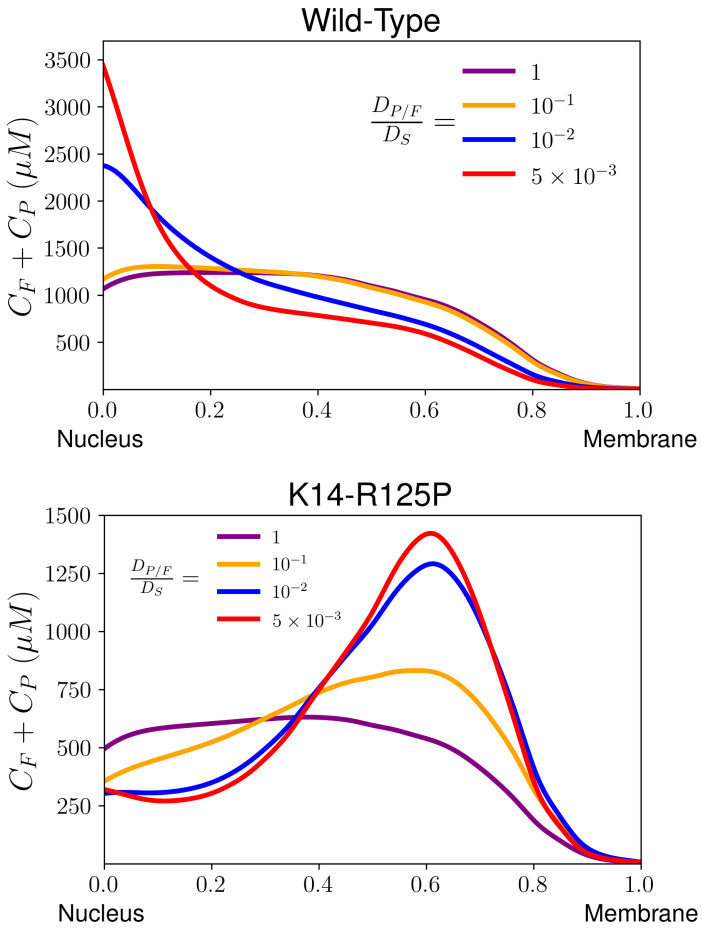

FIGURE 3.10: Radial average profiles of insoluble keratin concentrations for different values of D_P and D_F for both wild type (upper panel) and mutant cells (bottom panel).

interplay between the diffusion of keratin forms and their active transport by the actin cytoskeleton and myosin motors. In fluid dynamics, the ratio between the timescale of diffusive processes and the timescale of advection or transport phenomena is given by the Peclet number

$$Pe = \frac{L^2/D}{L/u} \tag{3.25}$$

where D is the diffusion rate, u is the advection velocity and L is the characteristic length of the system. For this system, let us assume the characteristic length is the average cell radius such that the lines presented in the graphs in Figure 3.10 correspond to Peclet numbers of: 0.10 (purple), 1.2 (orange), 13 (blue) and 25 (red). When $Pe \ll 1$, diffusive processes dominate the dynamics of the system while for $Pe \gg 1$ advection is the primary driver of the system. In Figure 3.10, we see that for Peclet numbers below one, the radial profile of the insoluble keratin distribution does not match what is seen in experiments, since the distributions are almost uniform throughout the cytoplasm. Only for high Peclet numbers (red and blue) lines does the insoluble keratin accumulate near the nuclear or cell membrane, depending on whether we are simulating WT or mutant cells. These results suggest that the choice made for the diffusion constant of the insoluble keratin, considering that the keratin advection velocity measured is correct, reproduces the transport-dominated dynamics of these keratin forms.

Space Independent Keratin Disassembly

In [85], it is shown that the disassembly of insoluble keratin back to the soluble pool follows the Michaelis-Menten kinetic law and that the disassembly rate increases linearly as we go from the cell membrane to the nucleus. To test how relevant the spatial dependency of the disassembly reaction is, we compare the results shown in Figure 3.9 to the result of simulations where we ignore the dependency of the reaction rate on the distance to the cell membrane and assume $\gamma(\mathbf{r}) = 0.5$ everywhere in the cytoplasm. In Figure 3.11 we

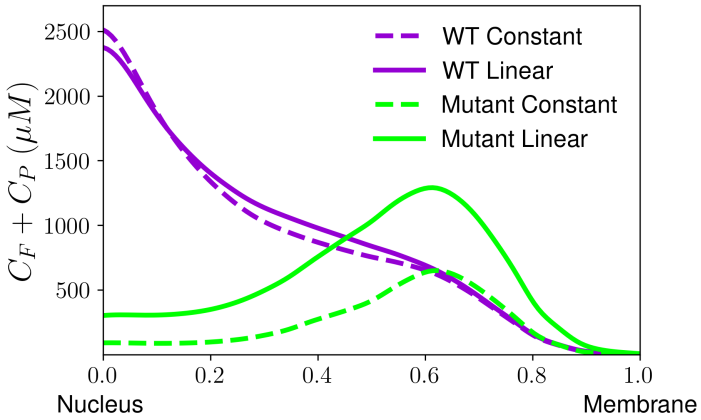

FIGURE 3.11: Radial profiles of insoluble keratin concentration for both WT (purple) and mutant cells (green), when using a uniform disassembly rate (dashed line) or linear dependence on the distance to the nucleus (filled lines).

can see how the concentration profile of insoluble keratin changes when we use a constant disassembly rate as opposed to the linear function of the distance to the cell membrane. For the wild-type case we see there is barely any difference in the profile in the two cases. However, in the mutant cell, we see there is a decrease in accumulated keratin in the cell cortex region. This can be explained by the fact that, in the WT case, where keratin accumulates in the perinuclear zone, the value of the disassembly rate in the constant case is lower than in the original model ($\gamma \approx 1$ in the linear case and $\gamma = 0.5$ in the constant

scenario). For the mutant cells, the exact opposite happens, and we see a decrease in accumulated keratin since particulate keratin stays in the cell cortex where, in the linear case the disassembly rate is very small. When we use a constant disassembly rate, there is more keratin degradation than in the original model and the concentration of particulate keratin is reduced.

Despite the differences of keratin concentrations in these two cases, qualitatively, the results do not suffer a significant change since we still have accumulation of insoluble keratin near the nucleus in the WT case and near the cell membrane in mutant cells.

Alternative Reaction Scheme

More complex models could have been constructed, more specifically by distinguishing different types of particles, or different types of keratin filaments. A reasonable first step in complexifying the model would be to divide the population of keratin particles in two types: the particles that can merge into fibers (P_1) and the particles that cannot (P_2). Therefore, distinguishing these two pools of keratin particles, the simulated pathway would be the one described in Figure 3.12. Since there is no permanent increase of the

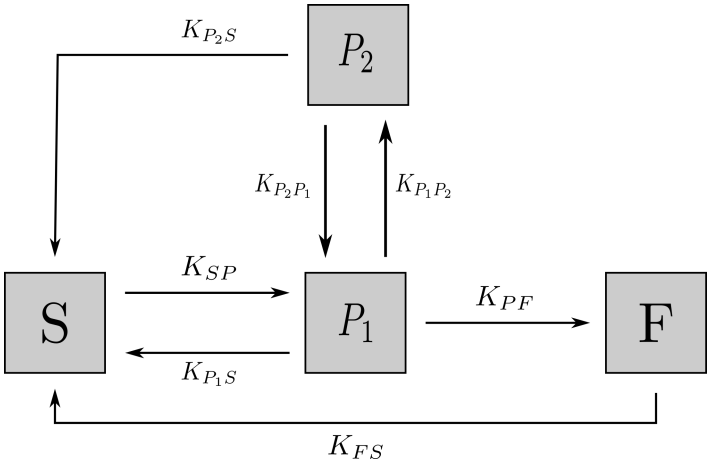

FIGURE 3.12: Alternative reaction diagram when considering two different states of particulate keratin.

concentration of keratin particles and since the particles can clearly disassemble back into the soluble phase as they move towards the cell nucleus, in Figure 3.12 we need to include reactions transforming both keratin particle types into soluble keratin. Importantly, this system would have three more reactions than the one in Figure 3.4 and five more reactions than the model introduced in [85]. In this more complex system, a reasonable choice to regulate the cell mutation would be to increase the reaction rate from keratin particles P_1 to keratin particles P_2 (by increasing $K_{P_1P_2}$, for example). This increase would lead to the accumulation of keratins in the form P_2. In the model of Figure 3.4 we consider just one keratin particle phase with a concentration of particles that corresponds to the sum of all types of keratin particles. Therefore, this concentration would be the sum of the concentrations of the two pools of keratin of the more complex model, i.e., $C_P = C_{P_1} + C_{P_2}$. In this complex model, the particles can disassemble by two processes with rates $K_{P1S}C_{P_1}$

and $K_{P_2S}C_{P_2}$. Therefore, if $K_{P_1S} \approx K_{P_2S} = K_{PS}$, the total rate of particle disassembly rate would be

$$K_{P_1S}C_{P_1} + K_{P_2S}C_{P_2} = K_{PS}(C_{P_1} + C_{P_2}) = K_{PS}C_P$$

i.e., equal to the disassembly rate for the model in Figure 3.4, and independent of the mutation.

Regarding keratin filament assembly, in the more complex model, the keratin particles can assemble into filaments by a single process with rate $K_{PF}C_{P_1}$. Note that in the manuscript we model filament assembly by the rate $K_{PF}C_P = K_{PF}(C_{P_1} + C_{P_2})$. For the complex model, in the wild-type case, C_{P_2} would be approximately zero (low $K_{P_1P_2}$), and both filament assembly rates (the one from the Figure 3.4 model and the one from the complex model) are equal. Strikingly, in the mutated cells, C_{P_2} would become much higher than C_{P_1} and so the simulated model is able to recover the same order of magnitude for the reaction rate obtained in the complex model by decreasing K_{PF}, which is exactly how we model the mutation.

In conclusion, while the model simulated in this work does not distinguish different types of the keratin particles (for which we would require more complex models, as the one exemplified above), it is able to recover the same keratin particle distribution in the mutated cells, since it can reproduce the reaction rates of more complex models between the keratin particles and the other keratin phases.

3.8 Conclusions and Future Work

In this chapter, a mathematical model for the dynamics of the keratin intermediate filament network was presented. The phase field formalism, used to describe the cell and its nucleus as a way to solve partial differential equations in systems with a complex geometry, has proven to be a valuable tool, mainly due to the way possible difficulties with boundary conditions are circumvented by using a smooth interface. Also, the phase field model for the interfaces allows for the solution of equations in cells that are moving or whose shape is changing, even though in this work only static domains were used.

With the system of equations used for the dynamics of keratin in both wild-type and K14R125P mutant cells, we were able to reproduce the spatial distribution of keratin filaments and aggregates that is observed in experiments. Moreover, the hypotheses made about how the mutation affects the assembly of keratin filaments from the intermediate particulate state may help to provide insights about disorders associated with the R125P mutation's phenotype such as EBS. We showed that in WT cells, the fast conversion of particulate keratin into filaments leads to the formation of a fibrous network across the cytoplasm, with a denser concentration of fibers near the cell nucleus. In contrast, when that assembly process is slowed down, there is an accumulation of particulate keratin in the cell cortex and a disrupted keratin network. As shown in [92] these organizational changes in the cytoskeleton lead to different mechanical properties of keratinocytes, emphasized

by the slight increase in cortical stiffness measured in cells with the K14R125P mutation. These differences in mechanical properties can explain the observed difference in response to stress shown by mutant keratinocytes and that are once again linked to the skin fragility shown in EBS patients.

Although the keratin-14 isoform was the focus of this study, other forms of keratin with different structural and biochemical properties are present in the cytoskeleton and could allow us to study the keratin cycle in the context of other physiological and pathological phenomena.

The active transport of insoluble keratin by the actin fibers was shown to be the most important process leading to the steady state distributions observed both for wild type and mutant cells. In this model, this process is included by adding a velocity field that directs insoluble keratin towards the nucleus, which is a simplified account of the dynamic interactions that happen between the actin and the intermediate filament network. A more complex model, including the actin assembly and disassembly cycle coupled to the keratin cycle as modeled in this work, would allow us to study the importance of the active transport in a more detailed manner. Moreover, this combined study of actin and keratin could provide further insight on how keratin mutations can alter the cell mechanical properties since actin filament network is the primary responsible in assuring the cell integrity.

Lastly, solving the equations for the keratin cycle in non-static cells would allow us to study how the keratin cytoskeleton rearranges when keratinocytes are perturbed [92]. This, however, would require the refinement of the numerical methods used to solve the model equations, since explicit finite differences in both time and space would not be able to account for the different timescales at which the keratin cycle and the deformation process happen both *in vivo* and *in vitro*.

Chapter 4

Keratin Aggregate Formation in Mutant Keratinocytes

The work described in this section resulted in the paper "A mathematical model for the dependence of keratin aggregate formation on the quantity of mutant keratin expressed in EGFP-K14R125P keratinocytes", published in December 2021 by PLoS ONE [93]. The work stems from a collaboration between the Soft and Biological Group at CFisUC, Portugal and Mirjana Liovic's group at the Faculty of Medicine of the University of Ljubljana, Slovenia

4.1 Motivation

In the previous chapter we have shown that the K14R125P mutation severely affects the intermediate filament network of epithelial cells. The appearance of small aggregates of keratin in the cell cortex and the disruption of the keratin fiber network leads to an alteration on the cell's ability to endure mechanical, osmotic and even heat-induced stress. EBS is a disorder that is intimately linked to the K14R125P mutation and is characterized by blistering of the skin and inefficient wound healing.

Surprisingly, further studies on the effects of mutated keratin on the IF network have shown that, under certain conditions, cells with mutant keratin are able to form functional filament networks, depending on the degree mutant keratin is combined with WT keratin-5 monomers [66]. The authors of the study further speculate that the appearance of keratin aggregates must have an origin other than the disruption of the filament network. However, to date, no mechanistic explanation has been proposed that could explain the counter-intuitive results (described below) presented in [66].

In the work presented in this chapter, we continue to explore the mechanisms behind keratin aggregate formation, by observing the cytoskeletal arrangement of cultured cells with a mixed content of WT and mutant keratin expressed at different ratios. This study also aims at advancing the understanding of EBS, since the actual ratio of WT to mutant keratin in patient derived cells is still unknown, as it is the effect that different mutant/WT

keratin ratios can have on the patient's disease severity. To this effect, cell clones were engineered such that they express, as close as possible to, 25%, 50% and 100% mutant keratin.

Coupled with the experimental work, we adopted a systems biology approach to model the amount of keratin found in different states for both mutant and WT keratin. Although other mathematical models of keratin dynamics have been developed (see Section 4.3 of Chapter IV) none has considered the coexistence of mutant and WT keratin in the same cell.

4.2 Experimental Results

Using cell engineering techniques, the experimental team was able to control the amount of mutant keratin a cell expresses. In the work presented in the previous chapter, the ratio between WT and mutant keratin expressed by the cells was not know. Using this technique, they wished to obtain three cell lines, each with a different mutant keratin expression value: 25%, 50% and 100%. After culture, the amount of EGFP-K14R125P keratin was measured and the values obtained for each line were: 18%, 45% and 99%. Although the measured keratin amounts were not exactly the ones desired, in this work we will refer to each cell line by their initially intended percentages.

The objective of engineering these cell lines containing both WT and mutated keratin, was to quantify how the amount of mutant keratin in each cell correlates to the amount of keratin found in aggregates. In Figure 4.1A, we can see the results for the number of aggregates found for each cell line. It is clear that the cell line where the fraction of cells with keratin aggregates was maximum was for the 25% construct. This result is surprising, especially when we look at the cell line with 100% mutant keratin and see that it was the one of the three showing the minimum value for the fraction of cells where aggregates were present. However, these results are in accordance with what has been previously seen [66], where it was shown that cells with 100% mutant keratin content could still form filament networks. In Figures 4.1B,C and D, we can see images of cells from each culture: 100% (B), 50% (C) and 25% (D). The red arrows in each frame points to regions where keratin aggregates can be easily seen.

After these images were taken, each culture was subject to centrifugation. This process produces two distinct phase: the supernatant phase, where the lighter components of the cells are found, and the pellet, where the heavier components form a deposit. Afterwards, these two phases were analyzed using a Western Blot, and the amount of WT and mutant keratin present in each phase was measured. In Figure 4.1E we can see the result of the Western Blot with appropriate annotation indicating what is being measured in each well. By knowing the chemical and physical properties of keratin aggregates, we expect that, after centrifugation, all the keratin aggregates will be found in the pellet phase. This allows us to infer what type of keratin (mutated or WT) can be found in the aggregates. The most important result we can extract from Figure 4.1E is that for the 25% mutant

A

Cell line	EGFP K14 R125P 100 %	EGFP K14 R125P 50 %	EGFP K14 R125P 25 %
No. of cells w/out aggregates	353	207	288
No. of cells with aggregates	3	25	65
Total no. of cells	356	232	353
% of cells with aggregates	0.8	10.8	18.4

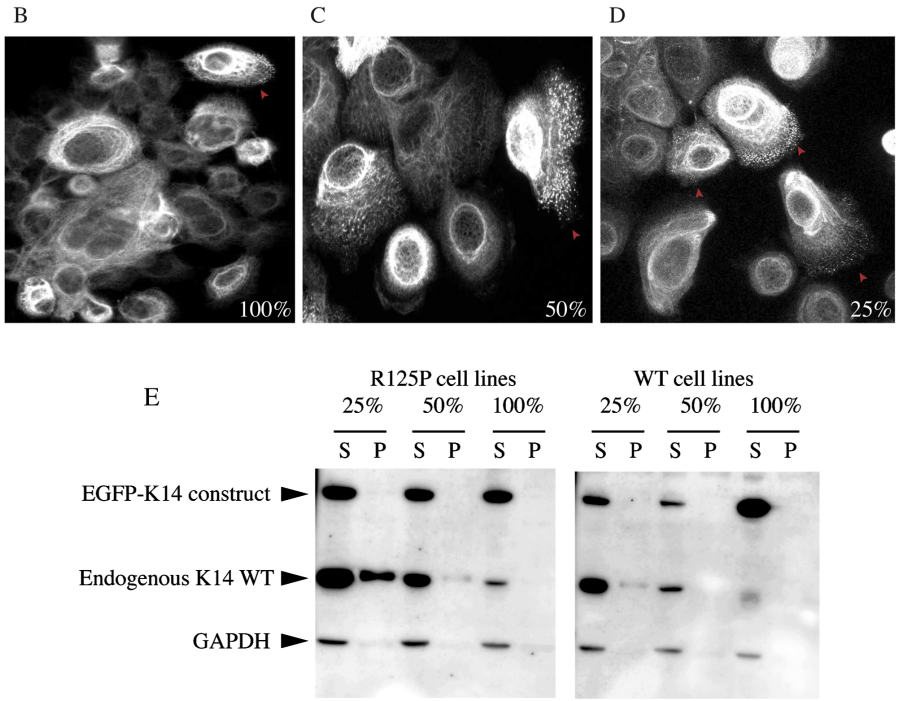

FIGURE 4.1: Table summarizing the results of aggregated keratin quantification for each construct (A). Images of keratinocytes with labeled keratin from each cell line (100% (B), 50% (C) and 100% (D)). The red arrows point to areas where keratin aggregates are visible. Results from a Western Blot, quantifying the amount of keratin present in the supernatant (S) and pellet (P) after centrifugation. GAPDH was used as internal loading control.

keratin construct, where the maximum number of keratin aggregates was measured, there is a significantly higher content of WT keratin compared to the amount of mutant keratin present in the pellet. For the 50 and 100% constructs, the amount of both mutant and WT keratin present in the pellet is almost negligible when compared to what is seen in the 25% case.

The significant difference in WT keratin fraction found in the pellet, when compared to the amount of mutant keratin that was measured, suggests that the formation of keratin aggregates involves binding of both WT and mutant keratin at a ratio that is not 1:1. As will be shown in a further section, a model where a 1:1 ratio is considered for the formation of keratin aggregates is not able to replicate the experimental observations presented in this section. Thus, in the model presented in the next section we introduce the concept of asymmetric binding between WT and mutant keratin at a $\gamma : 1$ ratio as a requisite for the formation of keratin aggregates.

4.3 Model Description

4.3.1 Proposed Reaction Network

In light of what was found in the experimental work presented in the previous section, we propose a new reaction network (Figure 4.2) that demonstrates how the coexistence of WT and mutant keratin affects the intermediate filament network. Keratins can be found in

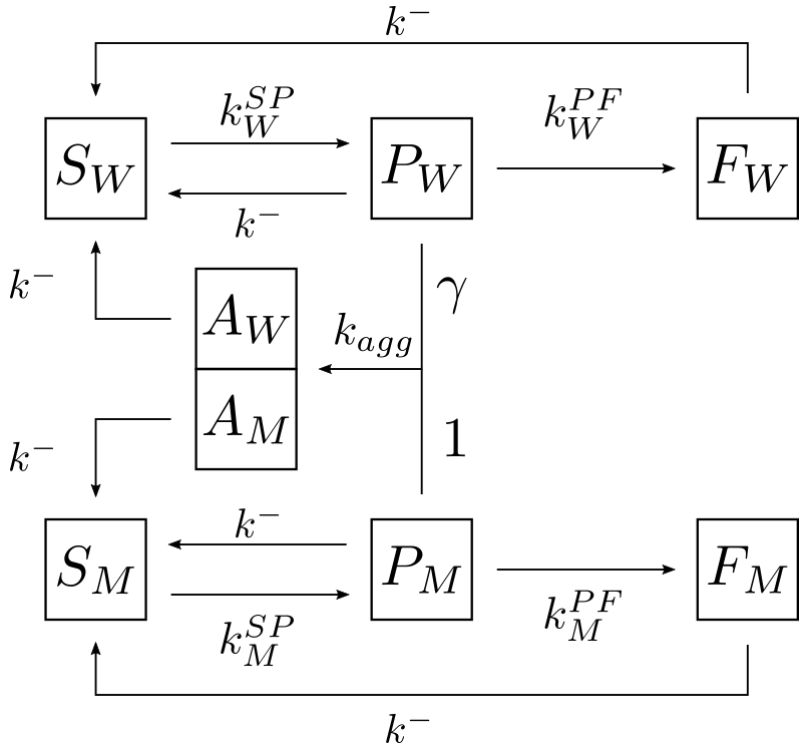

FIGURE 4.2: Diagram representing the proposed reaction network for the coupled dynamics of mutant and WT keratin in a cell.

complex polymeric structures of different sizes. For the keratin polymerization dynamics to be mathematically treatable, and analogously to other keratin models, we group the keratin configurations in few different states depending if it forms very small oligomers (soluble keratin), intermediate size oligomers (particulate keratin) or filaments. In the reaction network presented here, we consider 8 different states: 4 for each keratin species (WT and mutant). In the equations describing the reaction dynamics, S_W and S_M will represent the concentration of keratin in the soluble phase (W for wild type and M for mutant), P_W and P_M are the concentrations of keratin in the particulate phase, F_W and F_M the respective concentration in the filamentous phase, and A_W and A_M the respective amount of WT and mutant keratin that is present in the aggregates. We consider that all depolymerization processes occur at the same rate k^-. This assumption is valid if we consider that all the assembled keratin forms are deconstructed one unit at a time. $k_{W/M}^{SP}$ is the rate at which WT or mutant keratin found in the soluble state forms particles, while $k_{W/M}^{PF}$ is the rate at which these same particles assemble to form filaments. We propose that when two particles of different types, one WT and one mutant, assemble with reaction rate k_{agg}, they will integrate a keratin aggregate. We use the parameter γ to reflect the asymmetric formation

of aggregates from WT and mutant particles, which does not necessarily occur in a 1:1 ratio. A possible asymmetric mechanism of aggregate formation is by binding WT and mutant particles of different typical sizes. These aggregates are not static and they can lose keratin back to the soluble phase.

4.3.2 Mathematical Model

The reaction network presented in Figure 4.2 is modeled mathematically by the following system of ordinary differential equations (ODEs):

$$\begin{aligned}
\frac{\mathrm{d}S_W}{\mathrm{d}t} &= -k_W^{SP} S_W + k^- \left(P_W + F_W + A_W\right) \\
\frac{\mathrm{d}S_M}{\mathrm{d}t} &= -k_M^{SP} S_M + k^- \left(P_M + F_M + A_M\right) \\
\frac{\mathrm{d}P_W}{\mathrm{d}t} &= k_W^{SP} S_W - k^- P_W - k_W^{PF} P_W - \gamma k_{\mathrm{agg}} P_W P_M \\
\frac{\mathrm{d}P_M}{\mathrm{d}t} &= k_M^{SP} S_M - k^- P_M - k_M^{PF} P_M - k_{\mathrm{agg}} P_W P_M \\
\frac{\mathrm{d}F_W}{\mathrm{d}t} &= k_W^{PF} P_W - k^- F_W \\
\frac{\mathrm{d}F_M}{\mathrm{d}t} &= k_M^{PF} P_M - k^- F_M \\
\frac{\mathrm{d}A_W}{\mathrm{d}t} &= \gamma k_{\mathrm{agg}} P_W P_M - k^- A_W \\
\frac{\mathrm{d}A_M}{\mathrm{d}t} &= k_{\mathrm{agg}} P_W P_M - k^- A_M
\end{aligned} \tag{4.1}$$

These equations describe the temporal evolution of the concentrations of the different keratin phases. We assume all reactions can be modeled using first-order kinetics except for the formation of aggregates which depends on the product $P_W P_M$. Since we are only interested in the values of the concentrations when the keratin cycle reaches a dynamical equilibrium, we solve the system of equations until the value of all concentrations are stationary.

To simplify the analysis of the equations, we rewrite the ODEs in a non-dimensional form. We redefine the time variable as $\tau = k^- t$ and replace the concentrations by their respective fractions (indicated in lowercase) of the total amount of keratin in the cell cytoplasm, K_{total}, which is assumed constant. Thus, we are left with the following reformulated system

of equations:

$$\begin{aligned}
\frac{\mathrm{d}s_W}{\mathrm{d}t} &= -\lambda_W^{SP} s_W + p_W + f_W + a_W \\
\frac{\mathrm{d}s_M}{\mathrm{d}t} &= -\lambda_M^{SP} s_M + p_M + f_M + a_M \\
\frac{\mathrm{d}p_W}{\mathrm{d}t} &= \lambda_W^{SP} s_W - p_W - \lambda_W^{PF} p_W - \gamma\lambda_{\mathrm{agg}} p_W p_M \\
\frac{\mathrm{d}p_M}{\mathrm{d}t} &= \lambda_M^{SP} s_M - p_M - \lambda_M^{PF} p_M - \lambda_{\mathrm{agg}} p_W p_M \\
\frac{\mathrm{d}f_W}{\mathrm{d}t} &= \lambda_W^{PF} p_W - f_W \\
\frac{\mathrm{d}f_M}{\mathrm{d}t} &= \lambda_M^{PF} p_M - f_M \\
\frac{\mathrm{d}a_W}{\mathrm{d}t} &= \gamma\lambda_{\mathrm{agg}} p_W p_M - a_W \\
\frac{\mathrm{d}a_M}{\mathrm{d}t} &= \lambda_{\mathrm{agg}} p_W p_M - a_M \,.
\end{aligned} \tag{4.2}$$

In these ODEs, the non-dimensional form of the reaction rates are denoted by λ_W^{SP}, λ_M^{SP}, λ_W^{PF}, λ_M^{PF}, λ_{agg}, with $\lambda_{W/M}^{SP/PF} = k_{W/M}^{SP/PF}/k^-$ and $\lambda_{\mathrm{agg}} = k_{\mathrm{agg}} K_{\mathrm{total}}/k^-$, where K_{total} is the concentration of all keratin types (WT and mutant) in the cell. Here, we set $K_{\mathrm{total}} = 1$ mM [85]. The total fraction of mutant keratin in the cell will be denoted by $\chi_M = s_M + p_M + a_M + f_M$.

4.3.3 Parameter Value

Since the aim of this work is studying the formation of keratin aggregates for cells with different amounts of mutant and WT keratin, the parameters that will be varied in the studies presented in the next section will be χ_M, λ_{agg} and γ. The reaction rates of the other processes will be kept constant during the simulations and their value will be chosen based on data found in the literature.

Table 4.1: Model parameters and their values, both adimensional and in SI units.

Parameter	Adimensional	Value (s^{-1})	Reference
k_W^{SP}	$\lambda_W^{SP} = 1$	1×10^{-3}	[85]
k_M^{SP}	$\lambda_M^{SP} = 1$	1×10^{-3}	[45]
k_W^{PF}	$\lambda_W^{PF} = 100$	1×10^{-1}	[85]
k_M^{PF}	$\lambda_M^{PF} = 0.5$	5×10^{-4}	[45]
k^-	1	1×10^{-3}	[85]

In Table 4.1 the values chosen for the model parameters that stay constant are presented in both their adimensional (used in simulations) and dimensional forms (in SI units).

The value for some of the parameters was taken from the model presented in the previous chapter of this work and in [45]. Since, in that study, the value of the assembly/depolimerization rates was space dependent and in this model we deal only with the temporal evolution of the concentrations, the parameters used had to be averaged in space. Thus, for example, the value of k_W^{SP} in this model is calculated from $k_W^{SP}(x, y)$, a parameter from the previous model, via

$$k_W^{SP} = \frac{1}{\int \eta(x,y)\,\mathrm{d}x\,\mathrm{d}y} \int \eta(x,y) k_W^{SP}(x,y)\,\mathrm{d}x\,\mathrm{d}y \tag{4.3}$$

where $\eta(x, y)$ is the order parameter whose value is ≈ 1 inside the cytoplasm and ≈ 0 everywhere else in the grid, as defined in the previous chapter.

4.3.4 Numerical Methods

To solve computationally the system (4.2) of ODEs, an appropriate method was chosen. Traditionally, when presented with a system of ordinary differential equations subject to a set of initial conditions, an high order, explicit time step algorithm is used, the most popular one being the Runge-Kutta 4th order method. For this problem specifically, however, this method would only guarantee an accurate solution for a very small time step. In fact, the system of ODEs presented in 4.2, combined with the parameter values presented in Table 4.1 is classified as a stiff problem. Different rigorous definitions for what makes a problem stiff have been presented by different experts in the field of numerical analysis [94, 95]. A simplified definition of a stiff system of equations is a system where the parameters of the model span several orders of magnitude. Another way of interpreting this definition is that the system does not have a single characteristic time scale, but multiple. The fastest of these characteristic time scales limits the value for the explicit timestep that guarantees the integration of the system, imposing a very high computational cost of the explicit algorithm.

For the purpose of solving stiff problems, numerical methods have been developed, that circumvent the problems described above. The method used in this work was implemented in the library ODEPACK [96], in a routine called LSODA. This method combines the explicit Adams-Bashforth second-order multistep method with the implicit Backwards Differentiation Formula method along with an adaptative time stepping algorithm. Since the use of an implicit method implies the numerical solution of a system of non linear equations, LSODA uses the iterative Newton-Raphson algorithm to approximate the solution, being necessary to define the Jacobian matrix of the system of equations. In the case of the system in 4.2, the Jacobian is an 8×8 matrix that is explicitly defined in the code.

Although the first implementation of the LSODA algorithm is in FORTRAN77, the routines have been wrapped in more modern languages. In this work, the simulations were ran using the implementation of LSODA in the Python programming language.

To obtain the concentration of each keratin form in the steady state, the system 4.2 were solved for a sufficiently long time interval, until the time derivative of each keratin form fraction was smaller than $\epsilon = 10^{-10}$.

4.4 Results and Discussion

4.4.1 Keratin Aggregates as a function of γ and λ_{agg}

For a certain set of parameters $(\gamma, \lambda_{\text{agg}})$ we can solve the system of ODEs in equation 4.2 provided we define the initial conditions for the concentration of each keratin form. Assuming that, initially, all keratin (WT and mutant) is found in the soluble state, we define χ_M as the total fraction of mutant keratin in the cell such that the initial condition is be given by $s_W(\tau = 0) = 1 - \chi_M$ and $s_M(\tau = 0) = \chi_M$, while the concentration in all other states is set to zero.

Finding the steady state will give us the amount of each keratin form in equilibrium from where we can calculate Q, a quantity defined as

$$Q = \frac{p_W + p_M + a_W + a_M}{f_W + f_M} \tag{4.4}$$

which measures the ratio between particular/aggregate keratin and the fraction of keratin found in filament form.

When the cell has no mutant keratin i.e. when $\chi_M = 0$, it follows that $Q = p_W/f_W \approx 0$, meaning there is barely any aggregate formation. In the opposite case, when $\chi_M = 1$, the amount of aggregates is also close to zero. In fact, observing that, for the set of parameters used (Table 4.1), the system allows the formation of keratin filaments, in these conditions, we also have $Q = p_M/f_M \approx 0$. Q will peak when the fraction of keratin in the aggregate form is larger, for intermediate values of χ_M. By repeating this process for different values of χ_M, while setting constant the value of $(\gamma, \lambda_{\text{agg}})$, plot Q as a function of χ_M. A typical plot is represented in Figure 4.3A. From this curve we can extract two important parameters: $Q^{\max}$ measuring the maximum value keratin found in aggregate form and $\chi_M^{\max}$ the mutant keratin fraction for which $Q = Q^{\max}$.

Since the values of γ and λ_{nuc} have not been measured experimentally, we solve the model equations for different values of both parameters and we draw phase diagrams showing the different values obtained for both $\chi_M^{\max}$ and $Q^{\max}$, as presented in Figure 4.3B and Figure 4.3C, respectively.

For low λ_{agg}, the maximum in the observed aggregate fraction is obtained when the mutant keratin is above 50% of the total keratin in the cell, independently of the value of γ. When the process of aggregate formation is slow, the amount of aggregates in the steady state will directly depend on the size of the pools of particulate WT and mutant keratins in the cell. And so, since the formation of mutant filaments is a slower process than the formation of WT filaments, the fraction of mutant keratin in the particulate phase is higher than

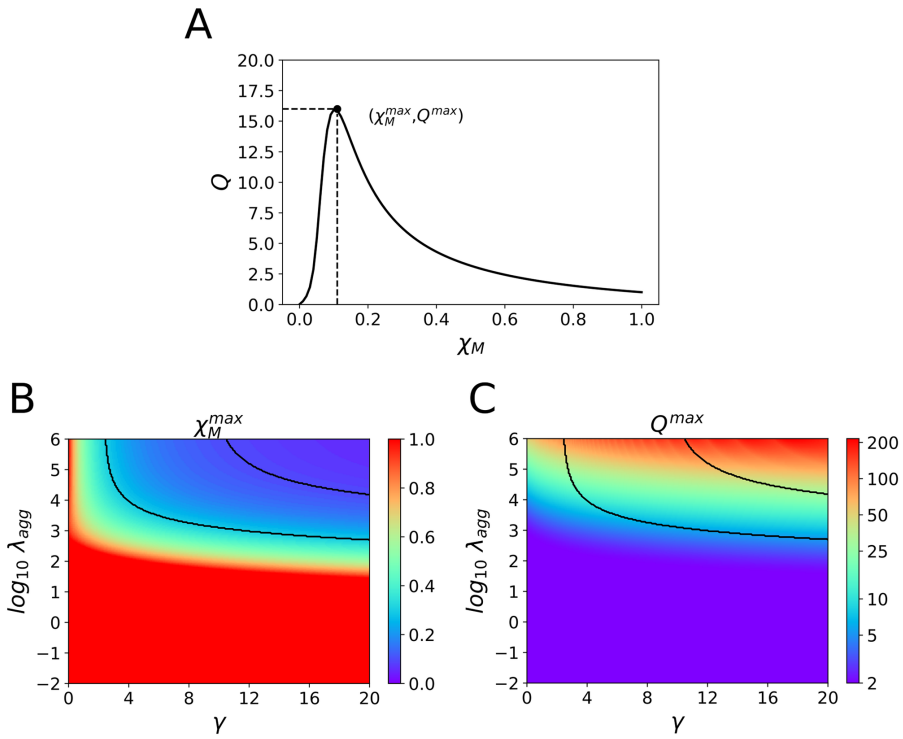

FIGURE 4.3: Example of a curve $Q(\chi_M)$ and of how the values of $\chi_M^{\max}$ and $Q^{\max}$ are determined (A). $\chi_M^{\max}$ (B) and $Q^{\max}$ (C) as a function of γ and λ_{agg}. The black lines in (A) and (B) delimit the region of parameter space where the maximum value of keratin aggregates occurs for percentages of mutant keratin between 15 and 30%.

the fraction of WT keratin in the particulate phase. Therefore, the most effective way to increase the fraction of keratin in the particulate phase in the cell is to increase the fraction of mutant keratin. Consequently, aggregate formation will peak at keratin mutant fraction above 50%. On the other hand, if the reaction rate of aggregate formation is high, we obtain the maximum in the observed aggregate fraction for mutant keratin below 50% of the total keratin in the cell, if $\gamma \gtrapprox 3$. At high λ_{agg}, aggregate formation is faster than filament formation. Therefore, if γ is large, adding WT keratin is a very efficient way to increase the amount of aggregates in the cell, since it readily reacts with mutant keratin in a ratio of γ to 1. However, we observe that if $\gamma \lessapprox 1$, $\chi_M^{\max}$ is always above 50%.

The experimental results of Figure 4.1 discussed in Section 5.2 show that the maximum value of keratin aggregates is measured for the around 25% WT/mutant keratin ratio EGFP-K14R125P cells. We identify in Figure 4.3B the range of parameters where $\chi_M^{\max}$ lays between 15 and 30%. We observe that for values of λ_{agg} in the order of $\approx 10^3 - 10^4$ (corresponding to k_{agg} on the order of $10^3 - 10^4$ $\text{M}^{-1}\text{s}^{-1}$) and for $\gamma > 8$ (including the order of magnitude of the ratio between WT and mutant prevalence in the pellet observed in Figure 4.1), the maximum of aggregates is always obtained for a ratio of mutant keratin close to the one that leads to the maximum number of aggregates in cell experiments. For smaller values of γ between 3 and 8, we still observe that a higher value of $\lambda_{\text{agg}} \approx 10^4 - 10^6$ (corresponding to corresponding to k_{agg} on the order of $10^4 - 10^6$ $\text{M}^{-1}\text{s}^{-1}$) leads to a peak in aggregate formation for $15 - 30\%$ ratio of mutant keratin.

In Figure 4.3C we plot the value of the maximum observable aggregate function, $Q^{\max}$, as a function of γ and λ_{agg}. Expectably, we obtain a larger accumulation of aggregates for larger λ_{agg}. Strikingly, we observe that in the region of parameters on the vicinity of 15-30% (bordered by the black lines in Figure 4.3C), and for $\gamma > 10$, the value $Q^{\max}$ is in the $\approx 10 - 50$ range, depending on the value of λ_{agg}. This means that if we look at the keratin distribution inside a 25% EGFP-K14R125P cell, the model predicts there will be about one order of magnitude more keratin in aggregates than in filaments.

4.4.2 Aggregates vs Particles

In the model, we monitor the observed accumulation of granular keratin forms (particles and aggregates) by calculating the ratio between these forms and keratin filaments,

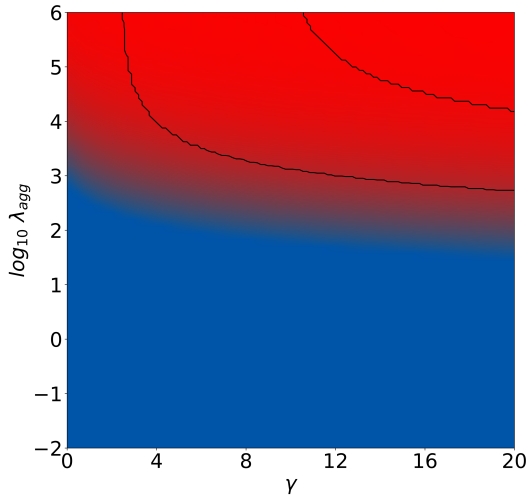

FIGURE 4.4: Keratin forms at the WT-mutant keratin composition that maximises Q. Fraction of aggregates is represented in red, keratin particles in blue and keratin filaments in green. The black lines in the figure delimit the region of parameter space where the maximum value of keratin aggregates occurs for percentages of mutant keratin between 15 and 30%.

$$Q = \frac{a_W + a_M + p_W + p_M}{f_W + f_M}$$

in the stationary state. In Figure 4.3A we observed that a relatively small fraction of mutant is able to lead to the accumulation of these forms. In Figure 4.4 we explore the fraction these different keratin forms at the composition that maximizes Q. Namely, for the mutation fraction $\chi_M^{\max}$ (which depends on the values of λ_{agg} and γ), we calculate the fraction of keratin in the particle ($p_W + p_M$), aggregate ($a_W + a_M$) and filaments ($f_W + f_M$) forms. A color in RGB is assigned to each corresponding point in Figure 4.4, such that the red represents the fraction of aggregates, blue represents the fraction of keratin particles and green the fraction of keratin filaments (normalized by the sum of all non-soluble forms, $a_w + a_M + p_W + p_M + f_W + f_M$). In the graph in Figure 4.4 we can clearly see the existence of two distinct regions with a third much smaller region dividing them. In the red region, defined by $\lambda_{\text{agg}} \gtrapprox 10^3$, almost all the keratin in the cell, in the state that maximizes Q, is found in aggregate form. The blue region, when $\lambda_{\text{agg}} \lessapprox 10^2$, the most dominant keratin

form in the maximizing state is in the form of particles. In the transition between these two dominant regions, we can see a thin predominantly green region where, for the state that maximizes Q, we have a high concentration of keratin filaments. From the graph we see that the region where $Q^{\max}$ is obtained for systems where the percentage of mutant keratin is between 15 and 30% i.e. where the results from simulations reproduce the results obtained in experiments, is located in the red portion of the diagram, suggesting that the value obtained for $Q^{\max}$ is mainly due to the accumulation of keratin aggregates and the process of asymmetric binding of WT and mutant particles.

4.4.3 Sensitivity Analysis

We have carried out a full sensitivity analysis of the model regarding variations of the parameters λ_W^{SP}, λ_M^{SP}, λ_W^{PF}, λ_M^{PF}, λ_{agg}, γ and χ_M. With this objective, we carried out positive and negative variations of 10% as well as doubling and halving each parameter, and calculated the corresponding variation in Q. We started from the state with $\lambda_{\text{agg}} = 10^4$, $\gamma = 5$ and $\chi_M = \chi_M^{\max} = 0.13$. For these parameters we have $Q^{\max} = 37$. The percentual changes in Q after varying each parameter are presented in Table 4.2 We observe that Q has

Table 4.2: Percentual Variation in Q

Parameter	**+10%**	**−10%**	$\times\frac{\mathbf{1}}{\mathbf{2}}$	**×2**
λ_W^{SP}	+1.29	−3.19	−34.13	−35.20
λ_M^{SP}	−0.7	−1.8	−73.5	−18.9
λ_W^{PF}	−4.7	+5.26	+33.9	−32.6
λ_M^{PF}	−4.8	+5.5	+40.7	−30.18
λ_{agg}	+4.8	−5.23	−32.6	+33.9
γ	+1.9	−8.8	−92.17	−14.9
χ_M	−4.31	−7.6	−94.15	−59.05

a relatively large sensitivity regarding all parameters in the model, with a large percentual variation on the same order of magnitude as the percentual variation of most parameters. In fact, for the larger variations of the reaction rates tried (by doubling or halving the value of each parameter), we observe typically a large variation in Q (by approximately 30%). The sensibility of Q is even larger with respect to variations in γ and χ_M.

4.4.4 Alternative Models

To further strengthen the argument that asymmetric binding of WT and mutant keratin is essential for the formation of keratin aggregates, we present two alternative models for reaction networks. By showing that the results coming from these two models are not in accordance with what is seen in experiments we can recognize the importance the asymmetric binding hypothesis.

Model I

The first alternative model considers the symmetrical aggregation of WT and mutant keratin. In a non-dimensional formulation, it contains seven variables: s_W, s_M, p_W, p_M, f_W and f_M, describing the same quantities as in the main model, and a the concentration of aggregates in the cytoplasm. As opposed to the main model, here, there is only one variable describing keratin aggregates instead of two. These aggregates are formed, by hypothesis, by adding WT and mutant soluble keratin in equal proportions with a rate $k_{\text{agg}} S_W S_M$. The conclusions reached with this model are independent of which keratin form we use to form the aggregates i.e., the results are similar if we use $k_{\text{agg}} P_W P_M$. In its non-dimensional form, the system of ODEs that models the reaction network is

$$
\begin{aligned}
\frac{\mathrm{d}s_W}{\mathrm{d}\tau} &= -\lambda_W^{SP} s_W + p_W + f_W + \frac{1}{2}a - \lambda_{\text{agg}} s_W s_M \\
\frac{\mathrm{d}s_M}{\mathrm{d}\tau} &= -\lambda_M^{SP} s_M + p_M + f_M + \frac{1}{2}a - \lambda_{\text{agg}} s_W s_M \\
\frac{\mathrm{d}p_W}{\mathrm{d}\tau} &= \lambda_W^{SP} s_W - p_W - \lambda_W^{PF} p_W \\
\frac{\mathrm{d}p_M}{\mathrm{d}\tau} &= \lambda_M^{SP} s_M - p_M - \lambda_M^{PF} p_M \\
\frac{\mathrm{d}f_W}{\mathrm{d}\tau} &= \lambda_W^{PF} p_W - f_W \\
\frac{\mathrm{d}f_M}{\mathrm{d}\tau} &= \lambda_M^{PF} p_M - f_M \\
\frac{\mathrm{d}a}{\mathrm{d}\tau} &= \lambda_{\text{agg}} s_W s_M - a\,.
\end{aligned}
$$

This model has only one unknown parameter, k_{agg}. We explored the stationary state of this system of equation for different values of λ_{agg} and fractions of mutant keratin, χ_M. In

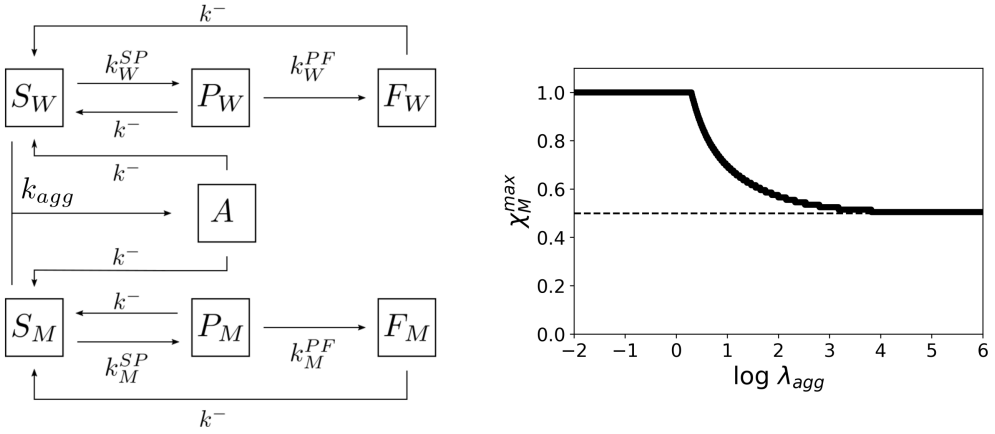

FIGURE 4.5: Reaction network diagram for Model I (left). Fraction of mutant keratin at which Q is maximum as a function of $\log_{\lambda_{\text{agg}}}$ (right). The dashed line represents $\chi_M^{\max}$ to which the curve converges as $\log_{\lambda_{\text{agg}}}$ increases.

Figure 4.5 right, we plot the fraction of mutant keratin where the value of Q is maximum

as a function of λ_{agg}. For values of λ_{agg} in the range $10^{-2} < \lambda_{\text{agg}} < 1$, the maximum value of Q is located at $\chi_M^{\max}$,i.e. for cells that contain only mutant keratin. By increasing λ_{agg}, the maximum starts shifting to lower values until it stagnates at $\chi_M^{\max}$ for large λ_{agg}.

Clearly this model is not able to reproduce what was observed in experiment as the aggregates have by design equal amounts of WT and mutant keratin. Moreover, it is important to notice that, contrary to the experimental observations, in this model $\chi_M^{\max}$ is always above 50%, regardless of the value of λ_{agg}. To understand the reason for this, consider a cell with 50% WT and 50% mutant keratin. As the formation of mutant filaments is a slower and less efficient process, the fraction of mutant keratin in the soluble and granular phases is larger than the fraction of WT keratin in those phases. Therefore, the percentage of both soluble and granular keratin will increase faster by adding mutant keratin to the system than by adding WT keratin. As the formation of aggregates will depend on the amount of soluble keratin in the system, more aggregates will be formed in this model when the amount mutant keratin is above 50% (and a similar conclusion would be reached if the aggregates were formed by adding keratin granules instead).

We have further explored the symmetric 1:1 binding scenario between WT and mutant keratins by considering different soluble to particle reaction rates. Also, in this scenario, we did not identify a region of parameter space which reproduced the experimental observations. Here, we explored the hypothesis that the process of transforming soluble WT keratin into WT particles is slower than its mutant counterpart. With this assumption, we expect an accumulation of WT keratin in the soluble phase that will allow the formation of more aggregates for lower values of mutant keratin fraction. However, we observe experimentally that though cells with 100% mutant keratin are able to form filament networks, they do not have a higher density of keratin fibers than the cells that only express WT keratin. Therefore, for the model to truly reproduce the results observed experimentally, we also need to verify that the total amount of fibers, $F_W + F_M$, is either approximately equal or higher in the WT cells ($\chi_M = 0$) than in the mutant cells ($\chi_M = 1$).

This model's reaction network is the same as before (Figure 4.5) but instead of only varying λ_{agg}, we will also explore how different values of $\beta_{\text{SP}} = \lambda_W^{SP}/\lambda_M^{SP}$ affects the formation of keratin aggregates.

In Figure 4.6A we can observe that there is a region of values for the parameters β_{SP} and λ_{agg} where the maximum amount of aggregates is at $0.10 < \chi_M^{\max} < 0.30$. When $\beta_{SP} > 0.1$ the system behaves very similarly to what was observed above: in that regime, as we increase the value of λ_{agg}, the maximum of aggregates goes from being located at $\chi_M^{\max} \approx 1$ to $\chi_M^{\max} \approx 0.5$. In this region, the equilibrium fraction of keratin in the soluble phase is still smaller in WT cells than in mutants, and therefore the formation of aggregates will occur faster at high concentrations of mutant keratin. As λ_W^{SP} gets smaller (for a fixed value of λ_M^{SP}), we see that for a limited range of λ_{agg}, the maximum of aggregates happens for $\chi_M^{\max} < 0.5$. In this domain, there is a higher accumulation of WT keratin in the soluble phase which means that the amount of soluble mutant keratin required to promote

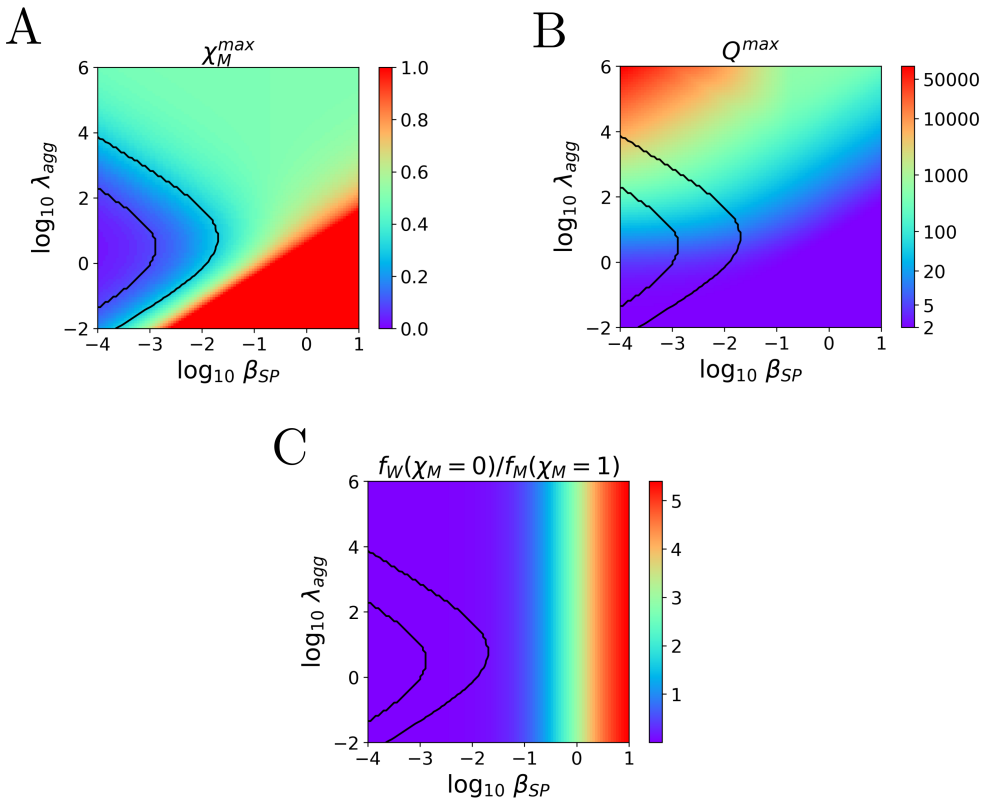

FIGURE 4.6: Value of $\chi_M^{\max}$ (A) and $Q^{\max}$ (B) as a function of λ_{agg} and β_{SP}. In (C) we represent the ratio between the fiber fraction of cells with 100% WT keratin and the fiber fraction in cells that are 100% mutant. The black curves bound the region where $0.10 < \chi_M^{\max} < 0.30$.

aggregation will be smaller and, when $\beta_{SP} \approx 10^{-4}$ we have aggregate formation with a fraction of mutant keratin in the system below 50%.

In Figure 4.6B we see the value of $Q^{\max}$ as a function of the same parameters. Inside the region delimited by black lines, we observe a large accumulation of aggregates for $\lambda_{\text{agg}} > 10$, according to what is expected from experiments. However, when we look at the ratio between the amount of fibers in cells expressing 100% WT keratin and in cells expressing 100% K14R125P mutant (Figure 4.6C) we see that if $\lambda_W^{SP} < 0.1\lambda_M^{SP}$ (i.e. in the region where we observe $\chi_M^{\max} < 0.50$) the model predicts that the fiber network of mutant cells is one order of magnitude denser than the fiber networks of WT cells. Thus, we conclude that a symmetric binding mechanism between WT and mutant soluble keratin cannot explain the results observed in experiment, even if we consider that the reaction where WT particles are formed is much slower than its mutant counterpart. In this case, we see that by slowing down formation of WT particles we are creating a bottleneck and limiting the formation of WT keratin fibers.

Model II

To address the difficulties identified by Model I in replicating the results obtained in the experiments, a new reaction network model was hypothesized (shown in Figure 2 left). Analogously to Sun et al 2015, in this model we consider that aggregates are initially nucleated by both mutant and WT keratin through a process with reaction rate k_{nuc}. These aggregates can then grow by the addition of both WT and mutant keratin particles in the soluble phase, with a rate $k^{\text{agg}}_{W/M} S_{W/M}(A_W + A_M)$, where k^{agg}_W and k^{agg}_M are not necessarily identical. The equations that model this reaction network are given by (in non-dimensional form):

$$
\begin{aligned}
\frac{\mathrm{d}s_W}{\mathrm{d}\tau} &= -\lambda^{SP}_W s_W + p_W + f_W + a_W - \lambda_{\text{nuc}} s_W s_M - \lambda^{\text{agg}}_W s_W (a_W + a_M) \\
\frac{\mathrm{d}s_M}{\mathrm{d}\tau} &= -\lambda^{SP}_M s_M + p_M + f_M + a_M - \lambda_{\text{nuc}} s_W s_M - \lambda^{\text{agg}}_M s_M (a_W + a_M) \\
\frac{\mathrm{d}p_W}{\mathrm{d}\tau} &= \lambda^{SP}_W s_W - p_W - \lambda^{PF}_W p_W \\
\frac{\mathrm{d}p_M}{\mathrm{d}\tau} &= \lambda^{SP}_M s_M - p_M - \lambda^{PF}_M p_M \\
\frac{\mathrm{d}f_W}{\mathrm{d}\tau} &= \lambda^{PF}_W p_W - f_W \\
\frac{\mathrm{d}f_M}{\mathrm{d}\tau} &= \lambda^{PF}_M p_M - f_M \\
\frac{\mathrm{d}a_W}{\mathrm{d}\tau} &= \lambda_{\text{nuc}} s_W s_M + \lambda^{\text{agg}}_W s_W (a_W + a_M) - a_W \\
\frac{\mathrm{d}a_M}{\mathrm{d}\tau} &= \lambda_{\text{nuc}} s_W s_M + \lambda^{\text{agg}}_M s_M (a_W + a_M) - a_M
\end{aligned}
$$

This model introduces two additional reaction rates λ^{agg}_W and λ^{agg}_M for which there is no

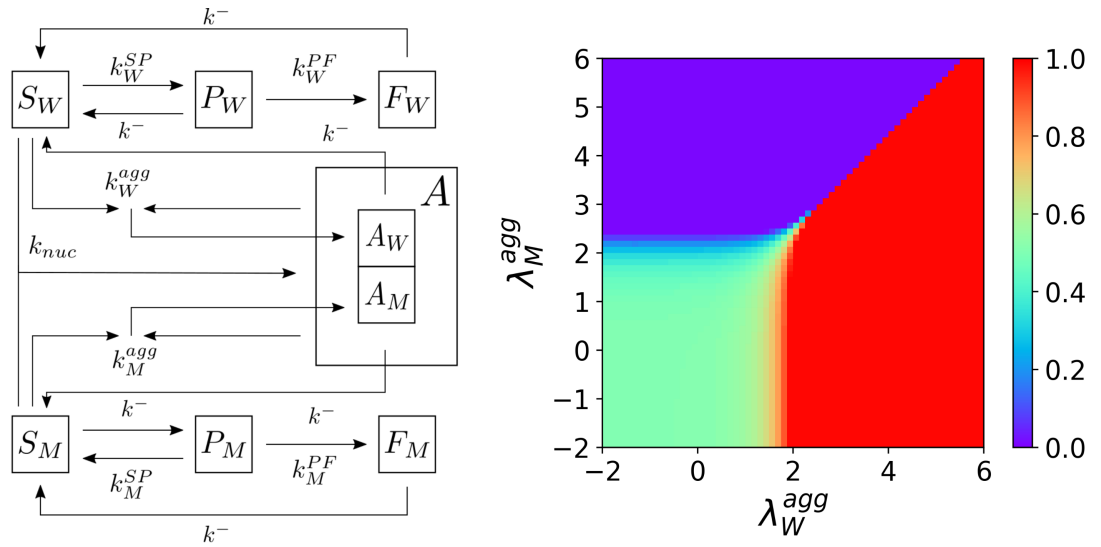

FIGURE 4.7: Reaction network for Model II (left). Fraction of mutant keratin at which Q is maximum as a function of λ^{agg}_W and λ^{agg}_M (right).

measured value available in literature. We solved the system of equations and explored

their steady state for different values of λ_W^{agg} and λ_M^{agg}. The value of λ_{nuc} was fixed at 10^3, a typical reaction rate for aggregation according to the results of the model in the main text (though a similar behavior was observed for a wide range of λ_{nuc} values).

In Figure 2 right we represent the value of $\chi_M^{\max}$ as a function of the value of the two aggregation rates. The diagram is essentially divided in 3 main regions with very sharp transitions between them. The light green region corresponds to results where $\chi_M^{\max} \approx 0.5$, in the red region $\chi_M^{\max} \approx 1$ and finally the purple region where $\chi_M^{\max} \approx 0$. The green region is defined by $\lambda_W^{\text{agg}} < 100$ and $\lambda_M^{\text{agg}} < 100$ and here the aggregation constants are small and the aggregates grow by the nucleation process as in Model I. In the purple region, the reaction rate for WT aggregation is larger than the reaction rate for mutant aggregation. Therefore, once there is a small amount of keratin that permits the formation of the aggregation nuclei, the WT keratin is able to attach to those nuclei and grow the aggregate. In this situation the higher the concentration of WT keratin, the larger the fraction of aggregates in the cell. As a consequence we obtain $\chi_M^{\max}$ at a concentration of mutant keratin vanishingly small. In the red region the similar reasoning can be made, and the maximum is reached with a very small quantity of WT keratin. For this model, aggregates can therefore be asymmetric, but very small fractions of mutated keratins can give rise to overwhelming aggregate formation, which is clearly not verified experimentally.

4.5 Conclusions and Future Work

The peek of aggregate concentration at low mutant keratin levels was reproduced in our mathematical model if we hypothesized WT and mutant keratin bind asymmetrically to form aggregates. The extensive exploration of minimal models where WT and mutant keratins bind at a 1:1 ratio predicted, opposite to what was observed experimentally, a maximum of agglomerate formation at mutant keratin fractions above 50%. We also explored the hypothesis of a nucleating oligomer formed by both WT and mutant keratin that could grow by the addition of WT keratin. This second hypothesis also did not reproduce the experimental results. Interestingly two previous studies on vimentin, an intermediate filament protein that builds homopolymeric filaments, bear similarities to our mathematical model's explanation of the findings we obtained on the K14R125P mutation. Namely, about 25% of mutant vimentin is enough to cause disruption of the endogenous filament network [36], while the influence of the same vimentin mutations on cataract formation in the eye lens of mice [37] showed that animals expressing less than 30% of mutant vimentin had in their tissues cytoplasmic vimentin inclusions that also contained endogenous WT vimentin.

Therefore, our mathematical model predicts that aggregates are the result of the asymmetric binding of WT and mutant keratins, with a ratio $\gamma : 1$, where $\gamma > 1$. This agrees with the imbalance between the two types of keratin recovered from the pellets. Finally, when the fraction of mutant keratin is such that the concentration of aggregates is maximum, the model predicts that the concentration of keratin in the aggregates is at least one order of

magnitude larger than the amount of keratin in the filaments in the cell. Therefore, in these conditions, the keratin aggregates will be ubiquitous in the cell, just as observed. In a future study we will address quantitatively the variability observed in keratin aggregation at the cell level. Introducing variability in the reaction rates of the model will also permit to better explore quantitatively these measured amounts of keratin.

Chapter 5

Simulating Blood Vessel Structures with a Multi-Phase Field Model

5.1 Motivation

For many decades, *de novo* vascular network formation via vasculogenesis has been extensively studied, and the same is true for angiogenesis. These processes are responsible for the formation of blood vessel networks, although the end product, in both cases, is an immature network that must undergo reorganization and remodeling to evolve into fully functional oxygen and nutrient distribution systems. Understanding vessel network remodeling can shed light into processes such as embryogenesis, organ formation and the appearance of vascular abnormalities associated with a wide range of disease.

Vascular pruning refers to the removal of a connection that existed between two vessels, with cell apoptosis being one of the main mechanisms by which the vessel disappears. This phenomenon has been identified in the mouse pupillary membrane and hyaloid canal [97, 98]. In the mouse retina, however, it has been shown that vessel regression can occur without significant apoptotic activity [99]. In zebrafish models, endothelial cell reorganization was recognized as the main driver of vascular remodeling in the brain [100].

In Franco et al. (2015), a four step process for vessel pruning was proposed, to explain how vascular remodeling can occur without cell apoptosis [101]. In Figure 5.1, we can see confocal images of the four steps proposed in that paper and a drawing showing a more detailed look on the role of several agents in the process of vessel pruning. Endothelial cell polarization can be measured in these vessels and observed to be induced by blood flow and will point in the opposite direction of that flow. The polarization of endothelial cells is closely related to the relative positioning of their Golgi apparatus with respect to the nucleus, as depicted in Figure 5.1 i), ii) and iii). The first step begins with the selection of which vessel will regress. At this stage, the vessel is lumenized and stable due

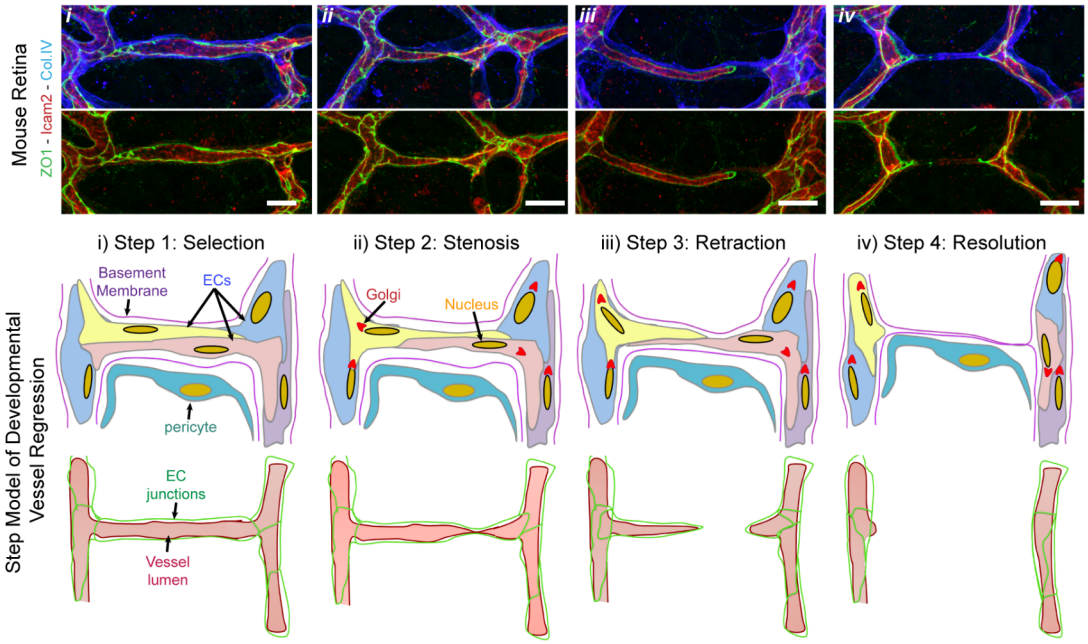

FIGURE 5.1: Vessel regression observed in a mouse retina (upper panel) and a diagram depicting each step of the process (bottom panel).

to the supporting role of perycites, strong adhesion at cell-cell junctions and the existence of a basement membrane. Afterwards, the selected vessel will undergo stenosis, meaning that the lumen will narrow and the blood flow in the selected segment will be restricted. After the blood flow is completely cut off in the regressing vessel, the cells that were previously organized to form its structure, will start migrating in the direction of their polarization, towards the vessels closest to them, that present a high blood flow. In the end, all that remains of the pruned vessel is its supporting structure of pericytes and basement membrane, since the lumen has also regressed.

The fact that the process, described above, conserves the number of cells in the system, highlights how important it is to understand how endothelial cells organize in a vessel structure and how stimuli-driven cell reorganization can lead to morphological changes, both in each individual cell and on the multi cellular system as a whole. With the model described in this chapter, we will explore how cells can organize in a tubular structure when subject to a polarization source, as well as how the migration of one cell can lead to the rearrangement of its neighbors to form a sprout.

5.2 Model Description

The model described in this section is based on the ideas presented in [102] and [103]. We have developed a multi-phase field model, in three dimensions, to describe a group of endothelial cells that form a tubular structure resembling a blood vessel. Besides modeling each cell individually using a set of order parameters $\{\phi_i\}$, we also describe the extracellular matrix and the vascular lumen, each represented by their own order parameter, ϕ_{ecm} and ϕ_{lumen}, respectively. Figure 5.2 represents a depiction of the system that will be modeled.

In this chapter, the value of all order parameters used will vary between $\phi = 0$ and $\phi = +1$.

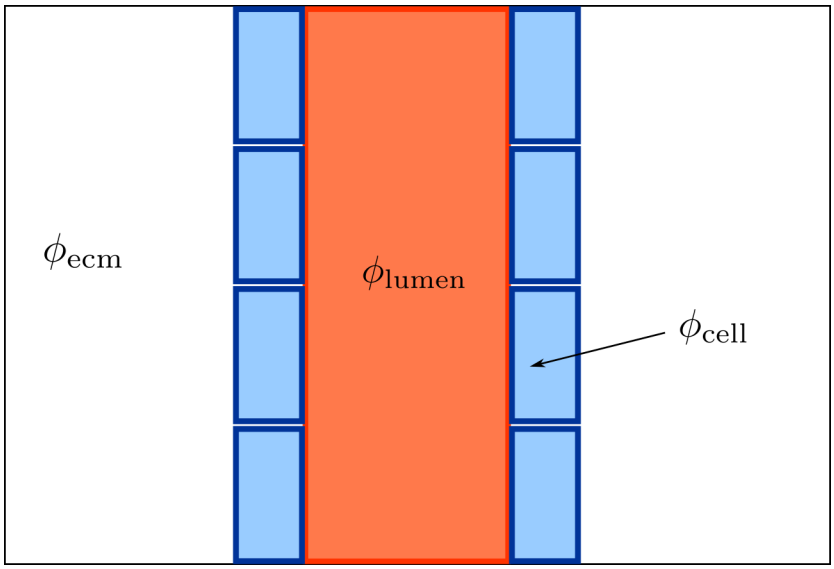

FIGURE 5.2: Illustration of the system being modeled (2D slice). The location of the labels show the region where the order parameter is equal to one.

5.2.1 Free Energy Functional

In the free energy functional of the system, besides the usual Ginzburg-Landau term common to most phase field models, we include energy terms that describe the interactions between endothelial cells, the ECM and the vascular lumen. The free energy functional will be a sum of three terms, one for each tissue we wish to represent:

$$F\left[\{\phi_i\}, \phi_{\text{ecm}}, \phi_{\text{lumen}}\right] = F^{\text{cells}} + F^{\text{ecm}} + F^{\text{lumen}}\,. \tag{5.1}$$

In this model, we assume that the dynamics of the system is driven by two main interactions: adhesion and repulsion. Besides these two, an extra term is added to ensure cell volume conservation.

Adhesion Energy

The functional that gives the adhesion energy between cells described by the order parameters ϕ_i and ϕ_j is given by

$$F^{\text{adh}}\left[\phi_i, \phi_j\right] = \frac{\eta_{ij}}{12} \int \boldsymbol{\nabla} h(\phi_i) \cdot \boldsymbol{\nabla} h(\phi_j)\, \mathrm{d}\mathbf{r} \tag{5.2}$$

where $h(\phi) = \phi^2(3 - 2\phi)$ and η_{ij} is an adhesion parameter that measures the adhesion energy density between ϕ_i and ϕ_j, and has units of J m^{-1}. From equation 5.2 we see that if the two cells are far from each other, the value of the functional is zero, since the dot product between the gradient terms (that are non-zero only at the interfaces) is null. In the case where the two cells are in contact, the adhesion term is no longer zero and it will

have a negative value, lowering the energy. Notice that $\boldsymbol{\nabla} h(\phi)$ points from the outside of the cell to the inside and so, when two cells overlap, the gradient terms will point to the inside of each cell but in opposite directions such that the dot product is a negative number. To avoid the existence of non-physical self-adhesion terms, the adhesion energy is only calculated between distinct cells (with distinct order parameters).

The functional derivative of $F^{\text{adh}}[\phi_i, \phi_j]$ with respect to one of the fields, ϕ_i in this case, is given by

$$\begin{aligned} \frac{\delta F^{\text{adh}}}{\delta \phi} &= -\frac{\eta_{ij}}{12} h'(\phi_i) \nabla^2 h(\phi_j) \\ &= -\frac{\eta_{ij}}{2} \phi_i (1 - \phi_i) \nabla^2 h(\phi_j) \,. \end{aligned} \tag{5.3}$$

Repulsion Energy

For the model to be realistic, making sure that two cells do not occupy the same volume is of great importance. That is achieved by adding a repulsion term between cells that ensures the excluded volume condition. The repulsion energy term between two cells described by ϕ_i and ϕ_j is given by

$$F^{\text{rep}}[\phi_i, \phi_j] = \frac{\beta_{ij}}{12} \int h(\phi_i) h(\phi_j) \, \mathrm{d}\mathbf{r} \tag{5.4}$$

where β_{ij} is the repulsion coefficient between cells represented by ϕ_i and ϕ_j, that has units of J m^{-3}. To the integral in 5.4 contribute points where the product $h(\phi_i)h(\phi_j)$ is not zero, which occurs only in regions where the two cells overlap. The more common points they share, the higher the energy gets, such that the behavior of cells that minimizes the overall energy is to not occupy the same space.

The functional derivative of $F^{\text{rep}}[\phi_i, \phi_j]$ with respect to one of the fields, ϕ_i in this case, is given by

$$\begin{aligned} \frac{\delta F^{\text{rep}}}{\delta \phi} &= \frac{\beta_{ij}}{12} h'(\phi_i) h(\phi_j) \\ &= \frac{\beta_{ij}}{2} \phi_i (1 - \phi_i) h(\phi_j) \,. \end{aligned} \tag{5.5}$$

Volume Conservation

Another important term that must be added to the model is an energy functional that maintains the cell volume approximately constant throughout the simulations. The corresponding energy term is given by

$$F^{\text{volume}}[\phi_i] = \frac{1}{12} \alpha_V \left(V_{\text{cell}}^T - V[\phi_i] \right)^2 \,. \tag{5.6}$$

where α_V is a penalization parameter with units of J m^{-6}, V^T_{cell} is the target volume chosen for the cell, and $V[\phi_i]$ is the current volume of the cell, given by

$$V[\phi_i] = \int h(\phi)\, \mathrm{d}\mathbf{r} \ . \tag{5.7}$$

Calculating the functional derivative of 5.6 we obtain

$$\frac{\delta F^{\text{volume}}}{\delta \phi_i} = -\alpha_V \phi_i (1-\phi_i) \left(V^T_{\text{cell}} - \int h(\phi_i)\, \mathrm{d}\mathbf{r} \right) . \tag{5.8}$$

In Figure 5.3, we present a diagram that represents the different components of the system (endothelial cells, vascular lumen and ECM) and the interactions between each of them, that are included in the model. Besides the adhesion and repulsion forces that occur between the distinct phases, there is also endothelial cell-cell adhesion and repulsion, as well as the degradation of the ECM by matrix metallo-proteases (MMPs) produced by tip cells. In the next sections we write the free energy functional for endothelial cells, the

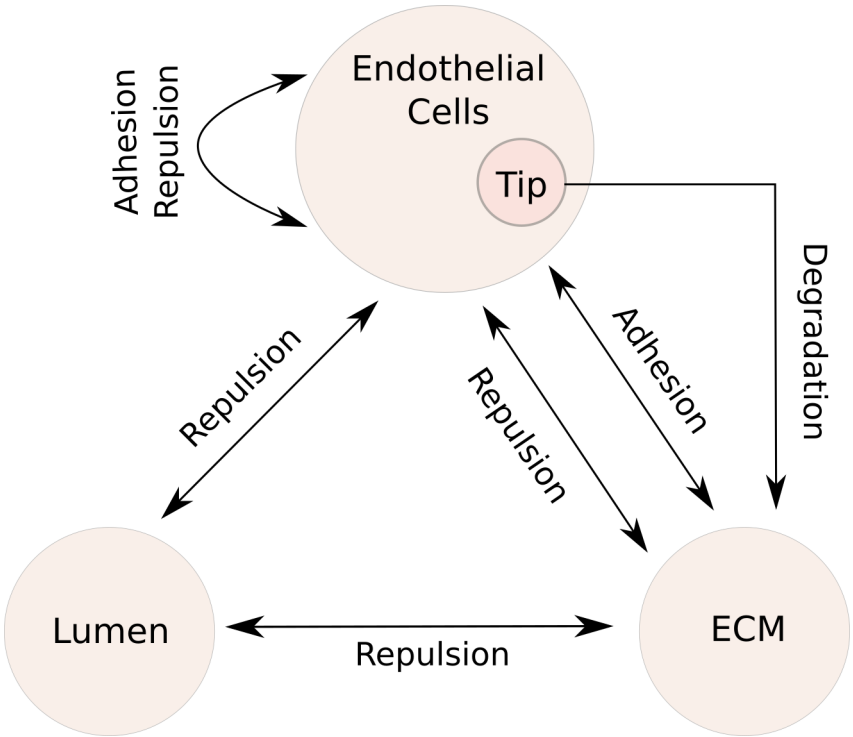

FIGURE 5.3: Diagram representing the different interactions between every component of the system. Double ended arrows represent interactions that are mutual.

lumen and the ECM, taking into account the interactions represented in Figure 5.3.

Endothelial Cell Free Energy F^{cells}

The contribution of endothelial cells to the system free energy can be written as

$$\begin{aligned} F^{\text{cells}} = &\sum_{i=1}^{N_{\text{cell}}} \int \left[\frac{\epsilon^2}{2} |\boldsymbol{\nabla}\phi_i|^2 + \frac{1}{4}\phi_i^2(1-\phi_i)^2 \right] \mathrm{d}\mathbf{r} + \frac{1}{12} \sum_{i=1}^{N_{\text{cell}}} \alpha_V \left(V_{\text{cell}}^T - V[\phi_i] \right)^2 \\ &+ \frac{1}{12} \sum_{i=1}^{N_{\text{cell}}} \sum_{j \neq i}^{N_{\text{cell}}} \int \left[\beta_{\text{cell}}^{\text{cell}} h(\phi_i) h(\phi_j) + \eta_{\text{cell}}^{\text{cell}} \boldsymbol{\nabla} h(\phi_i) \cdot \boldsymbol{\nabla} h(\phi_j) \right] \mathrm{d}\mathbf{r} \\ &+ \frac{1}{12} \sum_{i=1}^{N_{\text{cell}}} \int \left[\beta_{\text{ecm}}^{\text{cell}} h(\phi_i) h(\phi_{\text{ecm}}) + \eta_{\text{ecm}}^{\text{cell}} \boldsymbol{\nabla} h(\phi_i) \cdot \boldsymbol{\nabla} h(\phi_{\text{ecm}}) \right] \mathrm{d}\mathbf{r} \\ &+ \frac{1}{12} \sum_{i=1}^{N_{\text{cell}}} \int \beta_{\text{lumen}}^{\text{cell}} h(\phi_i) h(\phi_{\text{lumen}}) \, \mathrm{d}\mathbf{r} \end{aligned} \tag{5.9}$$

In Nonomura et al. (2012) [102], in order to simplify the expression for the Allen-Cahn equation that gives the time evolution of each order parameter in the model, and to aid the parallelization of the numerical methods used to solve it, introduced an auxiliary for each type of cell in the model. In this model, we define

$$\begin{aligned} \Phi_{\text{cell}} &= \sum_{i=1}^{N_{\text{cell}}} h(\phi_i) \\ \Phi_{\text{ecm}} &= h(\phi_{\text{ecm}}) \\ \Phi_{\text{lumen}} &= h(\phi_{\text{lumen}}) \end{aligned} \tag{5.10}$$

a field that represents the sum of all cells of the same type. Rewriting 5.9 using these new variables, we have that

$$\begin{aligned} F^{\text{cells}} = &\sum_{i=1}^{N_{\text{cell}}} \int \left[\frac{\epsilon^2}{2} |\boldsymbol{\nabla}\phi_i|^2 + \frac{1}{4}\phi_i^2(1-\phi_i)^2 \right] \mathrm{d}\mathbf{r} + \frac{1}{12} \sum_{i=1}^{N_{\text{cell}}} \alpha_V \left(V_{\text{cell}}^T - V[\phi_i] \right)^2 \\ &+ \frac{1}{12} \int \left[\beta_{\text{cell}}^{\text{cell}} \Phi_{\text{cell}}^2 + \eta_{\text{cell}}^{\text{cell}} |\boldsymbol{\nabla}\Phi_{\text{cell}}|^2 \right] \mathrm{d}\mathbf{r} \\ &- \frac{1}{12} \sum_{i=1}^{N_{\text{cell}}} \int \left[\beta_{\text{cell}}^{\text{cell}} h(\phi_i)^2 + \eta_{\text{cell}}^{\text{cell}} |\boldsymbol{\nabla} h(\phi_i)|^2 \right] \mathrm{d}\mathbf{r} \\ &+ \frac{1}{12} \int \left[\beta_{\text{ecm}}^{\text{cell}} \Phi_{\text{cell}} \Phi_{\text{ecm}} + \eta_{\text{ecm}}^{\text{cell}} \boldsymbol{\nabla}\Phi_{\text{cell}} \cdot \boldsymbol{\nabla}\Phi_{\text{ecm}} \right] \mathrm{d}\mathbf{r} \\ &+ \frac{1}{12} \int \beta_{\text{lumen}}^{\text{cell}} \Phi_{\text{cell}} \Phi_{\text{lumen}} \, \mathrm{d}\mathbf{r} \end{aligned} \tag{5.11}$$

where the fourth term in the sum appears to exclude self-interactions in cells.

ECM Free Energy F^{ecm}

The ECM free energy has all the terms already present in (5.11) regarding the interactions with the group of endothelial cells plus the excluded volume between the matrix and the lumen. As opposed to endothelial cells, the volume of the ECM is not conserved during

the simulation.

$$\begin{aligned} F^{\text{ecm}} = &\int \left[\frac{\epsilon^2}{2} |\boldsymbol{\nabla}\phi_{\text{ecm}}|^2 + \frac{1}{4}\phi_{\text{ecm}}^2(1-\phi_{\text{ecm}})^2 \right] \mathrm{d}\mathbf{r} \\ &+ \frac{1}{12}\int \left[\beta_{\text{ecm}}^{\text{cell}} \Phi_{\text{cell}}\Phi_{\text{ecm}} + \eta_{\text{ecm}}^{\text{cell}} \boldsymbol{\nabla}\Phi_{\text{cell}} \cdot \boldsymbol{\nabla}\Phi_{\text{ecm}} \right] \mathrm{d}\mathbf{r} \\ &+ \frac{1}{12}\int \beta_{\text{lumen}}^{\text{cell}} \Phi_{\text{cell}}\Phi_{\text{lumen}} \, \mathrm{d}\mathbf{r} \ . \end{aligned} \tag{5.12}$$

Lumen Free Energy F^{lumen}

Finally, the lumen free energy contains all the terms already presented in (5.11) and (5.12) plus a term representing the radial pressure exerted by the lumen on the surrounding cells and tissue. Just like the ECM, the volume of the lumen is also not conserved explicitly on the free energy. The free energy term regarding the lumen order parameter is given by

$$\begin{aligned} F^{\text{lumen}} = &\int \left[\frac{\epsilon^2}{2} |\boldsymbol{\nabla}\phi_{\text{lumen}}|^2 + \frac{1}{4}\phi_{\text{lumen}}^2(1-\phi_{\text{lumen}})^2 \right] \mathrm{d}\mathbf{r} \\ &+ \frac{1}{12}\int \left[\beta_{\text{lumen}}^{\text{cell}} \Phi_{\text{cell}} + \beta_{\text{lumen}}^{\text{ecm}} \Phi_{\text{ecm}} \right] \Phi_{\text{lumen}} \, \mathrm{d}\mathbf{r} \\ &- \frac{1}{6}\int p\Phi_{\text{lumen}} \, \mathrm{d}\mathbf{r} \end{aligned} \tag{5.13}$$

where p is the luminal pressure.

In the next section, we will derive the equations that give the time evolution of the order parameters in the model, from the free energy functional presented above.

5.2.2 Model Equations

The dynamics of each order parameter, ϕ_i, used in the model to describe each distinct phase, will be given by the Allen-Cahn equation corresponding to a phase field model A,

$$\frac{\partial \phi_i}{\partial t} = -\frac{\delta F}{\delta \phi_i} \, ,$$

where the mobility constant M is equal to 1, by adjusting the time scale.

For each order parameter, ϕ_i, that describes an endothelial cell, the corresponding equation for its time evolution is given by

$$\frac{\partial \phi_i}{\partial t} + \boldsymbol{\nabla} \cdot (\phi_i \mathbf{u_i}) = \epsilon^2 \nabla^2 \phi_i + \phi_i \left(1-\phi_i\right) \left[\phi_i - \frac{1}{2} + \alpha_V \left(V_{\text{cell}}^T - V[\phi_i] \right) + f_i^{\text{int}} \right] \tag{5.14}$$

where $\mathbf{u_i}$ is the advection velocity where endothelial cell polarization and tip cell velocity will be included, as described later in the chapter. All the extra terms that represent the

interaction between phases are included in f_i^{int}, given by

$$\begin{aligned} f_i^{\text{int}} = &- \beta_{\text{cell}}^{\text{cell}} \left[\Phi_{\text{cell}} - h(\phi_i)\right] - \beta_{\text{ecm}}^{\text{cell}} \Phi_{\text{ecm}} - \beta_{\text{lumen}}^{\text{cell}} \Phi_{\text{lumen}} \\ &+ \eta_{\text{cell}}^{\text{cell}} \left[\nabla^2 \Phi_{\text{cell}} - \nabla^2 h(\phi_i)\right] + \eta_{\text{ecm}}^{\text{cell}} \nabla^2 \Phi_{\text{ecm}} \,. \end{aligned} \tag{5.15}$$

For the extracellular matrix, described by ϕ_{ecm}, the corresponding Allen-Cahn equation is given by

$$\frac{\partial \phi_{\text{ecm}}}{\partial t} = \epsilon^2 \nabla^2 \phi_{\text{ecm}} + \phi_{\text{ecm}} \left(1 - \phi_{\text{ecm}}\right) \left[\phi_{\text{ecm}} - \frac{1}{2} + f_{\text{ecm}}^{\text{int}}\right] . \tag{5.16}$$

where the interaction function, $f_{\text{ecm}}^{\text{int}}$ is

$$f_{\text{ecm}}^{\text{int}} = -\beta_{\text{ecm}}^{\text{cell}} \Phi_{\text{cell}} - \beta_{\text{lumen}}^{\text{ecm}} \Phi_{\text{lumen}} + \eta_{\text{ecm}}^{\text{cell}} \nabla^2 \Phi_{\text{cell}} \,. \tag{5.17}$$

Finally, the dynamics of the lumen order parameter, ϕ_{lumen}, follows the equation

$$\frac{\partial \phi_{\text{lumen}}}{\partial t} = \epsilon^2 \nabla^2 \phi_{\text{lumen}} + \phi_{\text{lumen}} \left(1 - \phi_{\text{lumen}}\right) \left[\phi_{\text{lumen}} - \frac{1}{2} + p + f_{\text{lumen}}^{\text{int}}\right] , \tag{5.18}$$

where the interaction terms are included in $f_{\text{lumen}}^{\text{int}}$,

$$f_{\text{lumen}}^{\text{int}} = -\beta_{\text{lumen}}^{\text{cell}} \Phi_{\text{cell}} - \beta_{\text{lumen}}^{\text{ecm}} \Phi_{\text{ecm}} \,. \tag{5.19}$$

Numerical Methods

To solve the equations presented above, we discretize the spacial and temporal derivatives using the finite difference method. For the time derivative, we use a forward differentiation scheme where

$$\phi_i^{t+1} = \phi_i^t + \Delta t \left(\frac{\partial \phi_i}{\partial t}\right)^t ,$$

while for spatial derivatives we employ centered differences formulas.

5.2.3 Cell Polarization

Blood flow induced endothelial cell polarization is an important phenomenon to study the arrangement of cells in a vessel structure. In this work, we do not model the blood flow explicitly, but we include the effects it has on endothelial cell elongation and movement. It will be shown in the results section, considering the effects of blood flow is essential if we want to obtain a vessel-like tubular structure where the cells have realistic shapes, when comparing with experimental observations. In Figure 5.4 we show how blood induces an anti-parallel polarization on endothelial cells, leading to cell elongation and shape change. To model this phenomenon, we first find the two extreme points of the cell in the direction of the flow (assumed to be alligned with the z-axis), $(z_{\min}, z_{\max})$, as well as the coordinates of the cell center of mass, $\mathbf{r}_{\text{com}}$. The center of mass is calculated using a weighted average,

$$\mathbf{r}_{\text{com}} = \frac{\int h(\phi_i) \mathbf{r} \, \mathrm{d}\mathbf{r}}{\int h(\phi_i) \, \mathrm{d}\mathbf{r}} = (x_{\text{com}}, y_{\text{com}}, z_{\text{com}}) \,. \tag{5.20}$$

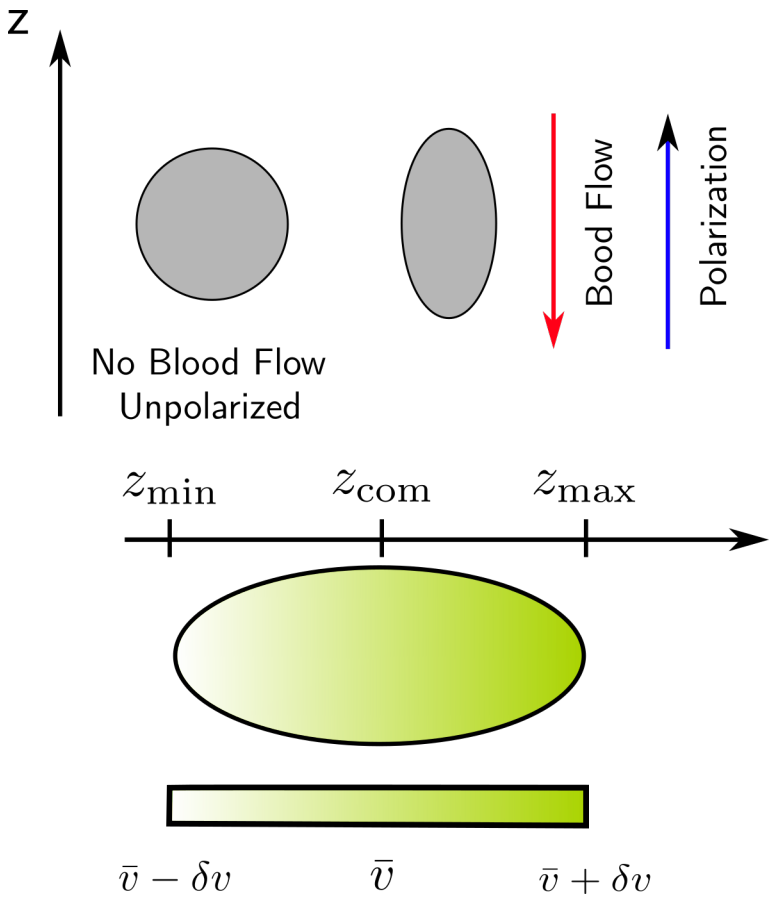

FIGURE 5.4: Diagram representing the different interactions between every component of the system. Double ended arrows represent interactions that are mutual.

We assume the blood flow induces a velocity field on each cell in the z-axis, that increases linearly from the points where $z = z_{\min}$ to where $z = z_{\max}$. The induced velocity is given by

$$v_z(z) = h(\phi_i)\left[\overline{v} + \frac{2z - z_{\max} - z_{\min}}{z_{\max} - z_{\min}}\delta v\right]. \tag{5.21}$$

An illustration of the velocity field, which varies linearly between $\overline{v} - \delta v$ and $\overline{v} + \delta v$, can be seen in the bottom image of Figure 5.4.

5.2.4 ECM Degradation

When we want to simulate a sprouting event, one of the endothelial cells in the tubular structures will start migrating in a perpendicular direction to the initial vessel. Since the tubular structure is surrounded by the ECM, in order to move, the tip cell must produce MMPs that will degrade the matrix and open space for the cell to migrate. To introduce the effects of MMPs in the model, we introduce a diffusion equation that governs the release of proteases by the tip cell. This dynamics is given by

$$\frac{\partial C_{\text{MMP}}}{\partial t} = D_{\text{MMP}}\nabla^2 C_{\text{MMP}} - k_{\text{MMP}} C_{\text{MMP}} + \gamma\phi_{\text{tip}} \tag{5.22}$$

where D_{MMP} and k_{MMP} are, respectively, the diffusion and decay rate of MMPs. The last term in the above equation regulates the production of MMPs by the tip cell, described by ϕ_{tip}, at a rate γ.

The effects of MMP on the order parameter that describes the ECM, ϕ_{ecm}, is modeled by adding an extra term to equation 5.16, given by $-\delta_{\mathrm{MMP}}\phi_{\mathrm{ecm}}C_{\mathrm{MMP}}$. This term will decrease the value of ϕ_{ecm} at a rate controlled by δ_{MMP}, when the concentration of MMPs at that point is greater than zero.

5.2.5 Cell Division

While tip cells have an increased sensibility to growth factor gradients, that will guide their migration, stalk cells have few VEGF receptors and their main task is cell proliferation. To model stalk cell proliferation, we must implement how we can turn one parent cell into two daughter cells, which, in practice, means defining two new order parameter fields from a preexisting one. To do that we will use the method presented in [102] and [103] where, given two points $\mathbf{p_1}$ and $\mathbf{p_2}$, an order parameter field is divided in two, with the plane of division being defined by a plane that contains both $\mathbf{p_1}$ and $\mathbf{p_2}$. Starting from a parent cell, described by ϕ_{parent}, we define two new order parameters ϕ_{A} and ϕ_{B}, such that

$$\begin{aligned}\phi_{\mathrm{A}}(\mathbf{r}) &= \phi_{\mathrm{parent}}(\mathbf{r})\xi(\mathbf{r};\mathbf{p_1},\mathbf{p_2}) \\ \phi_{\mathrm{B}}(\mathbf{r}) &= \phi_{\mathrm{parent}}(\mathbf{r})\left[1-\xi(\mathbf{r};\mathbf{p_1},\mathbf{p_2})\right] ,\end{aligned} \tag{5.23}$$

where the function $\xi(\mathbf{r};\mathbf{p_1},\mathbf{p_2})$ is a three dimensional step function that describes one half of 3D space, when it is bissected by a plane defined by $\mathbf{p_1}$ and $\mathbf{p_2}$. The function $1-\xi(\mathbf{r};\mathbf{p_1},\mathbf{p_2})$ describes the other half. $\xi(\mathbf{r};\mathbf{p_1},\mathbf{p_2})$ is defined as

$$\xi(\mathbf{r};\mathbf{p_1},\mathbf{p_2}) = \frac{1}{2}\left[1+\tanh\chi(\mathbf{r};\mathbf{p_1},\mathbf{p_2})\right] \tag{5.24}$$

where $\chi(\mathbf{r};\mathbf{p_1},\mathbf{p_2})$ is defined by

$$\chi(\mathbf{r};\mathbf{p_1},\mathbf{p_2}) = \frac{\mathbf{p_1}-\mathbf{p_2}}{|\mathbf{p_1}-\mathbf{p_2}|}\cdot\left(\mathbf{r}-\frac{\mathbf{p_1}+\mathbf{p_2}}{2}\right) . \tag{5.25}$$

To completely define how the division will occur, we must define which points $\mathbf{p_1}$ and $\mathbf{p_2}$ that we will use to define the bissection plane. To do this we determine the minimum bounding box that encloses the whole parent cell and determine which dimension of the box is largest. $\mathbf{p_1}$ and $\mathbf{p_2}$ will correspond to the two points where the cell intersects the bounding box in the direction where it is the most stretched.

In the end, the two daughter cells will have the same properties of the parent cell with their order parameter fields given by equation 5.23.

5.3 Results and Discussion

5.3.1 Initial Conditions

Before running a simulation, we must first define the initial geometry of the system, by initializing each order parameter field. The initial tubular structure is built by assembling layers of endothelial cells. In the top two images of Figure 5.5 we plot the initial conditions for the vessel where the cells form a cylinder with a hollow section in the middle, where the lumen will be initialized. The initial configuration of ϕ_{ecm} is not shown in the figure,

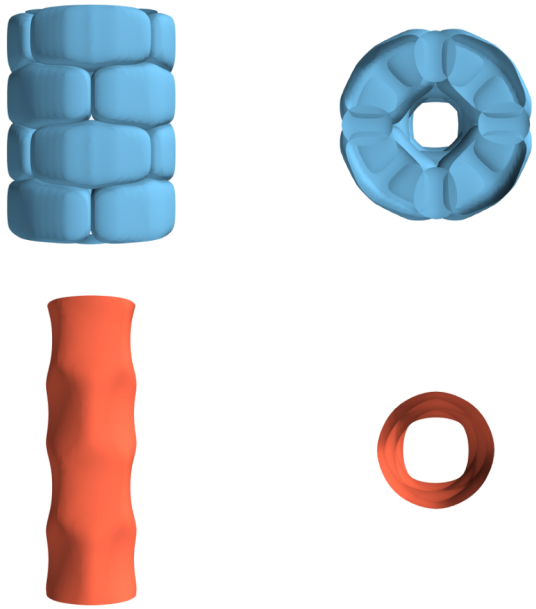

FIGURE 5.5: Initial configurations of the vessel structure (top) and the vascular lumen (bottom). These images where taken after a few iterations to allow the system to create a smooth interface. The surfaces show correspond to $\phi_i^{\text{cell}} = 0.5$ and $\phi_{\text{lumen}} = 0.5$. All the space outside the wall made up of endothelial cells has $\phi_{\text{ecm}} = 1$. The lumen is enclosed by the endothelial cells.

but it surrounds the endothelial cell tubular structure and fills the remaining space in the computational domain. Unless stated, the values of the parameters used in the simulations presented in the next sections are: the repulsion between the components of the system is the same for every interaction pair i.e. $\beta_{\text{cell}}^{\text{cell}} = \beta_{\text{ecm}}^{\text{cell}} = \beta_{\text{lumen}}^{\text{ecm}} = \beta_{\text{lumen}}^{\text{cell}} = 1$; cell-matrix adhesion is greater than cell-cell adhesion, with $\eta_{\text{cell}}^{\text{cell}} = 0.05$ and $\eta_{\text{ecm}}^{\text{cell}} = 0.10$.

5.3.2 Cell Arrangement in a Tubular Structure

Starting from the initial configuration presented shown in Figure 5.5 we evolve the order parameters in time, until a steady state configuration is achieved. In Figure 5.6 we can see the organization of the tubular endothelial cell structure and the shape of the lumen, in a steady state. Analyzing Figures 5.6A, C and D, we see that the lumen grows until it reaches a stable radius. The pressure it exerts on the endothelial cells, flattens these against the extracellular matrix that surrounds the vessel, until a balance between the lumen pressure and the ECM repulsion is achieved. In Figure 5.6A, it is noticeable the

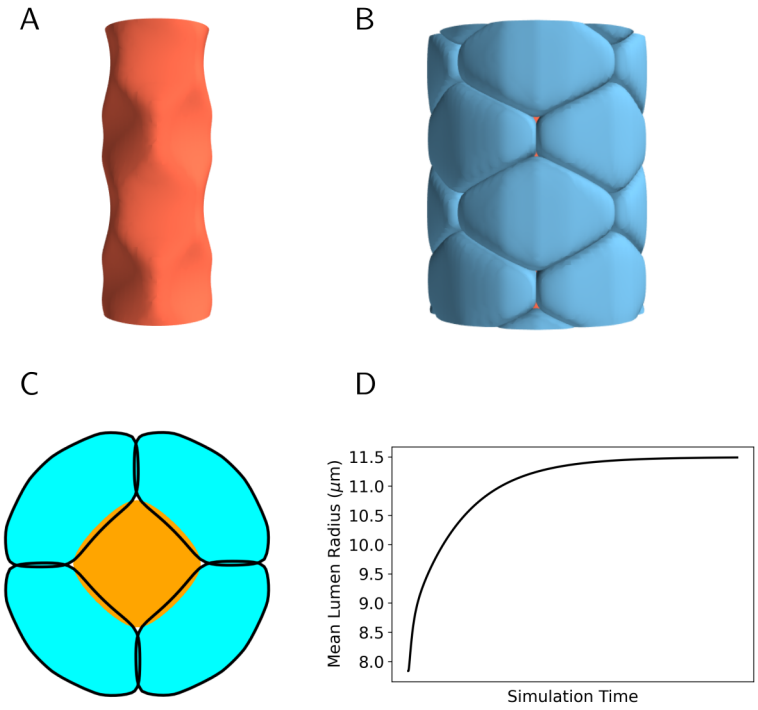

FIGURE 5.6: Equilibrium structure of the lumen (A) and the endothelial cell tube (B). Two dimensional slice of the tube cells (blue) and lumen (orange) taken at $z = 10$, with contour lines corresponding to $\phi_i^{\text{cell}} = 0.5$ (C). Mean lumen radius as a function of time (D).

deformation of the lumen caused by the endothelial cells, which can be further seen in Figure 5.6C, where we show a 2D cross section of the tubular structure.

The problem with the results presented in Figure 5.6 is visible when we look at the shape of the endothelial cells that line the vessel. All cells present, approximately, the same shape, which is not compatible to what is normally seen in reality, where there is a greater variability in cell shape. To try and achieve a more realistic endothelial cell distribution, we introduce a polarization field that models the effect of blood flow inside the vessel, inducing cell rearrangement.

5.3.3 Endothelial Cell Polarization

In this section we present the effects of blood flow induced polarization on endothelial cell organization in a vessel. To take into account the cell movement that comes from this polarization, we introduce a velocity field that is parallel to the tubular structure and in the opposite direction of blood flow. There are two components to this velocity field: one has a translational effect represented by the velocity applied to the center of mass of each cell, $\overline{v}$, which, in this section has a value between $\overline{v} = 0.25 - 0.35$ μm/s. Each cell will be assigned a random value of $\overline{v}$ in this range. The inhomogeneity in the velocity that depends on the elongation of the cell in the direction of the flow is determined by the parameter δv. In Figure 5.7 we show how endothelial cells organize in a vessel, when they

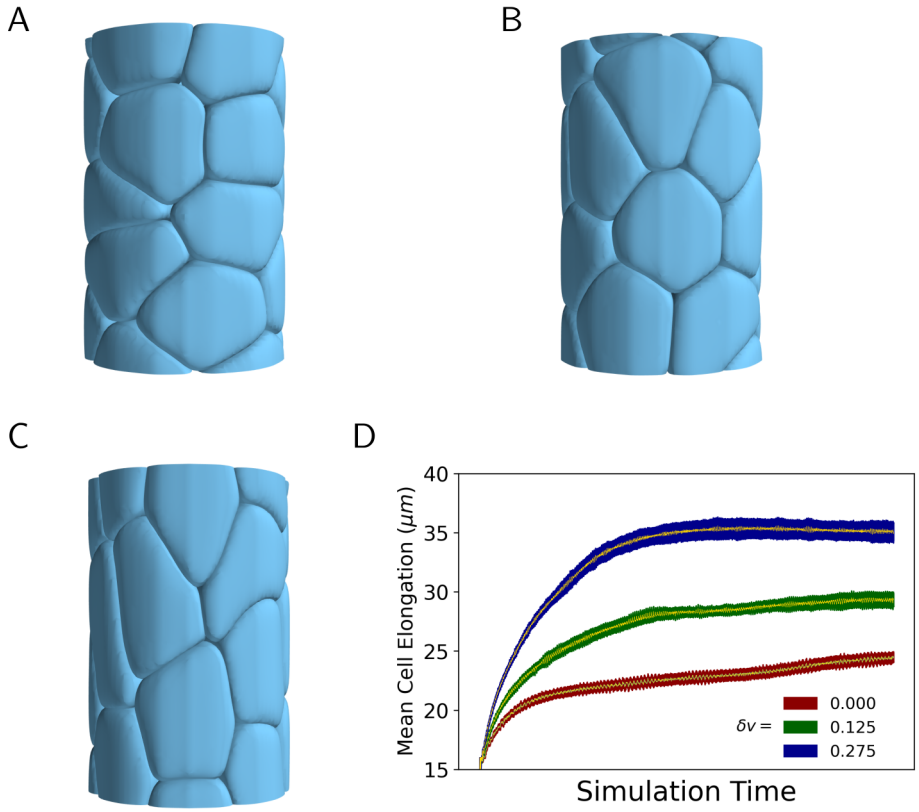

FIGURE 5.7: Endothelial cell organization in a vessel as a function of δv: 0.0 (A), 0.125 (B) and 0.275 μm/s (C). Average cell elongation as a function of time for different values of δv (D).

are polarized. In Figure 5.7A, $\delta v = 0$, meaning the velocity of the cell does not depend on how stretched it is and has a value $\overline{v}$ everywhere. However, due to the distinct values of $\overline{v}$ randomly assigned to each cell, we can see that there is a larger variety in cell shapes when compared to the ones presented in Figure 5.6. The differences in $\overline{v}$ between cells creates a sort of friction between the cells' interfaces, leading to deformation that lead to cell shape changes. As we increase δv, in Figure 5.7B and C, we notice that cells become increasingly more elongated since the difference in velocity between the top and bottom portions of the cell are larger, creating a net elongation in the z-direction. To study how the value of δv leads to different cell elongation, we plot the average cell elongation as a function of time, for different values of δv. As expected, larger values of lead to higher values of cell elongation. This higher variability in cell shape due to cell polarization gives more realistic results for the shape of cells in a tubular structure.

5.3.4 Tip Cell Sprouting

Sprouting angiogenesis starts when an endothelial cell that lines a blood vessel starts migrating towards tissue that is in hypoxia and, as a result, produces vascular growth factor to stimulate the formation of new blood vessels to deliver oxygen. In this section we simulate a sprouting event starting from an initial tubular vessel. At a certain point, one of the cells described in the model will start migrating perpendicularly to the longitudinal

axis of the vessel and will start degrading the ECM by releasing MMPs. Depending on the velocity of the tip cell, the resulting sprout can have different lengths, and in extreme cases, where cell-cell adhesion is not able to keep the stalk cells connected to the tip cell, the leading cell can break away from the sprout and migrate alone. Here, we will explore how tip cell velocity and the existence of stalk cell proliferation lead to different sprout morphologies and the effect they have on the distance the tip cell migrates. In Figure 5.8A,

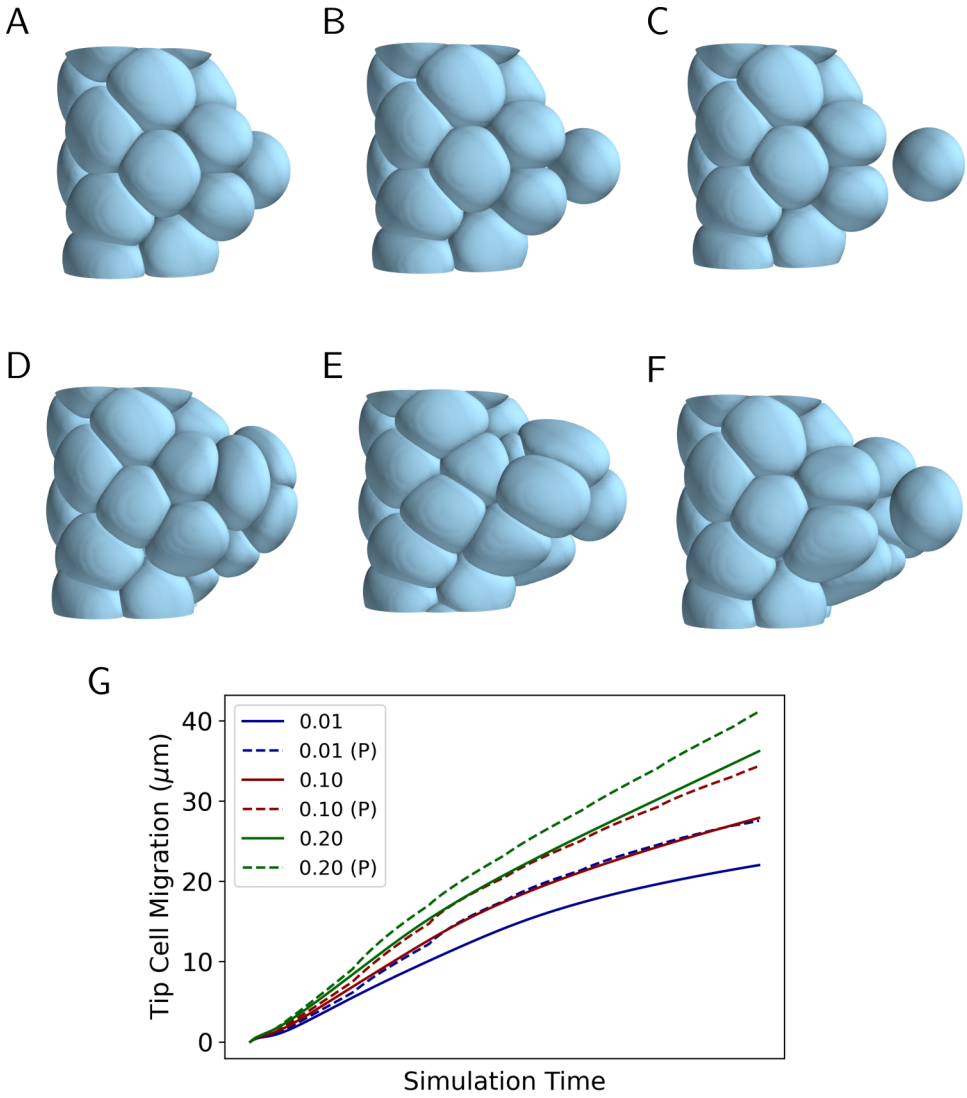

FIGURE 5.8: Sprout formation for different values of tip cell velocity: 0.01 (A,D), 0.1 (B,E) and 0.2 μm/s (C,F). The sprouts shown in the top panel (A,B,C) where obtained without stalk cell proliferation. Cell proliferation is used in (D,E,F). Tip cell migration distance as a function of time (in arbitrary units), for different values of tip cell velocity with (dashed) and without (continuous) stalk cell proliferation (G).

B and C, we show how, in the absence of stalk-cell proliferation, a sprout is formed from the initial vessel, depending on the tip cell velocity. In Figure 5.8A, $|\mathbf{v}_{\text{tip}}| = 0.01\ \mu\text{m}/s$, and we see the formation of a small protrusion from the vessel. Since tip cell velocity is low, cell-cell adhesion is able to secure the tip cell and it has difficulty migrating through the ECM, almost stop moving at about $\approx 20\ \mu$m from its initial position (Figure 5.8G). As we increase the velocity to $|\mathbf{v}_{\text{tip}}| = 0.1\ \mu\text{m}/s$, the tip cell migrates a bit further, and

it is visible, in Figure 5.8B that its connection to the neighboring stalk cells is weaker. Increasing the velocity further, we see that the tip cell completely detaches itself from the sprout, leaving behind the stalk cells. Since the cell is no longer interacting with other cells, it takes a more spherical shape, which minimizes the free energy of the interface.

To study how stalk cell proliferation can provide more support to the migrating tip cell, we use the cell division algorithm as described previously. At regular intervals during the simulation one cell (that is not the tip cell) can divide giving rise to two new ones. The cell that will be selected to undergo division will be the one that has the most surface contact with the tip cell. To measure cell-cell contact, for each cell, we calculate

$$\sigma_i = \int_V \boldsymbol{\nabla} h(\phi_i) \cdot \boldsymbol{\nabla} h(\phi_{\text{tip}}) \, \mathrm{d}\mathbf{r} \ .$$

The cell with the lowest value of σ_i (the integrand is negative, since the gradient of the order parameter for different cells will point in opposite directions) will be chosen to undergo cell division. Comparing the results in Figure 5.8 (D-F), with its counterparts with no proliferation, we can see that the sprouts are thicker and longer. In these simulation, the number of cells grows from 20 to 27 and due to the criterium used to choose which cell will divide, the structure behind the tip cell is more robust, which allows the vessel to elongate more without the tip cell breaking away. In Figure 5.8G, we can see how stalk cell proliferation increases the distance traveled by the tip cell, for all values of cell velocity. Comparing the dashed lines (corresponding to simulations with proliferation) with the continuous line of the same color, we see the distance traveled is always higher when there is stalk cell proliferation. Also, when $|\mathbf{v}_{\text{tip}}| = 0.2$ μm/s, for the system where the number of cells is constant, the tip cell breaks away from the sprout, which does not happen when stalk cells divide.

5.4 Conclusions and Future Work

In this chapter we have presented a multi-phase field model to study the behavior of endothelial cells in a vessel structure. We have shown that, in order to obtain a structure where cells have a realistic shape, we must take into account the polarization induced on them by the blood flow. Furthermore, we have shown that this model is capable of simulating the early steps of sprouting angiogenesis, when combined with stalk cell proliferation and the degradation of the extracellular matrix by MMPs. For a simple tubular structure, we have also achieved the formation of a stable lumen, which is an important step towards being able to study, for example, splitting angiogenesis, using this model. In this work, we have taken several steps into being able to simulate vessel regression, which was the motivation for this study. Some key aspects that are missing from the model are: refinement of lumen dynamics, especially during sprouting events; better capacity to simulate a larger number of cells in the system; optimization of the code used for the simulations and the ability to run it using multi-core capabilities.

One of the advantages of this multi-phase field model is its versatility, as it can be adapted to model different biological scenarios such as tumor growth, endothelial to mesenchymal transitions (EMTs) and the formation of metastasis. As such, the theoretical framework used in this model can be translated into a software library that could allow users to apply a multi-phase field approach to problems of their interest.

Chapter 6

Mechanical Model of Sprouting Angiogenesis

In this chapter a phase field model coupled with elasticity is used to study the process of sprouting angiogenesis. Studying how the mechanical properties of the extracellular matrix and the traction force exerted by the tip cells during migration lead to the formation of vessel networks with different morphologies is the main focus of this work. The experimental work presented in this chapter was performed at Coimbra Institute for Clinical and Biomedical Research (iCBR), that is a part of the Faculty of Medicine of the University of Coimbra.

6.1 Motivation

One of the most important processes in the angiogenic process is cell migration. The movement of the tip cell through the extracellular matrix is guided by the gradient of growth factors released by cells in hypoxia. This is only possible due to the existence of mechanical interactions, notably cell-cell adhesion and traction forces exerted by the tip cells, and as such it is expected that changing the mechanical properties of the agents involved in cell migration will lead to changes in the way vessel networks are formed.

The extracellular matrix is a fibrous three dimensional network of macromolecules and proteins, such as collagen and elastin, its ridigity spanning different orders of magnitude, vary for different types of tissue. Apart from physiological differences, certain pathologies can also lead to changes in the ECM composition resulting in deficient tissue connectivity and disrupting the dynamics of blood vessel networks that are established in that tissue. Besides the effect it has on angiogenesis, the mechanical properties of the ECM have also been shown to have an effect in gene expression and cell differentiation [104].

6.2 Background

The use of phase field models to describe sprouting angiogenesis were first introduced in Milde *et al.* (2008) [105] and in Travasso *et al.* (2011) to study the effect of tip

cell chemotaxis and stalk cell proliferation on the growth of vascular networks in two dimensions [29]. The model of Travasso *et al.* (2011) was also used to study the delivery of anti-angiogenic drugs to tumour vascular networks using nano particles [106]. Its extension to three dimensions was developed to study the effects of blood flow on vessel network morphology and on the formation of anastomoses [30, 107].

To understand how the mechanical properties of the extracellular matrix influence the formation of vessel networks and the migration of tip cells, we developed a phase field model that takes into account the elasticity of both the endothelial cells and the ECM. The work presented in this chapter is based on the model described in Santos-Oliveira et al. (2015) and on the dissertation written by myself for the conclusion of my master's degree [108, 109].

6.3 Experimental Work

Aortic ring assays have been one of the most popular experimental techniques to study angiogenesis. Its versatility allows studying angiogenesis, as well as other physiological processes associated with it, such as endothelial cell proliferation and migration, microvessel branching, and the effect of pro and anti-angiogenic drugs on those same processes. The collagen level of the substrate where the aortic ring is placed can also be varied to emulate ECMs with different mechanical properties.

The first step in a standard aortic ring assay protocol is the dissection of the aorta of the animal. For angiogenesis studies, aortas removed from mice are the most popular choice. After undergoing a cleaning process, the aorta is cut into rings and the resulting samples undergo an optional, but recommended, starvation process where they are deprived of growth factors. This is done to reset the endothelial cells sensitivity to the presence of growth factors, allowing an unbiased migratory response when placed in culture. After starvation, the aortic ring is placed in a matrix that will serve as substrate for cell migration. Usual choices for matrix composition are collagen, fibrin and Matrigel. Finally, a cocktail of growth factors, such as VEGF, are introduced in the culture to promote formation of new micro-vessels from the aorta. During and after, this process, the culture is observed using imaging techniques and in the end, the resulting images are analyzed to measure several observables such as sprout number and length, vessel area and endothelial cell migration distance. In Figure 6.1A we can see, on the left, a microscopy image taken from the aortic ring assay. On the right, we zoom into an area close to the exterior aorta wall where a new micro vasculature is forming and the activity of many endothelial cells is noticeable. The aorta slices in these experiments are very thin, with a thickness of approximately 0.5 mm, when compared to the radius of the Petri dish (35 mm). In Figure 6.1B the migration distance of endothelial cells is measured for five different values of collagen concentration between $0.5 - 2.5$ mg/ml. As the collagen concentration increases, we see that endothelial cells are able to migrate further and vessels start getting longer. However, when the collagen concentration reaches 1.5 mg/ml, the migration distance reaches its

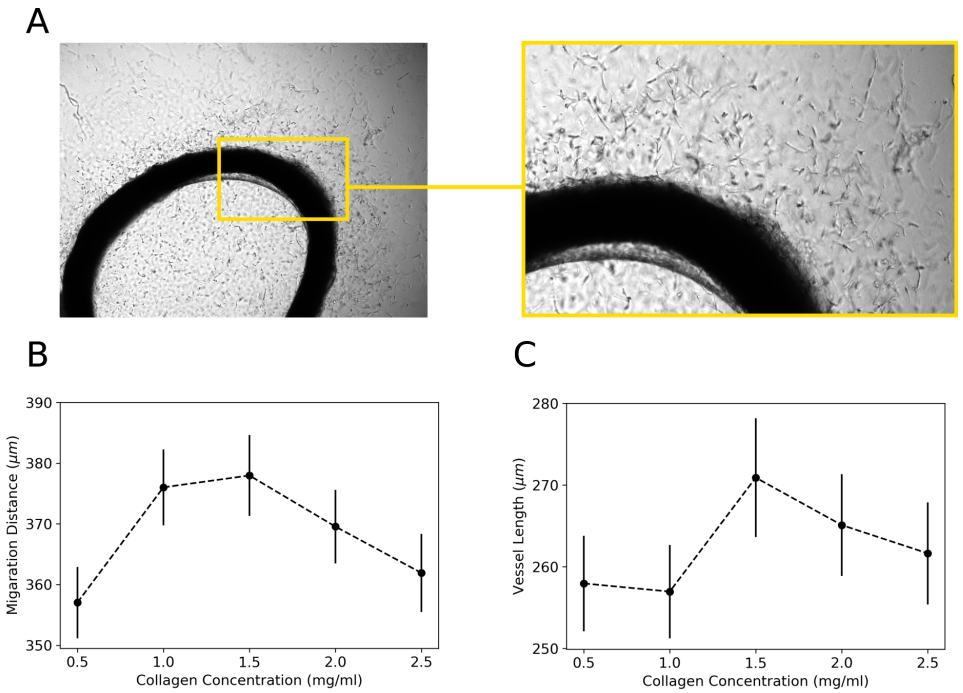

FIGURE 6.1: Image taken from the aortic ring assay using confocal microscopy. For better visualization, we zoom in a region near the aortic wall (A). Endothelial cell migration distance (B) and sprout length (C) as a function of the concentration of collagen used for the extracellular matrix, affecting the ECM rigidity.

maximum value, and for more rigid matrices, cells migrate less and vessels shorten. This non-monotonic dependence of cell migration on the rigidity of the matrix, suggests that the distance traveled by the tip cells depends on the interplay between two or more physical processes. In this work, we explore if varying ECM rigidity and the forces exerted by cells can replicate the experimental observations presented.

6.4 Model Description

In this model, a single order parameter $\phi(\mathbf{r})$ is used to describe the interface between endothelial cells and the extracellular matrix. Since we will not be modeling each endothelial cell individually, the value of $\phi(\mathbf{r})$ is an indicator as to whether a certain point in space is being occupied by endothelial cells, corresponding to $\phi(\mathbf{r}) \approx 1$, while in the absence of cells we assume that point is a part of the extracellular matrix and in that case, $\phi(\mathbf{r}) \approx -1$. The choice of values that the order parameter takes in each phase can be different leading to differences in the form of the free energy functional. The choice of $\phi = \pm 1$ is used on Santos-Oliveira et al.(2015) while in other models, $\phi = 0$ and $\phi = 1$ are used to identify each phase [108] (see also Chapter 5). All the relevant properties of the system, mainly the free energy that will drive the dynamics of the interface will be written as function of this order parameter.

6.4.1 Free Energy Functional

The free energy functional used in this phase field model is given by

$$\begin{aligned} F\left[\phi, \mathbf{u}, \mathbf{F}^{\text{cell}}\right] &= F^{\text{PF}}[\phi] + F^{\text{ela}}[\phi, \mathbf{u}] + F^{\text{cell}}[\phi, \mathbf{u}, \mathbf{F}^{\text{cell}}] \\ &= \int_V \left[\rho_\phi \left(f_0(\phi) + \frac{1}{2}\epsilon^2 |\boldsymbol{\nabla}\phi|^2\right) + \frac{1}{2}\sigma_{ij}\varepsilon_{ij} - F_i^{\text{cell}} u_i\right] \mathrm{d}V \end{aligned} \tag{6.1}$$

where F^{PF} is the Ginzburg-Landau free energy, F^{ela} is the elastic energy of the system, function of the displacement $\mathbf{u}$, and F^{cell} is the energy associated with the forces, $\mathbf{F}^{\text{cell}}$, exerted by the cells on the ECM (tip cell traction force) and the adhesion force that assures there is cohesion of the endothelial tissue.

The first term

$$F^{\text{PF}}[\phi] = \rho_\phi \int_V \left[f_0(\phi) + \frac{1}{2}\epsilon^2 |\boldsymbol{\nabla}\phi|^2\right] \mathrm{d}V \ . \tag{6.2}$$

dictates the values of ϕ inside each domain. The parameter ρ_ϕ gives the scale of the interface energy in the system. Since we want those values to be $\phi \approx \pm 1$ the natural choice for f_0 is

$$f_0(\phi) = -\frac{1}{2}a\phi^2 + \frac{1}{4}\phi^4$$

where a is a parameter whose value will be set further on in the model. The term proportional to $|\boldsymbol{\nabla}\phi|^2$ serves as an energy penalty to avoid the formation of a sharp interface, which means that rapid variations of ϕ will lead to an increase of the global energy and as such, the formation of a smooth, continuous interface of width ϵ is favored.

The elastic free energy $F^{\text{ela}}[\phi, \mathbf{u}]$ is given by

$$F^{\text{ela}}[\phi, \mathbf{u}] = \int_V \frac{1}{2}\sigma_{ij}\varepsilon_{ij} \, \mathrm{d}V \tag{6.3}$$

where σ_{ij} and ε_{ij} correspond to the components of the stress and strain tensors, respectively, which in turn are functions of the displacement field $\mathbf{u}$. The components of the stress tensor are a function of the components of the strain tensor given by the constitutive relation chosen for the material. As tissue and cells may have different elastic moduli, the elastic free energy is, in general, a function of ϕ as well. An extended analysis of this topic is given in the next section.

Finally, F^{cell} is associated to the energy accumulated by the forces applied by endothelial cells on each other and on the extracellular matrix, and is given by

$$F^{\text{cell}}\left[\phi, u_i, F_i^{\text{cell}}\right] = -\int_V F_i^{\text{cell}} u_i \, \mathrm{d}V \ . \tag{6.4}$$

In this model we consider that endothelial cells exert two distinct forces: a traction force applied by the tip cells that allows them to migrate, and a cell-cell adhesion force. Thus, the total force exerted by cells is the sum of those two components, such that

$$\mathbf{F}^{\text{cell}} = \mathbf{F}^{\text{adh}} + \mathbf{F}^{\text{tip}} \, . \tag{6.5}$$

where the adhesion force between endothelial cells is given by

$$\mathbf{F}^{\text{adh}} = \alpha \boldsymbol{\nabla} \phi \,. \tag{6.6}$$

and points towards the interior of the clusters of endothelial cells, where $\phi \approx +1$, and its strength is controlled by the parameter α. As will be shown in a further section, this force is what couples the phase field model for the description of the interface between the domains to the mechanical model used to describe the deformations in the elastic medium. $\mathbf{F}^{\text{tip}}$ models the traction forces that endothelial cells with a tip cell phenotype exert on the ECM. This force is calculated in an ellipse-shaped region centered at the tip cell position whose major axis is aligned with the direction of the gradient of VEGF that is sensed by the cell, and it is responsible for the migratory behavior of tip cells. Details about how this force is calculated will be discussed in a dedicated section. The way these forces are implemented in the model differs slightly from [108] since in this work we describe the forces exerted by cells as a more general vector field $\mathbf{F}^{\text{cell}}$ while in [108], the force was constrained to a curl-free vector i.e. $\mathbf{F}^{\text{cell}} = -\boldsymbol{\nabla} \chi^{\text{cell}}$.

6.4.2 Calculating the displacement field

Our aim with this model is to study how the mechanical properties of the extracellular matrix influence the sprouting of endothelial cells and as such it makes sense to describe the system using elasticity theory. We start by assuming that our system can be described using the linear approximation of elasticity theory and that the media is isotropic. In this way, the components of the stress tensor, σ_{ij} can be written in terms of the components of the strain tensor as

$$\sigma_{ij} = K(\phi)\delta_{ij}\varepsilon_{kk} + 2\mu(\phi)\left(\varepsilon_{ij} - \frac{\delta_{ij}}{D}\varepsilon_{kk}\right) \tag{6.7}$$

where D represents the dimensionality of the system, while K and μ are, respectively, the bulk modulus and rigidity of the system. K is related to the Lamé coefficient, λ, since

$$K = \lambda + \frac{2\mu}{D} \tag{6.8}$$

The later are both functions of ϕ meaning they have distinct values on the ECM ($\phi \approx -1$) and inside the endothelial tissue ($\phi \approx +1$) and so the system is generally elastically inhomogeneous. Their values are given by

$$\begin{aligned} \mu(\phi) &= \mu_0 - \mu_1 h(\phi) \\ K(\phi) &= K_0 - K_1 h(\phi) \end{aligned} \tag{6.9}$$

where μ_0, μ_1, K_0 and K_1 are constants and the function $h(\phi)$ is an interpolation function given by

$$h(\phi) = \frac{1}{2}\phi(3 - \phi^2)\,. \tag{6.10}$$

and represented in Figure 6.2.

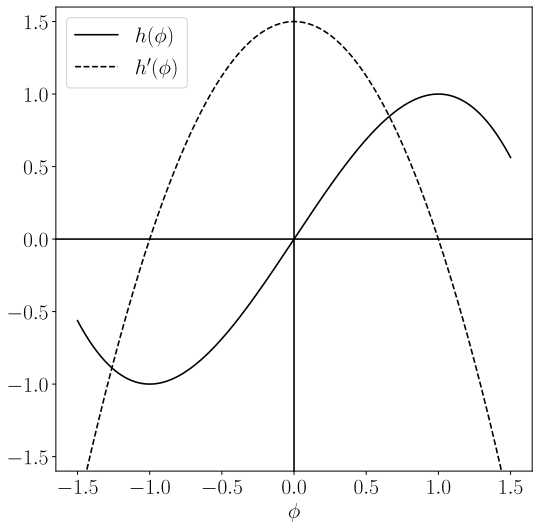

FIGURE 6.2: Graphical representation of the interpolating functions $h(\phi) = \frac{1}{2}\phi(3-\phi^2)$ and $h'(\phi) = \frac{3}{2}(1-\phi^2)$

From the definition of $\mu(\phi)$ and $K(\phi)$ we can establish a relation between μ_0, μ_1, K_0 and K_1 and the bulk and shear modulus of both phases (assuming $\mu_{\text{ecm}} = \mu(-1)$ and $\mu_{\text{ec}} = \mu(+1)$, and the same for the bulk modulus):

$$\begin{aligned} \mu_0 &= \frac{\mu_{\text{ecm}} + \mu_{\text{ec}}}{2} \\ K_0 &= \frac{K_{\text{ecm}} + K_{\text{ec}}}{2} \\ \mu_1 &= \frac{\mu_{\text{ecm}} - \mu_{\text{ec}}}{2} \\ K_1 &= \frac{K_{\text{ecm}} - K_{\text{ec}}}{2}\,. \end{aligned} \tag{6.11}$$

From the above relations we can see that the average shear and bulk modulus of the system are given by μ_0 and K_0, respectively, while $2\mu_1$ and $2K_1$ represent the difference in value of those properties between the two media and are a measure of the inhomogeneity in the mechanical properties of the system.

To calculate the displacement field as a function of the mechanical properties of the system and the forces applied by the cells, we assume that at each timestep the system reaches mechanical equilibrium implying that the effect of external forces are instantly propagated to every point in the material. This assumption is valid for the case in study since the relaxation time of the elastic medium is negligible compared to the time scale at which cell movement occurs. In a continuous medium, mechanical equilibrium requires that at every point in the domain, the following condition must hold

$$\partial_j \sigma_{ij} + F_i^{\text{cell}} = 0\,.$$

Using the constitutive relation 6.7 and the definition of the elastic parameters $\mu(\phi)$ and $K(\phi)$ the equilibrium equations are written as

$$\left(K_0 - \frac{2\mu_0}{D}\right)\partial_i\varepsilon_{jj} + 2\mu_0\partial_j\varepsilon_{ij} + F_i^{\text{cell}} + \\ -K_1\partial_i(h\varepsilon_{ll}) - \mu_1\left[2\partial_j(h\varepsilon_{ij}) - \frac{2}{D}\partial_i(h\varepsilon_{ll})\right] = 0\,.$$

which is a system of non-linear partial differential equations. It is, however, possible to simplify these equations, under certain conditions, especially since they can be expressed as the sum of a linear and a nonlinear term. In the linear elasticity regime, the strain tensor components are calculated from the displacement field using

$$\varepsilon_{ij} = \frac{1}{2}\left(\partial_i u_j + \partial_j u_i\right)$$

and plugging this definition into the linear part of the previous equation we get

$$\left(K_0 - \frac{2\mu_0}{D} + \mu_0\right)\partial_{ij}u_j + \mu_0\partial_{jj}u_i + F_i^{\text{cell}} + \\ -K_1\partial_i(h\varepsilon_{ll}) - \mu_1\left[2\partial_j(h\varepsilon_{ij}) - \frac{2}{D}\partial_i(h\varepsilon_{ll})\right] = 0\,.$$

We can define $L_0' = K_0 - \frac{2\mu_0}{D} + \mu_0$ and in the case where both $K_1 \ll L_0'$ and $\mu_1 \ll L_0'$ i.e. if the inhomogeneity in K and μ between the two media is very small, we can neglect the nonlinear terms and the condition for mechanical equilibrium becomes a linear PDE with an analytical solution

$$L_0'\partial_{ij}u_j^0 + \mu_0\partial_{jj}u_i^0 + F_i^{\text{cell}} = 0 \tag{6.12}$$

where u_i^0 are the components of the displacement field in the linear approximation. In Fourier space we can write the previous equation using the Green tensor for linear, isotropic materials, $G^{-1}(\mathbf{k})$, whose components are given by

$$G_{ij}^{-1}(\mathbf{k}) = \frac{1}{\mu_0|\mathbf{k}|^2}\left(\delta_{ij} - \frac{L_0 - \mu_0}{L_0}\frac{k_i k_j}{|\mathbf{k}|^2}\right)\,, \tag{6.13}$$

as

$$\hat{u}_i^0(\mathbf{k}) = G_{ij}^{-1}(\mathbf{k})\hat{F}_j^{\text{cell}}(\mathbf{k})\,, \tag{6.14}$$

where $L_0 = L_0' + \mu_0$ Since the use of the discrete Fourier representation of functions implies that the function is periodic, this solution is valid for periodic systems. Looking at the Green function we see it is not well defined when $\mathbf{k} = 0$ so for the system to have a unique solution we impose that $\hat{u}_i^0(\mathbf{k} = 0) = 0$. If we look at the definition of the Fourier transform of $\hat{u}_i^0$

$$\hat{u}_j^0(\mathbf{k}) = \int u_j^0(\mathbf{r})e^{-i\mathbf{k}\cdot\mathbf{r}}\,\mathrm{d}V\,,$$

imposing $\hat{u}_i^0(\mathbf{k}=0)=0$ means that

$$u_i^0(\mathbf{k}=0)=\int u_i^0(\mathbf{r})\,\mathrm{d}V=0$$

i.e. the average of u_i^0 in the domain is zero. Performing the inverse transform we get the displacement field everywhere in the domain and we can calculate the strain tensor components ε_{ij}.

6.4.3 Functional Derivative of the Free Energy

The temporal evolution of the order parameter field $\phi(\boldsymbol{r},t)$ follows a minimization principle of the free energy functional of the system. As such, calculating the functional derivative of the free energy with respect to ϕ is necessary. Since the functional derivative of a sum of functionals is the sum of the derivatives, we can calculate the functional derivative of each term in $F[\phi,u_i,F_i^{\mathrm{cell}}]$ separately. Starting with $F^{\mathrm{PF}}[\phi]$,

$$F^{\mathrm{PF}}[\phi+\delta\phi]=\int\rho_\phi\left[-a\frac{(\phi+\delta\phi)^2}{2}+\frac{(\phi+\delta\phi)^4}{4}+\frac{\epsilon^2}{2}\left(\boldsymbol{\nabla}\phi+\boldsymbol{\nabla}\delta\phi\right)^2\right]\mathrm{d}V$$

and making use of the binomial theorem expansion for $(x+y)^n$ and keeping only terms up to first order in $\delta\phi$ we get

$$\begin{aligned}F^{\mathrm{PF}}[\phi+\delta\phi]=&\int\rho_\phi\left[-a\frac{\phi^2+2\phi\delta\phi}{2}+\frac{(\phi^4+4\phi^3\delta\phi)}{4}+\right.\\&\left.+\frac{\epsilon^2}{2}\left(\boldsymbol{\nabla}\phi\cdot\boldsymbol{\nabla}\phi+2\boldsymbol{\nabla}\phi\cdot\boldsymbol{\nabla}\delta\phi\right)\right]\mathrm{d}V\ ,\end{aligned}$$

where we can recognize the terms of $F^{\mathrm{PF}}[\phi]$. Considering that, by definition, $\delta F=F[g+\delta g]-F[g]$, we rewrite the previous expression as

$$\delta F^{\mathrm{PF}}=\int\rho_\phi(-a\phi+\phi^3)\delta\phi\,\mathrm{d}V+\rho_\phi\epsilon^2\int\partial_i\phi\partial_i\delta\phi\,\mathrm{d}V\ .$$

The first integral in δF^{PF} is already in the form suitable for the calculation of the functional derivative using the definition. The second integral can be rewritten by using integration by parts i.e. using the product rule of differentiation

$$\int\partial_i\phi\partial_i\delta\phi\,\mathrm{d}V=\int\partial_i\left(\partial_i\phi\delta\phi\right)\mathrm{d}V-\int\partial_{ii}\phi\delta\phi\,\mathrm{d}V\ .$$

Using Gauss's theorem we can turn the first integral over the volume into a surface integral over its elements oriented with an S_i normal vector

$$\int\partial_i\phi\partial_i\delta\phi\,\mathrm{d}V=\int_S\left(\partial_i\phi\delta\phi\right)\mathrm{d}S_i-\int\partial_{ii}\phi\delta\phi\,\mathrm{d}V\ .$$

and since we are assuming our system has either periodic or zero flux boundary conditions at the surface of the domain, all surface integrals will be zero since there will always be

a zero net flux. Throughout the description of this model, this result will be used often. Finally, the functional derivative of F^{PF} when varying ϕ is

$$\frac{\delta F^{\mathrm{PF}}}{\delta \phi} = \rho_\phi \left(-a\phi + \phi^3 - \epsilon^2 \nabla^2 \phi \right) . \tag{6.15}$$

The elastic free energy density is given by

$$f^{\mathrm{ela}}(\phi, u_i) = \frac{1}{2} \sigma_{ij} \varepsilon_{ij} \tag{6.16}$$

and using zeroth order approximation for the displacement field, u_i^0 calculated in the previous section, we can write the energy density as

$$\begin{aligned} f^{\mathrm{ela}}(\phi, u_i) &= \frac{1}{2} \left[K(\phi) \delta_{ij} \varepsilon_{ll}^0 + 2\mu(\phi) \left(\varepsilon_{ij}^0 - \frac{1}{D} \delta_{ij} \varepsilon_{ll}^0 \right) \right] \varepsilon_{ij}^0 \\ &= \frac{1}{2} \left(K(\phi) - \frac{2\mu(\phi)}{D} \right) \varepsilon_{ii}^0 \varepsilon_{jj}^0 + \mu(\phi) \varepsilon_{ij}^0 \varepsilon_{ij}^0 . \end{aligned}$$

where ε_{ij}^0 are the components of the strain tensor calculated using u_i^0 as $2\varepsilon_{ij}^0 = \partial_i u_j^0 + \partial_j u_i^0$.

In order to calculate the variation of the elastic energy functional with respect to changes in ϕ we have to calculate $\delta\varepsilon_{ij}^0(\delta\phi)$ as well as $\delta F_i^{\mathrm{cell}}(\delta\phi)$. This last term is very simple to calculate since the only term in the force field that depends on the order parameter is the adhesion force

$$\delta F_i^{\mathrm{cell}} = \delta F_i^{\mathrm{adh}} = \alpha \partial_i \delta\phi . \tag{6.17}$$

To calculate $\delta\varepsilon_{ij}^0$ we need to calculate δu_i^0 which can be done by using the results in 6.13-6.14. In the Fourier domain, $\delta\hat{u}_i^0(\mathbf{k})$ is given by

$$\begin{aligned} \delta\hat{u}_i^0(\mathbf{k}) &= \frac{1}{\mu_0 |\mathbf{k}|^2} \left(\delta_{ij} - \frac{L_0 - \mu_0}{L_0} \frac{k_i k_j}{|\mathbf{k}|^2} \right) \delta\hat{F}_i^{\mathrm{cell}}(\mathbf{k}) \\ &= \frac{1}{\mu_0 |\mathbf{k}|^2} \left(\delta_{ij} - \frac{L_0 - \mu_0}{L_0} \frac{k_i k_j}{|\mathbf{k}|^2} \right) \alpha i k_j \delta\hat{\phi}(\mathbf{k}) \\ &= \frac{i\alpha k_i}{\mu_0 |\mathbf{k}|^2} \delta\hat{\phi}(\mathbf{k}) \left(1 - \frac{L_0 - \mu_0}{L_0} \right) \\ &= \frac{i\alpha k_i}{L_0 |\mathbf{k}|^2} \delta\hat{\phi}(\mathbf{k}) , \end{aligned} \tag{6.18}$$

which in real space translates into

$$\delta u_i^0 = -\frac{\alpha}{L_0} \Delta^{-1} \partial_i \delta\phi , \tag{6.19}$$

where the inverse laplacian operator Δ^{-1} is defined as

$$\Delta^{-1}(\nabla^2 f) = f . \tag{6.20}$$

Its definition in Fourier space is simply the product of a function of $f(\mathbf{k})$ and $-|\mathbf{k}|^{-2}$. Calculating the variation of the strain tensor components is now straightforward

$$\delta\varepsilon^0_{ij} = -\frac{\alpha}{L_0}\Delta^{-1}\partial_{ij}\delta\phi\,. \tag{6.21}$$

Another useful result is the variation of the trace of $\boldsymbol{\varepsilon}^0$

$$\begin{aligned}\delta\varepsilon^0_{ii} &= -\frac{\alpha}{L_0}\Delta^{-1}\partial_{ii}\delta\phi \\ &= -\frac{\alpha}{L_0}\delta\phi\,.\end{aligned} \tag{6.22}$$

Now that we have calculated the variation of the components of the strain tensor, ε_{ij}, we can calculate the variation of the elastic free energy

$$\begin{aligned}\delta F^{\text{ela}} &= \int \delta f^{\text{ela}}\,\mathrm{d}V \\ &= \int \left[\frac{1}{2}\left(\delta K - \frac{2\delta\mu}{D}\right)\varepsilon^0_{ii}\varepsilon^0_{jj} + \delta\mu\varepsilon^0_{ij}\varepsilon^0_{ij}\right. \\ &\left. + \left(K - \frac{2\mu}{D}\right)\varepsilon^0_{ii}\delta\varepsilon^0_{jj} + 2\mu\varepsilon^0_{ij}\delta\varepsilon^0_{ij}\right]\mathrm{d}V\,.\end{aligned} \tag{6.23}$$

The variations $\delta\mu$ and δK are given, respectively, by $-\mu_1 h'(\phi)\delta\phi$ and $-K_1 h'(\phi)\delta\phi$. Using the quantities calculated above, in the previous expression we have

$$\begin{aligned}\delta F^{\text{ela}} = &\int \left[-\frac{1}{2}\left(K_1 - \frac{2\mu_1}{D}\right)h'(\phi)\varepsilon^0_{ii}\varepsilon^0_{jj} - \mu_1 h'(\phi)\varepsilon^0_{ij}\varepsilon^0_{ij}\right]\delta\phi\,\mathrm{d}V \\ &- \int\left[\frac{\alpha}{L_0}\left(K - \frac{2\mu}{D}\right)\varepsilon^0_{ii}\delta\phi + \frac{2\mu\alpha}{L_0}\Delta^{-1}\left[\partial_{ij}\left(\mu\varepsilon^0_{ij}\right)\delta\phi\right]\right]\mathrm{d}V\,.\end{aligned} \tag{6.24}$$

By repetitively using integration by parts and considering that

$$\Delta^{-1}\partial_{ij}\varepsilon^0_{ij} = \Delta^{-1}\partial_{ii}\left(\partial_j u^0_j\right) = \varepsilon^0_{ii}\,,$$

then the functional derivative of the elastic free energy is given by

$$\begin{aligned}\frac{\delta F^{\text{ela}}}{\delta\phi} = &-\frac{1}{2}\left(K_1 - \frac{2\mu_1}{D}\right)h'(\phi)\varepsilon^0_{ii}\varepsilon^0_{jj} - \mu_1 h'(\phi)\varepsilon^0_{ij}\varepsilon^0_{ij} \\ &+ \frac{\alpha}{L_0}\left(K_1 - \frac{2\mu_1}{D}\right)h(\phi)\varepsilon^0_{ii} - \alpha\varepsilon^0_{ii} \\ &+ \frac{2\alpha\mu_1}{D}\Delta^{-1}\partial_{ij}\left[h(\phi)\varepsilon^0_{ij}\right]\,.\end{aligned} \tag{6.25}$$

Finally, the functional derivative of F^{cell} is given by

$$\frac{\delta F^{\text{cell}}}{\delta\phi} = \alpha\varepsilon^0_{ii} - \frac{\alpha^2}{L_0}\phi - \frac{\alpha}{L_0}\Delta^{-1}\partial_i F^{\text{tip}}_i\,, \tag{6.26}$$

allowing us to write the full expression for the functional derivative of the global free energy

$$\begin{aligned}\frac{\delta F}{\delta \phi} =&\rho_\phi \left[-\left(a + \frac{\alpha^2}{\rho_\phi L_0} \right) \phi + \phi^3 - \epsilon^2 \nabla^2 \phi \right] - \frac{1}{2} \left(K_1 - \frac{2\mu_1}{D} \right) h'(\phi) \varepsilon^0_{ii} \varepsilon^0_{jj} \\ &- \mu_1 h'(\phi) \varepsilon^0_{ij} \varepsilon^0_{ij} + \frac{\alpha}{L_0} \left(K_1 - \frac{2\mu_1}{D} \right) h(\phi) \varepsilon^0_{ii} \\ &+ \frac{\alpha}{L_0} \Delta^{-1} \left[2\mu_1 \partial_{ij} \left(h(\phi) \varepsilon^0_{ij} \right) - \partial_i F^{\text{tip}}_i \right] .\end{aligned} \tag{6.27}$$

Redefining a such that

$$a + \frac{\alpha^2}{\rho_\phi L_0} = 1 \,, \tag{6.28}$$

the expression for the derivative is simplified and we are left with

$$\begin{aligned}\frac{\delta F}{\delta \phi} =&\rho_\phi \left[-\phi + \phi^3 - \epsilon^2 \nabla^2 \phi \right] - \frac{1}{2} \left(K_1 - \frac{2\mu_1}{D} \right) h'(\phi) \varepsilon^0_{ii} \varepsilon^0_{jj} \\ &- \mu_1 h'(\phi) \varepsilon^0_{ij} \varepsilon^0_{ij} + \frac{\alpha}{L_0} \left(K_1 - \frac{2\mu_1}{D} \right) h(\phi) \varepsilon^0_{ii} \\ &+ \frac{\alpha}{L_0} \Delta^{-1} \left[2\mu_1 \partial_{ij} \left(h(\phi) \varepsilon^0_{ij} \right) - \partial_i F^{\text{tip}}_i \right] .\end{aligned} \tag{6.29}$$

6.4.4 Cahn–Hilliard Equation

The temporal dynamics of the interface associated with the order parameter $\phi(\boldsymbol{r}, t)$ used in this model is a variation of the Cahn–Hilliard equation typical of a phase field model B. In this case, the equation for the dynamics will be of the form

$$\frac{\partial \phi}{\partial t} = \boldsymbol{\nabla} \cdot \left[M(\phi, \mathbf{r}, t) \boldsymbol{\nabla} \frac{\delta F}{\delta \phi} \right] + p(\phi, \partial_i u_i) \,, \tag{6.30}$$

where $p(\phi, \partial_i u_i)$ is a non-local function that models the proliferation of endothelial stalk cells. The presence of this function in the CH equation does not allow us to write the equation as a conservation law, meaning that the total value of ϕ in the domain will not be constant and will increase with time, since by definition $p(\phi, \partial_i u_i) > 0$. In this work we will consider the case where $M(\phi, \mathbf{r}, t)$ is constant at every point and does not change in time, so that equation 6.30 can be simplified to

$$\frac{\partial \phi}{\partial t} = M \nabla^2 \frac{\delta F}{\delta \phi} + p(\phi, \partial_i u_i) \,. \tag{6.31}$$

Numerical Solution

To solve equation 6.31, our only solution is to resort to numerical methods since an analytical solution for such a complex model does not exist. To obtain the finite difference scheme used to obtain the numerical solution we split the terms in equation 6.31 in four different terms:

$$\frac{\partial \phi}{\partial t} = -M \rho_\phi \epsilon^2 \nabla^4 \phi + M \nabla^2 f_A + M f_B + p \,. \tag{6.32}$$

The first term comes from applying the Laplacian operator to the interface energy that already contained $\nabla^2\phi$. Then we divide the rest of the free energy functional derivative into f_A where we include all the terms that are not under the inverse Laplacian, while in f_B we include those terms where the inverse Laplacian is canceled by the Laplacian coming from the Model B equation. Lastly we keep the proliferation term as is. Applying a Fourier Transform to the previous equation we are left with

$$\frac{\partial\hat{\phi}(\mathbf{k})}{\partial t} = -M\rho_\phi\epsilon^2|\mathbf{k}|^4\hat{\phi}(\mathbf{k}) - |\mathbf{k}|^2 M\hat{f}_A(\mathbf{k}) + M\hat{f}_B(\mathbf{k}) + \hat{p}(\mathbf{k})\,. \tag{6.33}$$

The term containing $\nabla^4\phi$ is the most challenging to treat numerically. Since it leads to a term, in reciprocal space, proportional to $|\mathbf{k}|^4$, it can amplify numerical errors especially at high frequencies. To stabilize the behavior of this term during calculations, we use a semi-implicit time discretization where that term is treated implicitly and the rest of the terms are used in their explicit form. By using a Forward Time scheme for the time derivative, we arrive at the discretization of equation 6.32:

$$\begin{aligned}
&\frac{\hat{\phi}^{t+1}(\mathbf{k}) - \hat{\phi}^t(\mathbf{k})}{\Delta t} = -M\rho_\phi\epsilon^2|\mathbf{k}|^4\hat{\phi}^{t+1}(\mathbf{k}) - M|\mathbf{k}|^2\hat{f}_A^t(\mathbf{k}) + M\hat{f}_B^t(\mathbf{k}) + \hat{p}^t(\mathbf{k}) \\
&\Leftrightarrow \hat{\phi}^{t+1}(\mathbf{k}) = \frac{\hat{\phi}^t(\mathbf{k}) - \Delta tM|\mathbf{k}|^2\hat{f}_A^t(\mathbf{k}) + \Delta tM\hat{f}_B^t(\mathbf{k}) + \Delta t\hat{p}^t(\mathbf{k})}{1 + \Delta tM\rho_\phi\epsilon^2|\mathbf{k}|^4}
\end{aligned} \tag{6.34}$$

In general, f_A, f_B and p are nonlinear functions, and as such we apply a semi-spectral approach for their calculation. The terms containing derivatives of linear terms can be calculated directly in Fourier space. For the nonlinear terms, we do the calculation in real space using finite differences and then transform the result to $\mathbf{k}$-space.

6.4.5 VEGF Dynamics

To consider the effect of chemotaxis on the movement of tip cells and, consequently, on the formation of new vessels, we model the existence of a VEGF field in the system. In this work, we consider only one type of diffusible VEGF, although in other works the existence of different isoforms of VEGF (diffusible and non-diffusible) has been considered [29, 106]. The dynamics of endothelial growth factor is modeled using a diffusion equation

$$\frac{\partial V}{\partial t} = D_V\nabla^2 V - K_V(\phi)V\,, \tag{6.35}$$

where D_V is the diffusion rate of VEGF and $K_V(\phi)$ is the rate of consumption of the protein by endothelial cells, which depends on ϕ. As such, the consumption rate of VEGF is given by

$$K_V(\phi) = k_v\frac{h(\phi)+1}{2}\mathcal{H}(\phi)\,, \tag{6.36}$$

where k_v is the constant rate of consumption of VEGF by endothelial cells and $\mathcal{H}(h(\phi))$ is the Heaviside step function, that guarantees that the VEGF sink term is only non-zero in regions with endothelial cells.

We can estimate the diffusion distance of VEGF as a function of the parameters D_V and k_V by finding the stationary state of a one dimensional version of equation 6.35. This equation is

$$D_V \frac{\mathrm{d}^2 V}{\mathrm{d}x^2} - k_V V = 0\,. \tag{6.37}$$

The solution to this equation that has physical significance is

$$V(x) = V_0 \exp\left(-\frac{x}{\lambda_V}\right), \tag{6.38}$$

where

$$\lambda_V = \sqrt{\frac{D_V}{k_V}}\,. \tag{6.39}$$

Since the argument of the exponential function must be dimensionless, λ_V has units of distance. Physically, λ_V represents the average diffusion distance of VEGF.

Equation 6.35 is solved numerically using a semi-implicit spectral method with periodic boundary conditions. Applying a Fourier transform to the equation we get

$$\frac{\partial \hat{V}(\mathbf{k})}{\partial t} = -D_V |\mathbf{k}|^2 \hat{V}(\mathbf{k}) - \mathcal{F}\left\{K_V(\phi)V\right\}(\mathbf{k})\,. \tag{6.40}$$

Applying backward finite differences in time on the linear terms and explicit discretization on the non linear consumption term, we get

$$\frac{\hat{V}^{t+1}(\mathbf{k}) - \hat{V}^{t}(\mathbf{k})}{\Delta t} = -D_V |\mathbf{k}|^2 \hat{V}^{t+1}(\mathbf{k}) - \mathcal{F}\left\{K_V(\phi)V^t\right\}(\mathbf{k}) \tag{6.41}$$

Rearranging the terms we get

$$\hat{V}^{t+1}(\mathbf{k}) = \frac{\hat{V}^{t}(\mathbf{k}) - \Delta t \mathcal{F}\left\{K_V(\phi)V^t\right\}(\mathbf{k})}{1 + D_V \Delta t |\mathbf{k}|^2}\,. \tag{6.42}$$

By using a semi implicit discretization, we can use larger values for the timestep Δt, which, when using a fully explicit method like Forward Time Centered Space (FTCS) is limited by the Courant-Friedrichs-Lewy constraint resulting from the discretization of the Laplacian operator.

6.4.6 Tip Cell Force

The traction force field applied by an endothelial cell on a substrate has been studied by several authors using techniques like Traction Force Microscopy. Lemmon and Romer created a predictive model of this force based on experimental measurements where they observed that the traction force exerted by a cell points towards its center and its intensity increases linearly with the distance between the points where the force is calculated and the cell center [110]. The Lemmon-Romer model for the traction force has been adopted by other authors who have developed computational models of cell migration [111][104][112].

Here we assume that each tip cell is represented by the portion of the computational domain bounded by an ellipsoid centered at the interface between the endothelial tissue and the ECM. The traction force $\boldsymbol{F}_{\text{tip}}$ at each point inside the ellipsoidal region Ω_{tip} is given by

$$\boldsymbol{F}_{\text{tip}} = \begin{cases} F_0 \frac{\boldsymbol{r}_{\text{tip}} - \boldsymbol{r}}{R_{\max}}, & \boldsymbol{r} \in \Omega_{\text{tip}} \\ 0, & \boldsymbol{r} \notin \Omega_{\text{tip}}\,, \end{cases} \tag{6.43}$$

where $\boldsymbol{r}_{\text{tip}}$ and $\boldsymbol{r}$ are, respectively, the position of the ellipsoid's center and the position of the point of the domain where the force is calculated. $R_{\max}$ is the length of the major semiaxis of the ellipsoid such that the magnitude of the traction force lies between 0 (when $\boldsymbol{r} = \boldsymbol{r}_{\text{tip}}$) and F_0 (when $\|\boldsymbol{r} - \boldsymbol{r}_{\text{tip}}\| = R_{\max}$). The expression for the tip cell force in 6.43 follows the Lemmon-Romer model for its magnitude increases linearly with the distance to the center of the cell and points towards it. The domain Ω_{tip} is defined by

$$\left(\frac{x_{\text{tip}} - x}{R_x}\right)^2 + \left(\frac{y_{\text{tip}} - y}{R_y}\right)^2 + \left(\frac{z_{\text{tip}} - z}{R_z}\right)^2 < 1 \tag{6.44}$$

in the 3D model while in the 2D case we assume $z_{\text{tip}} = z$.

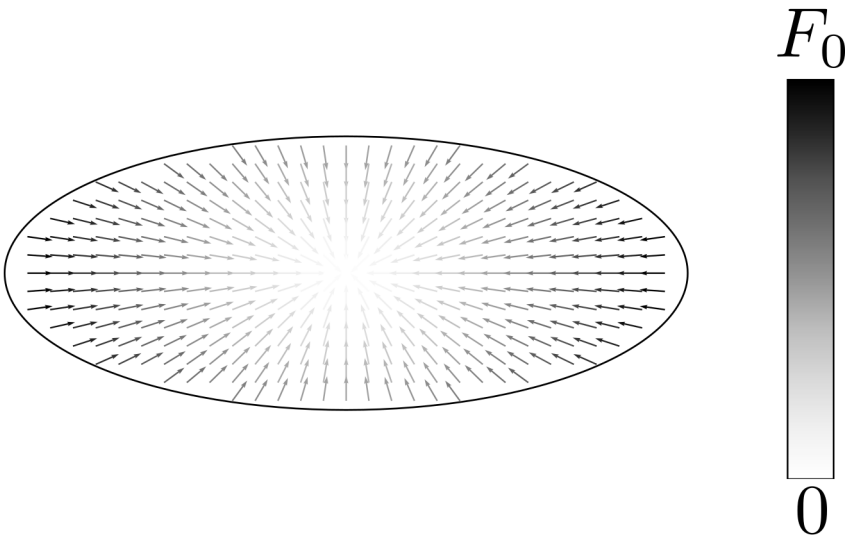

FIGURE 6.3: Tip cell traction force vector field. The tip cell boundary is denoted by the black line and the direction of the force is indicated by the arrows. The grayscale of the arrows indicates the intensity of the force at that point.

Since we want to simulate the chemotactic response of the tip cells to the vascular growth factor, the applied traction force must be aligned with the gradient of VEGF. This means that we must redefine Ω_{tip} to account for ellipsoids with a major axis that is not aligned with the reference frame of the computational domain. This operation is trivial in the two dimensional case: Let $\hat{v} = v_x\hat{e}_x + v_y\hat{e}_y$ be the unit vector that points in the direction of

the VEGF gradient. We can relate the components of $\hat{v}$ with the rotation angle θ

$$v_x = \cos\theta$$
$$v_y = \sin\theta$$

and assemble the rotation matrix that transforms the vector coordinates from the domain's reference frame to the frame where the major axis of the ellipse is aligned with $\hat{v}$

$$R = \begin{pmatrix} \cos\theta & \sin\theta \\ -\sin\theta & \cos\theta \end{pmatrix} . \tag{6.45}$$

Defining $\Delta x = x_{\text{tip}} - x$ and $\Delta y = y_{\text{tip}} - y$, we can write the equation that defines the rotated ellipse using

$$\begin{pmatrix} \Delta x' \\ \Delta y' \end{pmatrix} = R \begin{pmatrix} \Delta x \\ \Delta y \end{pmatrix} ,$$

i.e.

$$\left(\frac{\Delta x'}{R_x}\right)^2 + \left(\frac{\Delta y'}{R_y}\right)^2 < 1 . \tag{6.46}$$

Using this expression we can check if a points is inside the rotated ellipse aligned with the desired direction of migration.

In three dimensions, the process of finding the equation for the rotated ellipsoid is more complex. To perform the rotation we make use of the Rodrigues formula for 3D rotations (derived in Chapter 2). Like in the 2D case we wish to find the transformation that aligns an ellipsoid's major axis with the direction of increasing VEGF concentration. Suppose $\hat{p}$ represents the orientation of the ellipsoid's major axis and $\hat{v}$ is the unit vector in the direction of the VEGF gradient. To define the rotation we need to provide an axis around which the rotation will happen, as well as an angle. In this case the obvious choice for rotation axis is a vector that is perpendicular to both $\hat{p}$ and $\hat{v}$ i.e.

$$\boldsymbol{\omega} = \hat{p} \times \hat{v} \tag{6.47}$$

To get the angle of rotation we use the relation between the dot and cross product of two vectors and, respectively, the cosine and sine of that angle

$$\begin{aligned} \sin\theta &= |\hat{p} \times \hat{v}| = |\boldsymbol{\omega}| \\ \cos\theta &= |\hat{p} \cdot \hat{v}| , \end{aligned} \tag{6.48}$$

which can be used in the Rodrigues formula, along with the skew-symmetric matrix $N(\hat{\omega})$ to obtain the rotation matrix

$$R = I + \sin\theta \; N(\hat{\omega}) + (1 - \cos\theta) N^2(\hat{\omega}) . \tag{6.49}$$

6.4.7 Stalk Cell Proliferation

Although in this model we use a conservative phase field model B dynamics, we wish to model endothelial cell proliferation. To this end, we introduce the term $p(\phi, \mathbf{u}, V)$ as a source term in the Cahn-Hilliard equation. In [108], the dependence of sprout elongation on the model chosen for the function $p(\phi, \mathbf{u}, V)$ was studied in great detail. In that study, it was shown that, in order to better replicate the results obtained from experiments, proliferation must be a function of the concentration of VEGF but its occurence is limited to regions where the endothelial tissue is being stretched. Since the focus of this work is on the influence of mechanical properties of the tissue and not on how to model stalk cell proliferation, we will model the proliferation term as in [108].

To calculate the proliferation term, we suppose that every point in space that belongs to the endothelial tissue ($\phi \approx +1$) is the center of a round cell with a certain radius, r_{prol}. Inside that region we calculate

$$p(\phi, \mathbf{u}, V) = \frac{1}{\int \mathcal{H}(h(\phi))\,\mathrm{d}\mathbf{r}} \int \mathcal{P}(V)\mathcal{H}(h(\phi))\mathcal{H}\left(L_0 \boldsymbol{\nabla} \cdot \mathbf{u} + \alpha\right)\mathrm{d}\mathbf{r}\ . \tag{6.50}$$

The calculation of p can be interpreted as the integral of $\mathcal{P}(V)$ calculated inside the area of the cell centered at a certain point, normalized to the number of points in that same area where $h(\phi) > 0$. The presence of the term $\mathcal{H}\left(L_0 \boldsymbol{\nabla} \cdot \mathbf{u} + \alpha\right)$ serves to restrict the contribution to the integral of points that are being stretched i.e., it only counts points where $\boldsymbol{\nabla} \cdot \mathbf{u} = \mathrm{tr}(\varepsilon) > -\alpha/L_0$, where $-\alpha/L_0$ is the value of $\boldsymbol{\nabla} \cdot \mathbf{u}$ of the relaxed endothelial tissue, where there is no traction force being applied. Typically this means that the only zones that will be able to proliferate are the ones directly behind an active tip cell, where the tissue is being deformed the most.

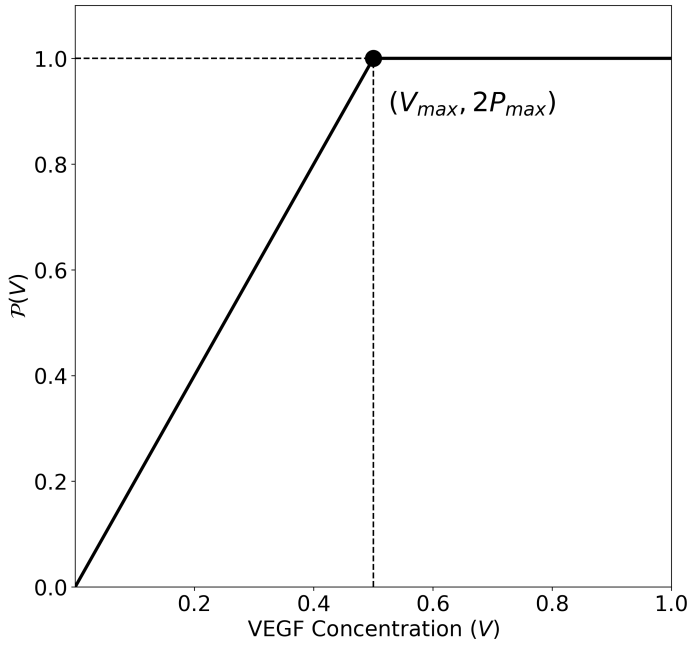

FIGURE 6.4: Graphical representation of $\mathcal{P}(V)$. The point where the value of $\mathcal{P}$ saturates to a constant value, $2P_{\max}$ is highlighted. For this representation, $V_{\max} = P_{\max} = 0.5$

The dependence of the proliferative term on the amount of VEGF in the tissue is included in the function $\mathcal{P}(V)$. This function includes two conditions to the value of proliferation at each point: first, the amount of proliferation depends linearly on the concentration of VEGF at that point, until a certain level of concentration $V_{\max}$ is reached, where the proliferation reaches a maximum, constant value, $P_{\max}$. The expression for $\mathcal{P}(V)$ is given by

$$\mathcal{P}(V) = \begin{cases} \frac{2P_{\max}V}{V_{\max}} & V < V_{\max} \\ 2P_{\max} & V > V_{\max} \end{cases} \tag{6.51}$$

as represented in Figure 6.4.

6.4.8 Notch Mechanism

The role of the Delta-Notch signaling pathway is essential in the formation of vessel networks and as such, to obtain a realistic computational model of angiogenesis, this mechanism and its consequences must be considered.

As described in the previous sections, tip cells are modeled as traction force fields centered at the interface, bounded by an ellipse (ellipsoid in 3D). Consequently, before adding a new tip cell, the set of all points in the grid that are at the interface is determined. In order to do that we first convert the order parameter from a continuous representation to a discrete binary map, where

$$\phi_{\text{bin}}(x,y,z) = \begin{cases} 1 & h(\phi(x,y,z)) > 0 \\ 0 & h(\phi(x,y,z)) \leq 0 \end{cases} . \tag{6.52}$$

Afterwards, to determine if a point belongs to the boundary, we calculate the sum of ϕ_{bin} over the neighborhood, $\mathcal{N}$, of that same point, given by

$$s(x,y,z) = \sum_{\mathcal{N}} \phi_{\text{bin}}(x,y,z)$$

where the neighborhood considered can include first and second neighbors called, respectively, the Von Neumann or Moore neighborhood. In the case where the simpler Von Neumann neighborhood is considered, a point is counted as a part of the boundary if $\phi_{\text{bin}}(x,y,z) = 1$ and if $s(x,y,z) \neq n(\mathcal{N})$, where $n(\mathcal{N})$ is the cardinality, or, number of elements set $\mathcal{N}$. In two dimensions, the cardinality of the set containing all points in the Von Neumann neighborhood is equal to 4, while in three dimensional systems it is equal to 6.

Let $\mathcal{B}$ be the set of all points that are a part of the interface between the endothelial tissue and the ECM. Also, let $d(b_1, b_2)$ be a function that for any two elements of $\mathcal{B}$, b_1 and b_2 returns the Euclidean distance d between b_1 and b_2. At a certain point in time, a tip cell can be added to the system at point $t_{\text{new}} \in \mathcal{B}$ if for each position t_i of every tip cell

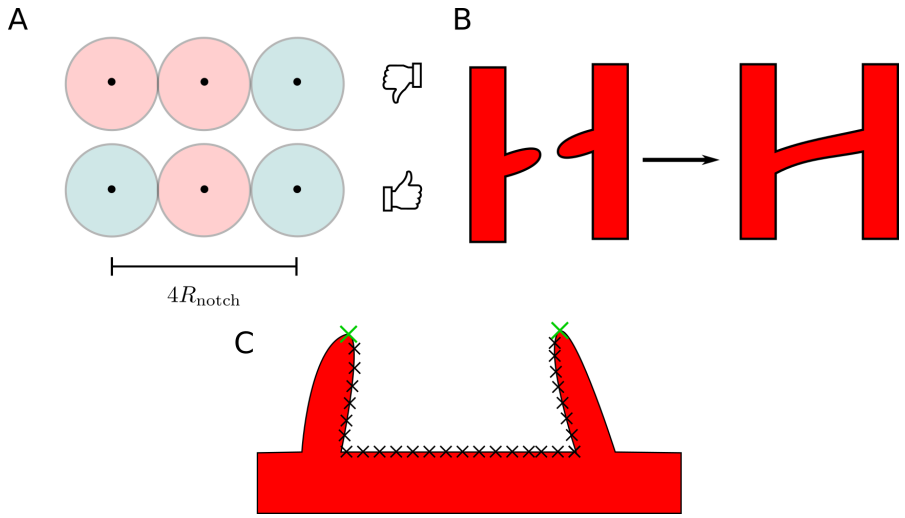

FIGURE 6.5: Example of tip (red) and stalk (blue) patterns that are and are not allowed, considering the Delta-Notch mechanism (A). Two tip cells can be close if they belong to different clusters , and can form anastomosis (B). Graphical representation of the distance between two tip cells (green crosses) is calculated along the vessel interface (C).

currently in the simulation, the condition

$$d(t_i, t_{\text{new}}) > 4R_{\text{notch}} \tag{6.53}$$

is verified. R_{notch} defines the minimum distance between two cells, that allows them to both have a tip cell phenotype. The distance of $4R_{\text{notch}}$ means that for two cells, aligned on an axis, to be tip cells, there must be at least one other cell between them, as depicted in Figure 6.5A.

The Delta-Notch pathway not only controls the appearance of new tip cells, but it is also responsible for reversing the tip cell phenotype if two tip cells get too close to each other. In this model, the method for removing a tip cell from the system is more complex than the one for adding new tip cells, as described above. The difference stems from the fact that Delta-Notch signaling is contact-dependent. This means that if two tip cells are very close to each other, but they do not belong to the same endothelial cell cluster, they can both maintain their phenotype. However, if two sprouts meet in space and form a connection (Figure 6.5B) called an anastomosis, one of the tip cell leaders of those two sprouts must be removed.

Determining the distance between two tip cells located at $\mathbf{t_1}$ and $\mathbf{t_2}$ (green crosses in Figure 6.5C, while at the same time checking if the two cells belong to the same cluster, means finding a path between the two positions that only contains points that belong to $\mathcal{B}$. If $l_{\text{path}} < 4R_{\text{notch}}$, where l_{path} is the length of the shortest path found, one of the tip cells must revert its phenotype to stalk cell. To find the shortest path, we describe the interface of the system as a graph, where each node corresponds to a point that belongs to $\mathcal{B}$. An edge connects two nodes if they are adjacent and its value is equal to one (considering a Von Neumann neighborhood). We define a map $\delta(\mathbf{p})$ where to each node, $\mathbf{p}$ we assign the distance to one of the tip cells, measured along the interface. Performing a Breadth First

Search on the graph is an iterative process where we start from one of the tip cell nodes and set $\delta(\mathbf{t_1}) = 0$, while all other nodes have a value of $\delta(\mathbf{p}) = \infty$ (in practice, a very large number). Then, starting from $\mathbf{t_1}$ we process its neighbors and their value of δ in the next iteration will be

$$\delta(\mathbf{p})^{t+1} = \min\left(\delta(\mathbf{p})^t, \delta(\mathbf{t_1})^t + 1\right) . \tag{6.54}$$

In the next step, all the nodes visited in the previous one will be analyzed, and after some iterations, the value of $\delta(\mathbf{t_2})$ will be the distance of tip cell $\mathbf{t_1}$ to tip cell at $\mathbf{t_2}$ i.e. l_{path}. If $l_{\text{path}} < 4R_{\text{notch}}$, either $\mathbf{t_1}$ or $\mathbf{t_2}$ must loose its tip cell phenotype. In this work, one of the two is randomly selected for removal.

6.5 Results and Discussion

6.5.1 Single Tip Cell Migration

Before simulating very complex systems with many sprouting events, it is appropriate to look at how the migration of a single tip cell is dependent on the mechanical properties of the ECM and on the intensity of the traction force the cell exerts on the matrix. To this end we simulate a single tip cell that sprouts from an initial and stable vessel, located on the left side of the domain, and migrates in the direction of the VEGF gradient that, in this case, points from left to right, perpendicularly to the vessel. The simulations are ran for the same number of timesteps, $N_t = 2 \times 10^4$, in a rectangular box of dimensions Lx $\times$ Ly $= 64 \times 512$, where an initial vessel of width $w = 30$ μm. In this simulation we assume there is no stalk cell proliferation, so that we can focus on the effects of the different mechanical properties of the ECM on the result. The adhesion force parameter is set to $\alpha = 470$ Pa and the bulk modulus is set such that it is the same in both phases ($K_1 = 0$). The only tip cell in the system is placed in the middle of the main vessel at $(x, y) = (w, {}^{Ly}/_2)$. In Figure 6.6, we show the results of simulating a single sprouting event and where the vessel structure and length can be seen when we vary the ECM rigidity and the maximum value of the traction force exerted by the tip cell on the surrounding tissue. The ECM rigidity varies column-wise, increasing from left to right, from 90 to 180 Pa while the traction forces increases from 47 to 70 Pa, top to bottom, row-wise. From Figure 6.6 we can directly see that for different combinations of ECM rigidity and tip cell traction force values, there are two things that can happen: either there is the formation of a sprout that extends reaching a certain length or the tip cell, instead of forming a sprout, breaks away from the main vessel and migrates alone in the direction of the VEGF gradient.

In the case where the ECM has low rigidity, even for low values of tip cell traction force, the matrix is easily deformed, facilitating the movement of the tip cell in the direction of the VEGF gradient. Depending on the value of cell-cell adhesion, this can lead to the movement of stalk cells not being able to keep up with the tip cell. When this happens, the tip cell will break free from the neighboring tissue and migrate individually. As we increase μ_{ECM}, the tip cell can still deform the matrix, but now the adhesion force is

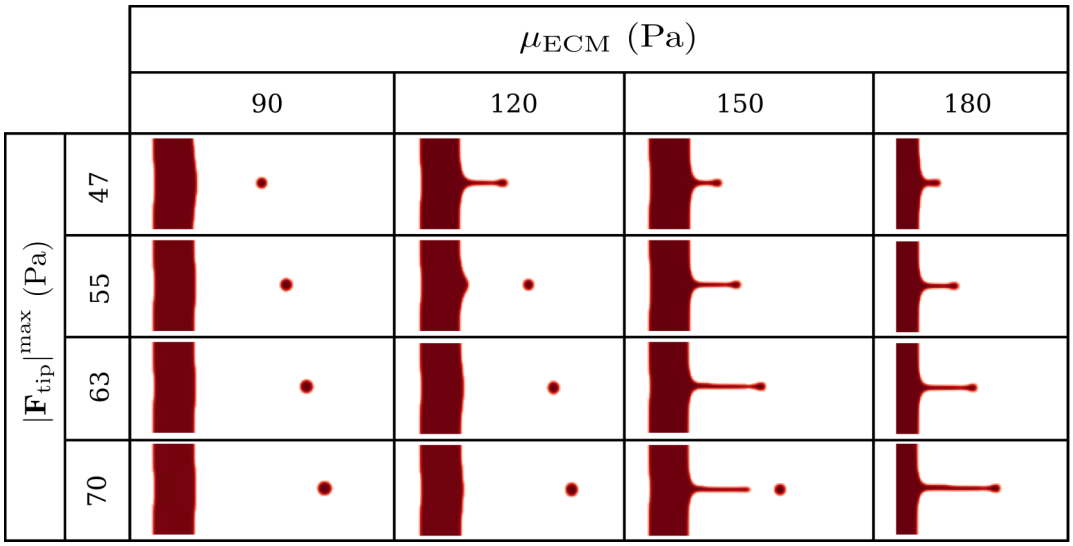

FIGURE 6.6: Dependence of vessel length and structure for different values of ECM rigidity, μ_{ecm}, and the maximum value of tip cell traction force, $|\mathbf{F}_{\mathrm{tip}}|$. The red zones correspond to regions where $\phi \approx 1$ (endothelial tissue) and in the white background we have $\phi \approx -1$ (ECM).

capable of maintaining the integrity of the sprout and there is a formation of longer vessel that extends towards VEGF sources.

These simulations using a single tip cell also serve to explain how the dynamics of the order parameter depends on the rigidity of the ECM and on the tip cell force. When a cell exerts a traction force, there is a deformation of the surrounding tissue. In order to minimize the free energy, the system's overall driving force, $\mathbf{J} = -\boldsymbol{\nabla}\frac{\delta F}{\delta \phi}$, will direct the movement of endothelial cells ($\phi \approx +1$) towards regions where the ECM has the highest strain. Since the rigidity of the ECM is always higher than the rigidity of the vascular tissue i.e., $\mu_1 > 0$, this will lead to the endothelial cells to occupy the surrounding tissue that is being stretched due to the tip cell traction force. At the same time, this traction force is compressing the endothelial cells located just behind the tip cell, raising its energy, also favouring the movement of those cells to distended areas of the ECM. This compression generated on the stalk cells leads to an accumulation of order parameter in that region, such that its value in those zones can be slightly larger than one.

6.5.2 One Spheroid

In order to assess the model's ability to reproduce the experimental observations from the aortic ring assays, we simulate a system that starts from a two dimensional spheroid represented by a circle with a radius of R_{sph}, where the order parameter has an initial value of $\phi = 1$ (and $\phi = -1$ outside the circle). This system is more complex than the one used on the single tip cell simulations. Here we consider there is stalk cell proliferation and Delta-Notch derived rules are used for the appearance and removal of tip cells. In Figure 6.7, we can see networks of vessels, for different values of tip cell traction force and ECM rigidity. The presence of isolated, migrating tip cells when the ECM rigidity is lower is easily seen and expected, considering the results obtained for the same range of rigidity

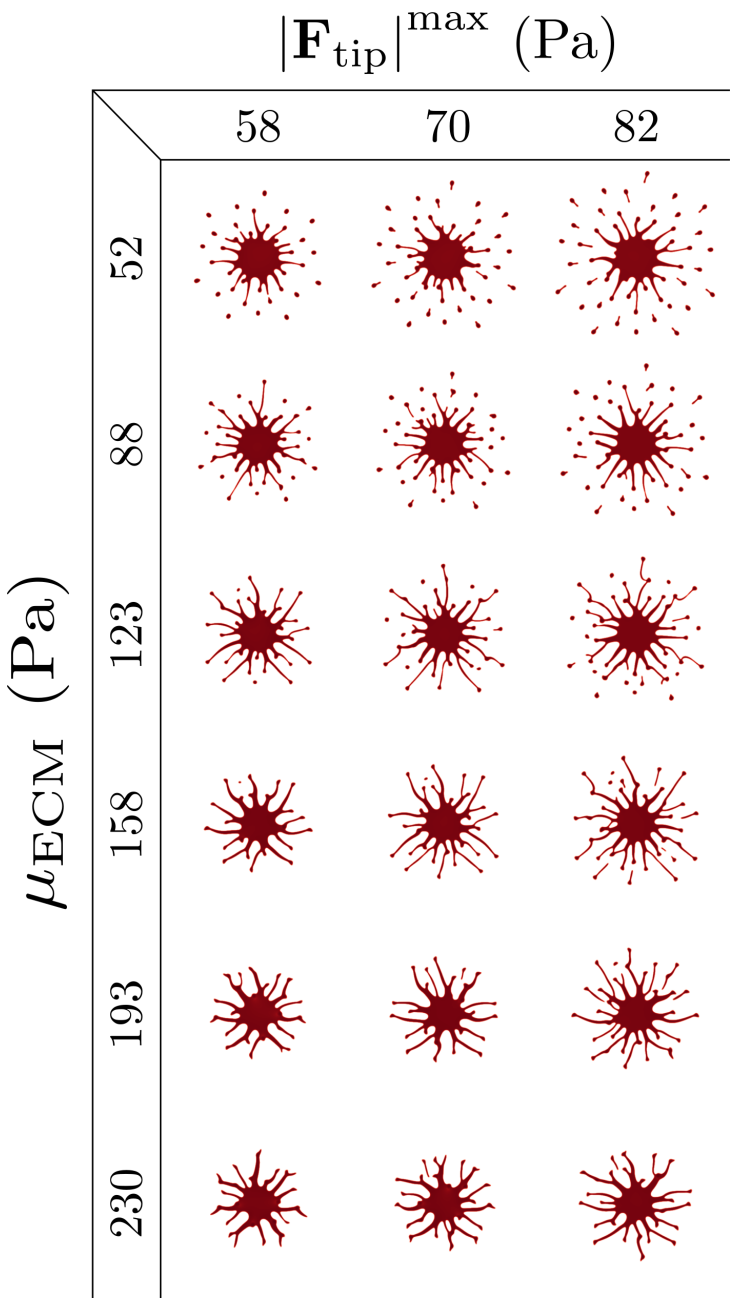

FIGURE 6.7: Dependence of vessel length and structure for different values of ECM rigidity, μ_{ecm}, and the maximum value of tip cell traction force, $|\mathbf{F}_{\text{tip}}|^{\text{max}}$. The red zones correspond to regions where $\phi \approx 1$ (endothelial tissue) and in the white background we have $\phi \approx -1$ (ECM).

used in the previous section. When $\mu_{\text{ECM}} = 52$ Pa, the sprout formations we see are very short and there is an abundance of tip cells that break free from the spheroid cluster. As we increase the value of the tip cell traction force, in the same time interval, those tip cells migrate further, resulting in a more dispersed network. As we increase the stiffness of the ECM, we see a drop in the number of loose tip cells and we start seeing more elongated sprouts that maintain their connection to the spheroid although some cells are still able to break away from the sprouts, mainly for higher values of tip cell traction force. The length of the vessels starts increasing with rigidity and, at a μ_{ECM} value dependent on the value of the cells' traction force, they reach their maximum length. For higher rigidities,

the vessel network starts getting more compact, showing vessels of shorter length.

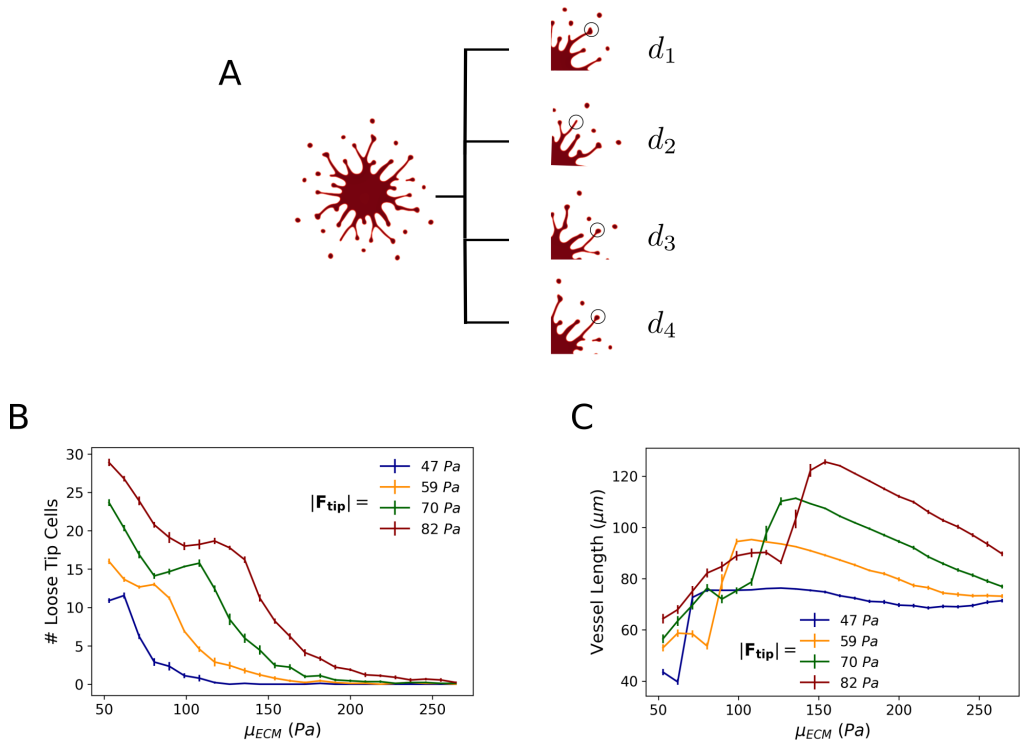

FIGURE 6.8: Vessel length measurement procedure. From each quadrant of the image, the distance of the tip cell that migrated the most, while still attached to the spheroid, (surrounded by a black circle) is extracted, yielding a set of 4 distances, $\{d_1, d_2, d_3, d_4\}$ (A). Number of tip cells that break away from the spheroid (B) and vessel length (C) as a function of ECM rigidity for different values of maximum tip cell traction force.

In order to provide a quantitative analysis of the results obtained from the simulations in the images presented in Figure 6.7, image analysis was performed on the vessel networks. The methods used to analyze the computational results were tailored to be as close as possible to the ones used in analyzing the microscopy images obtained from the aortic ring assay. In Figure 6.8A is illustrated how, from each image, we extract four values for the vessel length, measured only for vessels that are connected to the main spheroid. For each quadrant we determine which tip cell traveled the furthest and store the set of measurements. The same system with the same parameters is simulated for N_{seeds} different seeds of the random number generator, that determine the choice of the tip cell position, in the end we perform an average of the $4N_{\text{seeds}}$ values of vessel lengths and calculate the standard deviation of the mean.

In Figure 6.8B we see how the number of tip cells that break away from the main spheroid varies for matrices of different rigidities. As expected, for very soft ECMs, the number of tip cells migrating individually is high since the matrix is very compliant and easily deformed, prompting the movement of the compressed tissue to move to those areas. For the value of adhesion α, surface tension ρ_ϕ and stalk cell proliferation used in the simulations, it is very likely for the tip cell to detach from the trailing cells. As expected, the higher the tip cell traction force, the higher the number of detached cells. As we increase the rigidity of the

matrix, the tip cells are not able to deform the surrounding matrix as much and we see the formation of some sprouts, marked by the increase in vessel length represented in Figure 6.8C. As the number of isolated tip cells diminishes, the length of the sprouts increases as we look into increasingly more rigid ECMs. The most striking result observed in Figure 6.8C is that for each traction force amplitude, there is a value of rigidity for which the length of the sprouts reaches a maximum value. For lower values of $|\mathbf{F}_{\text{tip}}|^{\text{max}}$, the μ_{ECM} value that maximizes the sprout length is also lower. When $|\mathbf{F}_{\text{tip}}|^{\text{max}} = 47$ Pa, sprout length is highest for an ECM rigidity of $\mu_{\text{ECM}} \approx 75$ Pa while for $|\mathbf{F}_{\text{tip}}|^{\text{max}} = 82$ Pa, the maximum is located at $\mu_{\text{ECM}} = 150$ Pa. This suggests that what determines the maximum vessel length is a balance between the tip cell traction force and the ECM rigidity. When cells exert small forces, they are not able to sufficiently deform the ECM in a way that allows the vessel to elongate significantly. For higher traction forces, sprouts can elongate further and for more rigid matrices, until a certain rigidity is reached, where the vessels start getting shorter.

6.5.3 Aortic Ring

In this section we present the results for simulations where the initial condition resembles an aortic ring as the ones used in the experimental work. The initial condition is a ring with an inner radius of $r_{\text{in}} = 150$ μm and an outer radius of $r_{\text{out}} = 225$ μm. Although, in experiments (Figure 6.1), we can see there is some sprouting activity on the inside part of the aorta, those sprouts are not taken into consideration when measuring cell migration and vessel length. As such, in the simulation, there is VEGF only on the outside of the modeled aortic ring, so that there is no sprouting activity in the inner circle. In Figure 6.9A can see the result of a simulation of the system described above for a very soft ECM with a rigidity of $\mu_{\text{ECM}} = 80$ Pa. As seen in the results from the spheroid simulations, most of the tip cells are detached from the aortic ring, migrating individually with only a few longer sprouts seen very close to the aorta. For medium rigidity matrices where $\mu_{\text{ECM}} = 172$ Pa, the network shows fewer cells migrating individually and there are longer sprouts, some of them with ramifications. In Figure 6.9C and D we see the network for a stiffer matrix ($\mu_{\text{ECM}} = 265$ Pa). For this rigidity, there are barely any cells migrating alone and more complex vascular structures can be observed. Figure 6.9D shows the amplification of the region marked in yellow in Figure 6.9C, where we can see some of these vascular structures in more detail. One of the most important features of this model is the most apparent when looking at the closed loops of vessels seen in that amplified region. These loops are the result of anastomosis events between two or more sprouts that meet in space. This phenomenon can be explained using only the principles that drive the dynamics of the order parameter when tip cell traction forces and the resulting displacement field are taken into account. As previously mentioned, tip cell forces create a deformation on the ECM, lowering the energy of the tissue and in order to minimize the global energy, tip cells tend to migrate to those regions. When two or more tip cells are close to one another, in a way that does not lead to a phenotypic change due to the Delta-Notch mechanism, they all deform the same neighboring tissue. This results in certain areas of the tissue to be highly

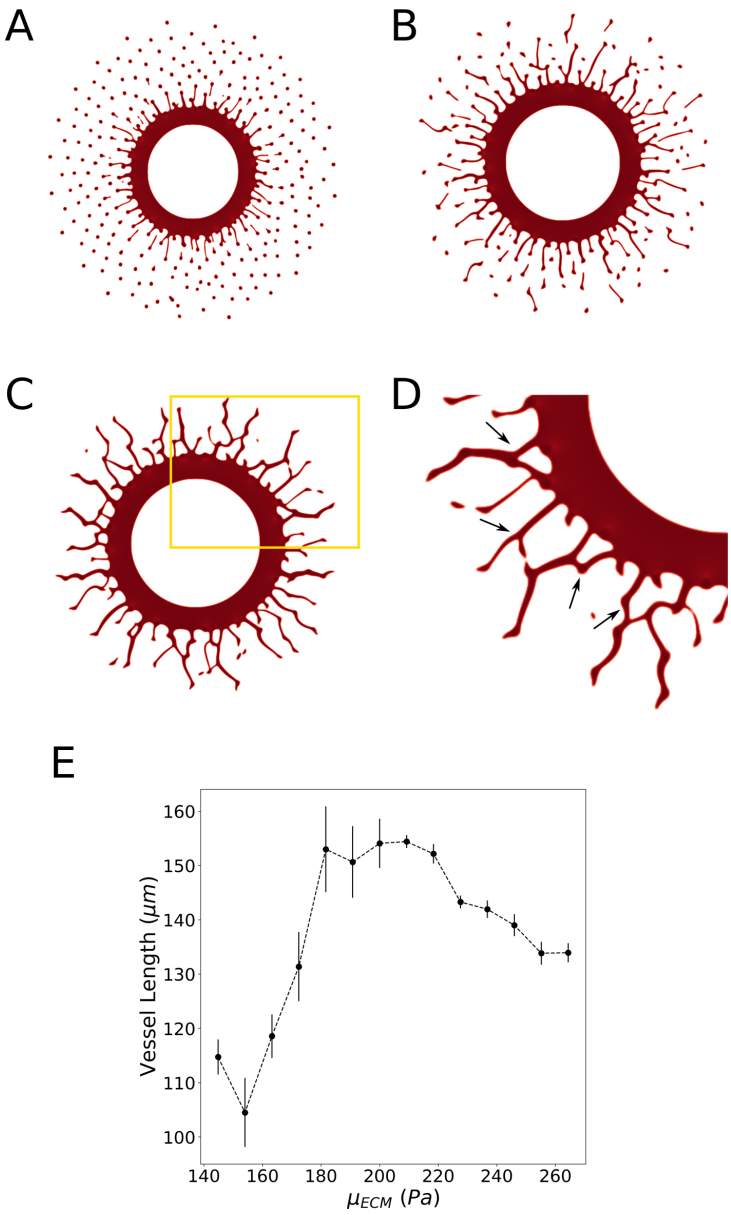

FIGURE 6.9: Results obtained from simulations of sprouting angiogenesis in aorta rings, for matrices of different rigidity (80 (A), 172 (B) and 265 Pa (C)). In (D) we can an amplification of the region delimited by the yellow lines in (C) with arrows pointing to the regions where anastomoses were formed. Vessel length as a function of ECM rigidity (E).

favorable for the tip cells to move there, leading to the fusion of between them, which is also favored by the fact that it reduces the amount of interface in the system. When they fuse, tip cells are now in contact, and the Notch mechanism will ensure only one tip cell remains, thus these loop structures are formed. In Figure 6.9E we show the vessel length as a function of ECM rigidity, μ_{ECM} for a maximum tip cell force of 70 Pa. As seen in the previous section, vessel length depends on ECM rigidity in a non-monotonic way which is compatible with the same measurement made experimentally.

6.5.4 Sprouting in Three Dimensions

In three dimensions, we can observe how endothelial cell sprouting depends on the rigidity of the ECM for more complex initial structures. In the first row of Figure 6.10 we show

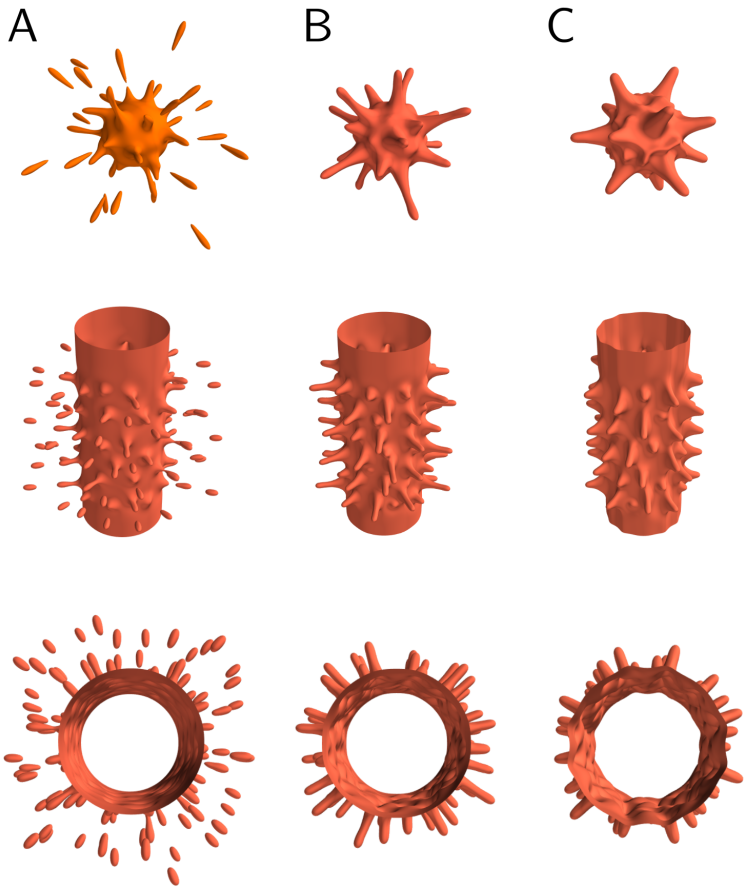

FIGURE 6.10: Sprout formation in three dimensions for different ECM rigidities and endothelial cell distributions: spheroid (top) and for a tubular geometry (middle and bottom, top view). ECM rigidity increases from left to right: 52 Pa (A), 145 Pa (B) and 240 Pa (C)

how sprouting occurs when it starts from a 3D spheroid, a natural extension of the results shown in Figure 6.7. For low values of ECM rigidity (column A) we see that there is little sprout formation, since most tip cells break away from the initial spheroid. The same is observed for the system that starts from a tubular structure, which means that the difficulty in forming elongated sprouts is independent of the initial geometry and is related with the properties of the ECM. For higher rigidities (columns B and C) we see some sprout elongation, and it is noticeable that sprout length is higher for intermediate rigidities, starting to decrease for stiff ECMs. The differences in sprout length is clearer when we look at the results for the tubular geometry from a top view. For soft matrices, there is increased cell migration, but with no sprout formation, since all cells break away from the initial vessel. As we increase μ_{ecm}, there is sprout formation that become shorter for more rigid ECMs.

6.6 Conclusions and Future Work

In this chapter we showed how the formation of neovascular through sprouting angiogenesis is dependent on the forces generated by endothelial cells, but most importantly, on the stiffness of the ECM that surrounds the active endothelial tissue. For a fixed value of tip cell traction force, we can see that sprout length has a non linear dependence on the value of ECM rigidity. Soft matrices are easily deformed, which creates a displacement field that promotes tip cell movement. For a certain value of cell-cell adhesion, stalk cells are not capable of following the tip cell, which looses the structure that connects it to the initial vessel and breaks away, migrating alone. As we increase μ_{ecm}, the matrix becomes more rigid, less prone to deformation and tip cell migration slows down, now allowing for stalk cells to follow, forming elongated sprouts. Strikingly, we observe that there is a certain value for μ_{ecm} that leads to a maximum value of sprout elongation. This result is validated by experimental observations, where this non monotonic variation of vessel length with ECM rigidity is also verified. For matrices that are very rigid, sprout length shortens, due to the difficulty for the tip cell to deform the matrix.

When we simulate systems where there is increased sprouting activity, as in an aortic ring assay, we see the formation of more complex vessel networks and the joining of two or more branches which creates a loop. The observation of tip cell-tip cell anastomoses is a result of considering the system as an elastic medium and the displacement field created by the tip cells. As such, it arises naturally from modeling choices, instead of it being a programmed behavior.

The model presented in this chapter can still be improved to simulate more realistic settings. While in this work we have considered the tissue as a linear and isotropic material, real matrices such as the ones used in experiments, present a non-linear behavior. To model this type of materials, new constitutive relations could be used to describe their elasticity. Also, in this model, when we calculate the displacement field, we do so under the assumption that the material is homogeneous. Using a perturbative-iterative approach, it is possible to calculate higher order terms in the approximation, which would take into account the inhomogeneity of the tissue [113, 114]. While in this work we have considered that tip cells exert the same traction force independently of ECM stiffness, it has been reported that cells exert stronger forces on stiff ECMs than on softer substrates [115]. Simulating sprouting angiogenesis in three dimensions, as presented in this work, requires a substantial ammount of computational effort, and as such more efficient algorithms could be used to solve the model equations. Furthermore, the parallelization of the software used to solve these equations would decrease simulation time but would require the use of large computing clusters, coupled with intensive testing and debugging of the software.

Bibliography

[1] Sunita Patel-Hett and Patricia A D'Amore. "Signal transduction in vasculogenesis and developmental angiogenesis". In: *The International journal of developmental biology* 55 (2011), p. 353.

[2] Domenico Ribatti et al. "Postnatal vasculogenesis". In: *Mechanisms of development* 100.2 (2001), pp. 157–163.

[3] Emmanuel Nwadozi and Tara L Haas. "Emerging Roles of Pericytes in Coordinating Skeletal Muscle Functions: Implications and Therapeutic Potential". In: *Current Tissue Microenvironment Reports* 2 (2021), pp. 29–39.

[4] Judah Folkman. "Tumor angiogenesis: therapeutic implications". In: *New england journal of medicine* 285.21 (1971), pp. 1182–1186.

[5] Michael J Murray and Bruce A Lessey. "Embryo implantation and tumor metastasis: common pathways of invasion and angiogenesis". In: *Seminars in reproductive endocrinology*. Vol. 17. 03. Copyright© 1999 by Thieme Medical Publishers, Inc. 1999, pp. 275–290.

[6] Marcia G Tonnesen, Xiaodong Feng, and Richard AF Clark. "Angiogenesis in wound healing". In: *Journal of investigative dermatology symposium proceedings*. Vol. 5. 1. Elsevier. 2000, pp. 40–46.

[7] Austin P Veith et al. "Therapeutic strategies for enhancing angiogenesis in wound healing". In: *Advanced drug delivery reviews* 146 (2019), pp. 97–125.

[8] Hamish M Fraser and Stephen F Lunn. "Angiogenesis and its control in the female reproductive system". In: *British medical bulletin* 56.3 (2000), pp. 787–797.

[9] Uzoagu A Okonkwo and Luisa A DiPietro. "Diabetes and wound angiogenesis". In: *International journal of molecular sciences* 18.7 (2017), p. 1419.

[10] Tânia B Cruz et al. "Mice with type 2 diabetes present significant alterations in their tissue biomechanical properties and histological features". In: *Biomedicines* 10.1 (2022), p. 57.

[11] Bruce R Zetter. "Angiogenesis and tumor metastasis". In: *Annual review of medicine* 49.1 (1998), pp. 407–424.

[12] Monica S Chung and Sang Jun Han. "Endometriosis-associated angiogenesis and anti-angiogenic therapy for endometriosis". In: *Frontiers in Global Women's Health* 3 (2022).

[13] Rohit Khurana et al. "Role of angiogenesis in cardiovascular disease: a critical appraisal". In: *Circulation* 112.12 (2005), pp. 1813–1824.

[14] Judah Folkman et al. “Isolation of a tumor factor responsible for angiogenesis”. In: *The Journal of experimental medicine* 133.2 (1971), p. 275.

[15] Donald R Senger et al. “Tumor cells secrete a vascular permeability factor that promotes accumulation of ascites fluid”. In: *Science* 219.4587 (1983), pp. 983–985.

[16] Napoleone Ferrara and William J Henzel. “Pituitary follicular cells secrete a novel heparin-binding growth factor specific for vascular endothelial cells”. In: *Biochemical and biophysical research communications* 161.2 (1989), pp. 851–858.

[17] Agata N Rumianek and David R Greaves. “How have leukocyte in vitro chemotaxis assays shaped our ideas about macrophage migration?” In: *Biology* 9.12 (2020), p. 439.

[18] Paul T Elkington, Justin A Green, and Jon S Friedland. “Analysis of matrix metalloproteinase secretion by macrophages”. In: *Macrophages and Dendritic Cells: Methods and Protocols* (2009), pp. 253–265.

[19] Stefano J Mandriota et al. “Vascular endothelial growth factor-C-mediated lymphangiogenesis promotes tumour metastasis”. In: *The EMBO journal* 20.4 (2001), pp. 672–682.

[20] Steven A Stacker and Marc G Achen. “Emerging roles for VEGF-D in human disease”. In: *Biomolecules* 8.1 (2018), p. 1.

[21] Pipsa Saharinen et al. “Lymphatic vasculature: development, molecular regulation and role in tumor metastasis and inflammation”. In: *Trends in immunology* 25.7 (2004), pp. 387–395.

[22] DA Cheresh and DG Stupack. “Regulation of angiogenesis: apoptotic cues from the ECM”. In: *Oncogene* 27.48 (2008), pp. 6285–6298.

[23] Changcun Fang et al. “An important role of matrix metalloproteinase-8 in angiogenesis in vitro and in vivo”. In: *Cardiovascular research* 99.1 (2013), pp. 146–155.

[24] Xian Wu Cheng et al. “Mechanisms underlying the impairment of ischemia-induced neovascularization in matrix metalloproteinase 2–deficient mice”. In: *Circulation research* 100.6 (2007), pp. 904–913.

[25] Eve Gazave et al. “Origin and evolution of the Notch signalling pathway: an overview from eukaryotic genomes”. In: *BMC evolutionary biology* 9.1 (2009), pp. 1–27.

[26] Ilse Geudens and Holger Gerhardt. “Coordinating cell behaviour during blood vessel formation”. In: *Development* 138.21 (2011), pp. 4569–4583.

[27] Frederik De Smet et al. “Mechanisms of vessel branching: filopodia on endothelial tip cells lead the way”. In: *Arteriosclerosis, thrombosis, and vascular biology* 29.5 (2009), pp. 639–649.

[28] Katie Bentley, Holger Gerhardt, and Paul A Bates. “Agent-based simulation of notch-mediated tip cell selection in angiogenic sprout initialisation”. In: *Journal of theoretical biology* 250.1 (2008), pp. 25–36.

[29] Rui DM Travasso et al. “Tumor angiogenesis and vascular patterning: a mathematical model”. In: *PloS one* 6.5 (2011), e19989.

[30] Maurício Moreira-Soares et al. "Angiogenic Factors produced by Hypoxic Cells are a leading driver of Anastomoses in Sprouting Angiogenesis–a computational study". In: *Scientific reports* 8.1 (2018), pp. 1–12.

[31] I. Newton. *Philosophiae naturalis principia mathematica*. W. Dawson, 1687.

[32] Peter Carmeliet et al. "Targeted deficiency or cytosolic truncation of the VE-cadherin gene in mice impairs VEGF-mediated endothelial survival and angiogenesis". In: *Cell* 98.2 (1999), pp. 147–157.

[33] Cynthia A Reinhart-King, Micah Dembo, and Daniel A Hammer. "The dynamics and mechanics of endothelial cell spreading". In: *Biophysical journal* 89.1 (2005), pp. 676–689.

[34] Joseph P Califano and Cynthia A Reinhart-King. "The effects of substrate elasticity on endothelial cell network formation and traction force generation". In: *Engineering in Medicine and Biology Society, 2009. EMBC 2009. Annual International Conference of the IEEE*. IEEE. 2009, pp. 3343–3345.

[35] Roland Moll, Markus Divo, and Lutz Langbein. "The human keratins: biology and pathology". In: *Histochemistry and cell biology* 129 (2008), pp. 705–733.

[36] Pavel Strnad et al. "Unique amino acid signatures that are evolutionarily conserved distinguish simple-type, epidermal and hair keratins". In: *Journal of Cell Science* 124.24 (2011), pp. 4221–4232.

[37] DM Toivola et al. "Intermediate filaments take the heat as stress proteins". In: *Trends in cell biology* 20.2 (2010), pp. 79–91.

[38] Reinhard Windoffer et al. "Cytoskeleton in motion: the dynamics of keratin intermediate filaments in epithelia". In: *Journal of Cell Biology* 194.5 (2011), pp. 669–678.

[39] Nam-On Ku and M Bishr Omary. "Keratins turn over by ubiquitination in a phosphorylation-modulated fashion". In: *The Journal of cell biology* 149.3 (2000), pp. 547–552.

[40] Mayumi Komine. "Regulation of expression of keratins and their pathogenic roles in keratinopathies". In: *Keratin*. IntechOpen, 2018.

[41] Gunduz Caginalp. "An analysis of a phase field model of a free boundary". In: *Archive for Rational Mechanics and Analysis* 92.3 (1986), pp. 205–245.

[42] Seshadev Sahoo and Kevin Chou. "Review on phase-field modeling of microstructure evolutions: application to electron beam additive manufacturing". In: *International Manufacturing Science and Engineering Conference*. Vol. 45813. American Society of Mechanical Engineers. 2014, V002T02A020.

[43] Samuel M Allen and John W Cahn. "A microscopic theory for antiphase boundary motion and its application to antiphase domain coarsening". In: *Acta Metallurgica* 27.6 (1979), pp. 1085–1095.

[44] John W Cahn and John E Hilliard. "Free energy of a nonuniform system. I. Interfacial free energy". In: *The Journal of chemical physics* 28.2 (1958), pp. 258–267.

[45] Marcos Gouveia et al. “Keratin Dynamics and Spatial Distribution in Wild-Type and K14 R125P Mutant Cells—A Computational Model”. In: *International journal of molecular sciences* 21.7 (2020), p. 2596.

[46] Lena Ramms et al. “Keratins as the main component for the mechanical integrity of keratinocytes”. In: *Proceedings of the National Academy of Sciences* 110.46 (2013), pp. 18513–18518.

[47] Kristin Seltmann et al. “Keratins significantly contribute to cell stiffness and impact invasive behavior”. In: *Proceedings of the National Academy of Sciences* 110.46 (2013), pp. 18507–18512.

[48] Francois Bordeleau et al. “Keratin contribution to cellular mechanical stress response at focal adhesions as assayed by laser tweezers”. In: *Biochemistry and cell biology* 86.4 (2008), pp. 352–359.

[49] Ming Guo et al. “The role of vimentin intermediate filaments in cortical and cytoplasmic mechanics”. In: *Biophysical journal* 105.7 (2013), pp. 1562–1568.

[50] Daniel A Fletcher and R Dyche Mullins. “Cell mechanics and the cytoskeleton”. In: *Nature* 463.7280 (2010), pp. 485–492.

[51] Guillaume Salbreux, Guillaume Charras, and Ewa Paluch. “Actin cortex mechanics and cellular morphogenesis”. In: *Trends in cell biology* 22.10 (2012), pp. 536–545.

[52] Florian Huber et al. “Cytoskeletal crosstalk: when three different personalities team up”. In: *Current opinion in cell biology* 32 (2015), pp. 39–47.

[53] Kevin Wilhelmsen, Sandy HM Litjens, and Arnoud Sonnenberg. “Multiple functions of the integrin $\alpha 6\beta 4$ in epidermal homeostasis and tumorigenesis”. In: *Molecular and cellular biology* 26.8 (2006), pp. 2877–2886.

[54] Špela Zemljič Jokhadar and Jure Derganc. “Structural rearrangements in CHO cells after disruption of individual cytoskeletal elements and plasma membrane”. In: *Cell Biochemistry and Biophysics* 71 (2015), pp. 1605–1613.

[55] Seyun Kim, Pauline Wong, and Pierre A Coulombe. “A keratin cytoskeletal protein regulates protein synthesis and epithelial cell growth”. In: *Nature* 441.7091 (2006), pp. 362–365.

[56] Hunain Alam et al. “Novel function of keratins 5 and 14 in proliferation and differentiation of stratified epithelial cells”. In: *Molecular biology of the cell* 22.21 (2011), pp. 4068–4078.

[57] Sonja M Wojcik, Donnie S Bundman, and Dennis R Roop. “Delayed wound healing in keratin 6a knockout mice”. In: *Molecular and cellular biology* 20.14 (2000), pp. 5248–5255.

[58] Stacy Mazzalupo et al. “Role for keratins 6 and 17 during wound closure in embryonic mouse skin”. In: *Developmental dynamics: an official publication of the American Association of Anatomists* 226.2 (2003), pp. 356–365.

[59] Cristina Velez-delValle et al. “Epithelial cell migration requires the interaction between the vimentin and keratin intermediate filaments”. In: *Scientific reports* 6.1 (2016), p. 24389.

[60] Sungjun Yoon and Rudolf E Leube. "Keratin intermediate filaments: intermediaries of epithelial cell migration". In: *Essays in biochemistry* 63.5 (2019), pp. 521–533.

[61] Fei-Chi Yang, Yuchen Zhang, and Maikel C Rheinstädter. "The structure of people's hair". In: *PeerJ* 2 (2014), e619.

[62] Takashi Kitahara and Hideoki Ogawa. "The extraction and characterization of human nail keratin". In: *Journal of dermatological science* 2.6 (1991), pp. 402–406.

[63] Chang-Hun Lee et al. "Structural basis for heteromeric assembly and perinuclear organization of keratin filaments". In: *Nature structural & molecular biology* 19.7 (2012), pp. 707–715.

[64] David AD Parry et al. "Towards a molecular description of intermediate filament structure and assembly". In: *Experimental cell research* 313.10 (2007), pp. 2204–2216.

[65] Harald Herrmann and Ueli Aebi. "Intermediate filaments: structure and assembly". In: *Cold Spring Harbor Perspectives in Biology* 8.11 (2016), a018242.

[66] Harald Herrmann et al. "Characterization of early assembly intermediates of recombinant human keratins". In: *Journal of structural biology* 137.1-2 (2002), pp. 82–96.

[67] Jean Christopher Chamcheu et al. "Keratin gene mutations in disorders of human skin and its appendages". In: *Archives of biochemistry and biophysics* 508.2 (2011), pp. 123–137.

[68] Mirjana Liovic et al. "A novel keratin 5 mutation (K5V186L) in a family with EBS-K: a conservative substitution can lead to development of different disease phenotypes". In: *Journal of investigative dermatology* 116.6 (2001), pp. 964–969.

[69] Pouria Khani et al. "Keratins and epidermolysis bullosa simplex". In: *Journal of cellular physiology* 234.1 (2019), pp. 289–297.

[70] Mariella D'Alessandro et al. "Keratin mutations of epidermolysis bullosa simplex alter the kinetics of stress response to osmotic shock". In: *Journal of Cell Science* 115.22 (2002), pp. 4341–4351.

[71] SM Morley et al. "Generation and characterization of epidermolysis bullosa simplex cell lines: scratch assays show faster migration with disruptive keratin mutations". In: *British Journal of Dermatology* 149.1 (2003), pp. 46–58.

[72] Mirjana Liovic et al. "Observation of keratin particles showing fast bidirectional movement colocalized with microtubules". In: *Journal of cell science* 116.8 (2003), pp. 1417–1427.

[73] Mirjana Liovic et al. "Dual-specificity phosphatases in the hypo-osmotic stress response of keratin-defective epithelial cell lines". In: *Experimental cell research* 314.10 (2008), pp. 2066–2075.

[74] Mirjana Liovic et al. "Severe keratin 5 and 14 mutations induce down-regulation of junction proteins in keratinocytes". In: *Experimental cell research* 315.17 (2009), pp. 2995–3003.

[75] Tina Zupancic et al. “Intestinal cell barrier function in vitro is severely compromised by keratin 8 and 18 mutations identified in patients with inflammatory bowel disease”. In: *PLoS One* 9.6 (2014), e99398.

[76] Nicola Susann Werner et al. “Epidermolysis bullosa simplex-type mutations alter the dynamics of the keratin cytoskeleton and reveal a contribution of actin to the transport of keratin subunits”. In: *Molecular biology of the cell* 15.3 (2004), pp. 990–1002.

[77] Marcin Moch et al. “Measuring the regulation of keratin filament network dynamics”. In: *Proceedings of the National Academy of Sciences* 110.26 (2013), pp. 10664–10669.

[78] Reinhard Windoffer et al. “Focal adhesions are hotspots for keratin filament precursor formation”. In: *The Journal of cell biology* 173.3 (2006), pp. 341–348.

[79] Veena Prahlad et al. “Rapid movements of vimentin on microtubule tracks: kinesin-dependent assembly of intermediate filament networks”. In: *The Journal of cell biology* 143.1 (1998), pp. 159–170.

[80] Amelie Robert et al. “Kinesin-dependent transport of keratin filaments: a unified mechanism for intermediate filament transport”. In: *The FASEB Journal* 33.1 (2019), p. 388.

[81] M Bishr Omary, Pierre A Coulombe, and WH Irwin McLean. “Intermediate filament proteins and their associated diseases”. In: *New England Journal of Medicine* 351.20 (2004), pp. 2087–2100.

[82] Ildiko Szeverenyi et al. “The Human Intermediate Filament Database: comprehensive information on a gene family involved in many human diseases”. In: *Human mutation* 29.3 (2008), pp. 351–360.

[83] Rebecca L Haines and E Birgitte Lane. “Keratins and disease at a glance”. In: *Journal of cell science* 125.17 (2012), pp. 3923–3928.

[84] Norbert Mucke et al. “Assembly kinetics of vimentin tetramers to unit-length filaments: a stopped-flow study”. In: *Biophysical journal* 114.10 (2018), pp. 2408–2418.

[85] Stéphanie Portet et al. “Keratin dynamics: modeling the interplay between turnover and transport”. In: *PloS one* 10.3 (2015), e0121090.

[86] Anne Kolsch et al. “The keratin-filament cycle of assembly and disassembly”. In: *Journal of cell science* 123.13 (2010), pp. 2266–2272.

[87] Stéphanie Portet et al. “Organization of the cytokeratin network in an epithelial cell”. In: *Journal of theoretical biology* 223.3 (2003), pp. 313–333.

[88] Stéphanie Portet et al. “Intermediate filament networks: in vitro and in vivo assembly models”. In: *Comptes Rendus Biologies* 327.11 (2004), pp. 970–976.

[89] Chengjun Sun et al. “A mathematical model for the keratin cycle of assembly and disassembly”. In: *The IMA Journal of Applied Mathematics* 80.1 (2015), pp. 100–114.

[90] Michael Beil et al. “Simulating the formation of keratin filament networks by a piecewise-deterministic Markov process”. In: *Journal of theoretical biology* 256.4 (2009), pp. 518–532.

[91] Ryan P Hobbs, Justin T Jacob, and Pierre A Coulombe. "Keratins are going nuclear". In: *Developmental cell* 38.3 (2016), pp. 227–233.

[92] Špela Zemljič Jokhadar et al. "Cortical stiffness of keratinocytes measured by lateral indentation with optical tweezers". In: *Plos one* 15.12 (2020), e0231606.

[93] Marcos Gouveia et al. "A mathematical model for the dependence of keratin aggregate formation on the quantity of mutant keratin expressed in EGFP-K14 R125P keratinocytes". In: *Plos one* 16.12 (2021), e0261227.

[94] David Garfinkel, Carl B Marbach, and Norman Z Shapiro. "Stiff differential equations". In: *Annual review of biophysics and bioengineering* 6.1 (1977), pp. 525–542.

[95] Lawrence F Shampine and Skip Thompson. "Stiff systems". In: *Scholarpedia* 2.3 (2007), p. 2855.

[96] George D Byrne and Alan C Hindmarsh. "Stiff ODE solvers: A review of current and coming attractions". In: *Journal of Computational physics* 70.1 (1987), pp. 1–62.

[97] Ivan B Lobov et al. "WNT7b mediates macrophage-induced programmed cell death in patterning of the vasculature". In: *Nature* 437.7057 (2005), pp. 417–421.

[98] Annette P Meeson et al. "VEGF deprivation-induced apoptosis is a component of programmed capillary regression". In: *Development* 126.7 (1999), pp. 1407–1415.

[99] Suzanne Hughes and TAILOI CHAN-LING. "Roles of endothelial cell migration and apoptosis in vascular remodeling during development of the central nervous system". In: *Microcirculation* 7.5 (2000), pp. 317–333.

[100] Eva Kochhan et al. "Blood flow changes coincide with cellular rearrangements during blood vessel pruning in zebrafish embryos". In: *PloS one* 8.10 (2013), e75060.

[101] Claudio A Franco et al. "Dynamic endothelial cell rearrangements drive developmental vessel regression". In: *PLoS biology* 13.4 (2015), e1002125.

[102] Makiko Nonomura. "Study on multicellular systems using a phase field model". In: *PloS one* 7.4 (2012), e33501.

[103] M Akiyama et al. "Numerical study on spindle positioning using phase field method". In: *Physical biology* 16.1 (2018), p. 016005.

[104] Heloísa Gerardo et al. "Soft culture substrates favor stem-like cellular phenotype and facilitate reprogramming of human mesenchymal stem/stromal cells (hMSCs) through mechanotransduction". In: *Scientific reports* 9.1 (2019), pp. 1–18.

[105] Florian Milde, Michael Bergdorf, and Petros Koumoutsakos. "A hybrid model for three-dimensional simulations of sprouting angiogenesis". In: *Biophysical journal* 95.7 (2008), pp. 3146–3160.

[106] Flávia Sousa et al. "Intratumoral VEGF nanotrapper reduces gliobastoma vascularization and tumor cell mass". In: *Journal of Controlled Release* 339 (2021), pp. 381–390.

[107] Maria Margarida Dias Soares Quinas Guerra and Rui DM Travasso. "Novel approach to vascular network modeling in 3D". In: *2012 IEEE 2nd Portuguese meeting in bioengineering (ENBENG)*. IEEE. 2012, pp. 1–6.

[108] Patrícia Santos-Oliveira et al. “The force at the tip-modelling tension and proliferation in sprouting angiogenesis”. In: *PLoS computational biology* 11.8 (2015), e1004436.

[109] Marcos João do Carmo Gouveia. “Simulating Vessel Growth with Extracellular Matrix Remodelling”. Universidade de Coimbra, 2017.

[110] Christopher A Lemmon and Lewis H Romer. “A predictive model of cell traction forces based on cell geometry”. In: *Biophysical journal* 99.9 (2010), pp. L78–L80.

[111] João RD Ramos, Rui Travasso, and João Carvalho. “Capillary network formation from dispersed endothelial cells: Influence of cell traction, cell adhesion, and extracellular matrix rigidity”. In: *Physical Review E* 97.1 (2018), p. 012408.

[112] Elisabeth G Rens and Roeland MH Merks. “Cell shape and durotaxis explained from cell-extracellular matrix forces and focal adhesion dynamics”. In: *Iscience* 23.9 (2020), p. 101488.

[113] SY Hu and LQ Chen. “A phase-field model for evolving microstructures with strong elastic inhomogeneity”. In: *Acta materialia* 49.11 (2001), pp. 1879–1890.

[114] P Yu et al. “An iterative-perturbation scheme for treating inhomogeneous elasticity in phase-field models”. In: *Journal of Computational Physics* 208.1 (2005), pp. 34–50.

[115] Marion Ghibaudo et al. “Traction forces and rigidity sensing regulate cell functions”. In: *Soft Matter* 4.9 (2008), pp. 1836–1843.